



National Technical University of Athens  
School of Naval Architecture and Marine Engineering  
Shipbuilding Technology Laboratory

Diploma Thesis

*Structural Design of CNG Storing Composite Pressure Vessels for  
Marine Applications*

Tsonos Angelos

Thesis Supervisor: Professor N. Tsouvalis

Athens, October 2017





Εθνικό Μετσόβιο Πολυτεχνείο  
Σχολή Ναυπηγών Μηχανολόγων Μηχανικών  
Εργαστήριο Ναυπηγικής Τεχνολογίας

Διπλωματική Εργασία

*Κατασκευαστικός Σχεδιασμός Δεξαμενών CNG από Σύνθετα Υλικά για  
Ναυπηγικές Εφαρμογές*

Τσώνος Άγγελος

Επιβλέπων: Καθηγητής Ν. Τσούβαλης

Τριμελής Επιτροπή

Ν. Τσούβαλης  
Καθηγητής Ε.Μ.Π

Δ. Παντελής  
Καθηγητής Ε.Μ.Π

Μ. Σαμουηλίδης  
Καθηγητής Ε.Μ.Π

Αθήνα, Οκτώβριος 2017

.....  
**Άγγελος Ι. Τσώνος**

Διπλωματούχος Ναυπηγός Μηχανολόγος Μηχανικός Ε.Μ.Π.

Copyright © Τσώνος Άγγελος 2017

Με επιφύλαξη παντός δικαιώματος. All rights reserved

Απαγορεύεται η αντιγραφή, αποθήκευση και διανομή της παρούσας εργασίας, εξ ολοκλήρου ή τμήματος αυτής, για εμπορικό σκοπό. Επιτρέπεται η ανατύπωση, αποθήκευση και διανομή για σκοπό μη κερδοσκοπικό, εκπαιδευτικής ή ερευνητικής φύσης, υπό την προϋπόθεση να αναφέρεται η πηγή προέλευσης και να διατηρείται το παρόν μήνυμα. Ερωτήματα που αφορούν τη χρήση της εργασίας για κερδοσκοπικό σκοπό πρέπει να απευθύνονται προς τον συγγραφέα.

Οι απόψεις και τα συμπεράσματα που περιέχονται σε αυτό το έγγραφο εκφράζουν τον συγγραφέα και δεν πρέπει να ερμηνευθεί ότι αντιπροσωπεύουν τις επίσημες θέσεις του Εθνικού Μετσόβιου Πολυτεχνείου.

## **Acknowledgements**

This diploma thesis was carried out at the Shipbuilding Technology Laboratory (STL) of the School of Naval Architecture and Marine Engineering of the National Technical University of Athens, under the supervision of Professor Nicholas Tsouvalis.

First of all, I would like to express my sincere and humble appreciation to Professor Nicholas Tsouvalis for giving me the opportunity to work on this research topic. Furthermore, his technical insights, innovative ideas, and support not only made this thesis possible but also shaped my mind as an engineer.

Secondly, I would like to thank Astrinos Papadakis, PhD student at the STL, for his continuous encouragement and support throughout the conduction of this thesis. His contribution was vital for the completion of this thesis.

I would also like to express my gratitude to the permanent staff of the Shipbuilding Technology Laboratory and especially to A. Markoulis and C. Xanthis, whose help was critical for the experimental part of this work.

Last but not least, I want to thank my family and my friends for their support throughout this thesis and for giving me reasons and motivation to become a better person and scientist.



## **Abstract**

The use of the natural gas as a propulsion fuel is becoming gradually more popular in the marine industry, as it offers complete compliance with the recent emission restrictions (SO<sub>x</sub> and NO<sub>x</sub>). However, further research is needed for its onboard storage. CNG is stored in pressure vessels able to withstand operating pressures above 250bar. Although the use of composite materials for their construction offers a lightweight solution, it imposes new challenges to the structural designer. The use of simulation software packages, that utilize the Finite Element Method (FEM), is an efficient and economically feasible option to cope with the former issue. In the context of this thesis, a simulation model was developed in Abaqus software.

The development of the model demanded extensive bibliographic research concerning designing and manufacturing aspects of composite pressure vessels. The research included important for the structural behavior of the pressure vessel topics like winding trajectories and modeling of thickness build-up at the dome regions. The design parameters and the extent at which they affect the aforementioned topics were also investigated. In addition, the theoretical modeling of the thickness build-up at the dome region was verified with thickness measurements at a constructed pressure vessel.

The obtained theoretical knowledge was used in the development of the simulation model. This model was used for the conduction of a parametric study, which investigated the design parameters that affect the structural behavior of the pressure vessel and helped in the optimization of its weight. Finally, based on the conclusions of the parametric study, the structural design of a pressure vessel was made. The pressure vessel is designed to be used in marine applications.

**Keywords:** Finite Element Method (FEM), simulation, structural design, composite pressure vessel, composite material, filament winding, natural gas, CNG

## Περίληψη

Η χρήση του φυσικού αερίου ως καύσιμο πρόωσης γίνεται σταδιακά πιο διαδεδομένη στο χώρο της ναυπηγικής, αφού προσφέρει απόλυτη συμμόρφωση με τους πρόσφατους περιορισμούς ρίπων των καυσαερίων (SOx και NOx). Όμως, περισσότερη έρευνα απαιτείται για την αποθήκευση του στο πλοίο. Το CNG αποθηκεύεται σε δοχεία πίεσεως ικανά να αντέξουν πιέσεις λειτουργίας άνω των 250bar. Παρόλο που η χρήση σύνθετων υλικών για την κατασκευή τους προσφέρει χαμηλό βάρος, δημιουργεί νέες προκλήσεις για τον σχεδιαστή. Η χρήση λογισμικών προσομοίωσης, που αξιοποιούν την Μέθοδο Πεπερασμένων Στοιχείων, είναι μία αποδοτική και οικονομικά εφικτή επιλογή για να αντιμετωπιστούν οι παραπάνω προκλήσεις. Στο πλαίσιο της παρούσας διπλωματικής, αναπτύχθηκε μοντέλο προσομοίωσης στο λογισμικό Abaqus.

Η ανάπτυξη του μοντέλου απαιτήσε εκτενή βιβλιογραφική έρευνα σχετικά με σχεδιαστικά και κατασκευαστικά θέματα δοχείων πίεσης από σύνθετα υλικά. Η έρευνα περιέλαβε σημαντικά για την μηχανική απόκριση της κατασκευής θέματα, όπως οι τροχιές των ινών περιέλιξης και την μοντελοποίηση της αύξησης του πάχους του σύνθετου υλικού στην περιοχή των θόλων. Επίσης, ερευνήθηκαν οι σχεδιαστικές παράμετροι και ο βαθμός με τον οποίο αυτοί επηρεάζουν τα παραπάνω θέματα. Επιπροσθέτως, η θεωρητική μοντελοποίηση της αύξησης του πάχους στην περιοχή των θόλων επιβεβαιώθηκε με μετρήσεις σε κατασκευασμένο δοχείο πίεσης.

Η αποκτηθείσα θεωρητική γνώση χρησιμοποιήθηκε στην ανάπτυξη του μοντέλου προσομοίωσης. Το συγκεκριμένο μοντέλο χρησιμοποιήθηκε για την διενέργεια παραμετρικής μελέτης, που εξέτασε τις σχεδιαστικές παραμέτρους που επηρεάζουν την απόκριση του δοχείου και βοήθησε στην βελτιστοποίηση του βάρους του. Τέλος, με βάση τα συμπεράσματα που εξήχθησαν από την παραμετρική μελέτη, έγινε η σχεδιαστική μελέτη ενός δοχείου πίεσης. Το συγκεκριμένο δοχείο πίεσης είναι σχεδιασμένο για να χρησιμοποιηθεί σε ναυπηγικές εφαρμογές.

**Λέξεις κλειδιά:** Μέθοδος Πεπερασμένων Στοιχείων, προσομοίωση, κατασκευαστικός σχεδιασμός, δοχείο πίεσης από σύνθετα υλικά, σύνθετα υλικά, μέθοδος περιέλιξης ινών, φυσικό αέριο, CNG



# Contents

Chapter 1	Introduction.....	11
1.1	Environmental issues and restrictions .....	11
1.2	Proposed alternatives .....	12
1.3	Natural Gas as an alternative fuel.....	13
1.4	CNG in shipping industry.....	15
1.4.1	CNG and LNG.....	15
1.4.2	CNG fuelled ships .....	15
1.4.3	Rules and Standards for tank location and arrangement on ship.....	18
1.5	Scope of the thesis .....	21
Chapter 2	CNG Pressure Vessels .....	24
2.1	General.....	24
2.2	Manufacturing of pressure vessels with the filament winding method .....	25
2.3	Rules and Standards for Designing, Manufacturing and Testing.....	27
2.3.1	The ASME Boiler and Pressure Vessel Code .....	27
2.3.2	Rules and Regulations of Classification Societies .....	28
2.4	Literature Review .....	32
Chapter 3	Theory of Filament Winding .....	36
3.1	Winding Trajectory.....	36
3.1.1	Geodesic and non-geodesic trajectories .....	36
3.1.2	Maximum static friction coefficient .....	39
3.1.3	The winding equation used in Wound Composite Modeller of Abaqus ..	42
3.1.4	Winding angle diagrams .....	43
3.2	Thickness variation along the dome .....	48
3.2.1	Theoretical equations and comparison .....	48
3.2.2	Experimental results .....	51
Chapter 4	Numerical Simulation .....	60
4.1	Description of the reference model .....	60
4.1.1	Mesh Convergence Analysis .....	63
4.2	Description of the new model created in Abaqus.....	65
4.2.1	Mesh convergence analysis .....	67
4.3	Comparison of ANSYS and Abaqus models.....	68
4.3.1	Comparison based on stiffness .....	69
4.3.2	Comparison based on the developed stresses .....	70
4.4	Evaluation of the impact of the increasing thickness at domes.....	72
Chapter 5	Case Study .....	79

5.1	General description of the initial design of the case study .....	79
5.1.1	Mesh convergence analysis .....	81
5.1.2	Results of the initial design .....	82
5.2	Parametric Study.....	87
5.2.1	The impact of the helical/hoop layer thickness ratio on the strength of the pressure vessel .....	87
5.2.2	The impact of the liner thickness on the strength of the pressure vessel..	89
5.2.3	The impact of the dome shape on the strength and stiffness of the pressure vessel .....	92
5.3	Definition of the total thickness of the composite reinforcement .....	95
5.4	The final design .....	97
5.4.1	Description of the final design.....	97
5.4.2	Results of the analysis at failure load .....	98
5.4.3	Results of the analysis at the operating load (25 MPa) .....	101
Chapter 6	Conclusions and Recommended Future Work .....	105
6.1	Conclusions .....	105
6.2	Recommended future work .....	106
References	.....	108
Appendix A	.....	112

## Chapter 1 Introduction

### 1.1 Environmental issues and restrictions

The revised Annex VI of International Convention for the Prevention of Pollution from Ships (MARPOL) created new challenges for the shipping industry. The amendment limits sulphur content in fuel to 0.1% in Emission Control Areas (ECAs) since 1 January 2015 and to 3.5% for the rest of the world since 1 January 2012. The cap will be further decreased to 0.5% globally in 2020. The effective date depends on the conclusions of a study on availability of low sulphur fuel that will be completed in 2018 by International Marine Organization (IMO). According to Adamchak and Adede (2013), if IMO decides that the low sulphur fuel is insufficient, the date of implementation can be delayed until 2025.

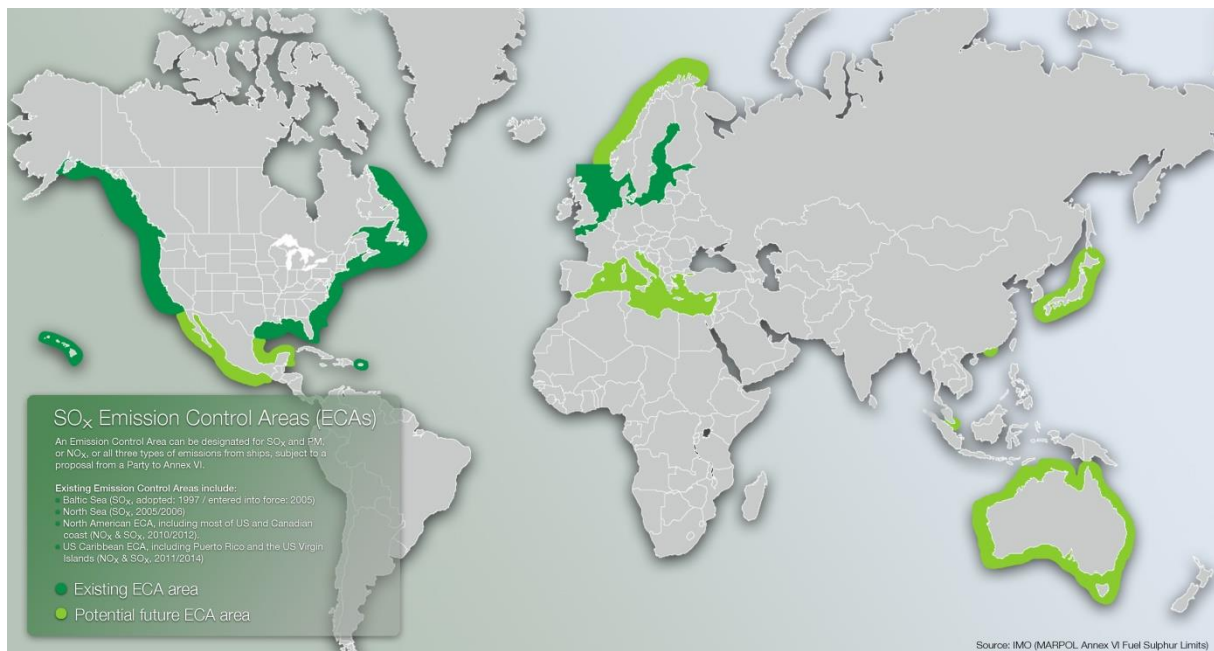


**Figure 1-1 Existing and potential future Emission Control Areas (Pospiech, 2014)**

Annex VI limits also NO<sub>x</sub> emissions of installed marine engines of over 130kW output. The limits are divided in two levels (Tiers) based on the area of operation and construction date. The Tier III controls affect ships operating in ECAs, which are constructed on or after 1 January 2016. The Tier II controls apply globally to ships constructed on or after 1 January 2011. There are currently established four ECAs, Baltic Sea area (SO<sub>x</sub> only), North Sea area (SO<sub>x</sub> only), North American area (SO<sub>x</sub>, NO<sub>x</sub> and PM) and United States Caribbean Sea area (SO<sub>x</sub>, NO<sub>x</sub> and PM) (I.M.O., 1973). Therefore, the Tier III controls apply only to North American and United States Caribbean Sea areas. However, as the Figure 1-1 shows, new ECAs may be implemented by IMO in the forthcoming years. The actual limits of NO<sub>x</sub> emissions are determined from the engine's rated speed, as shown in Figure 1-2.

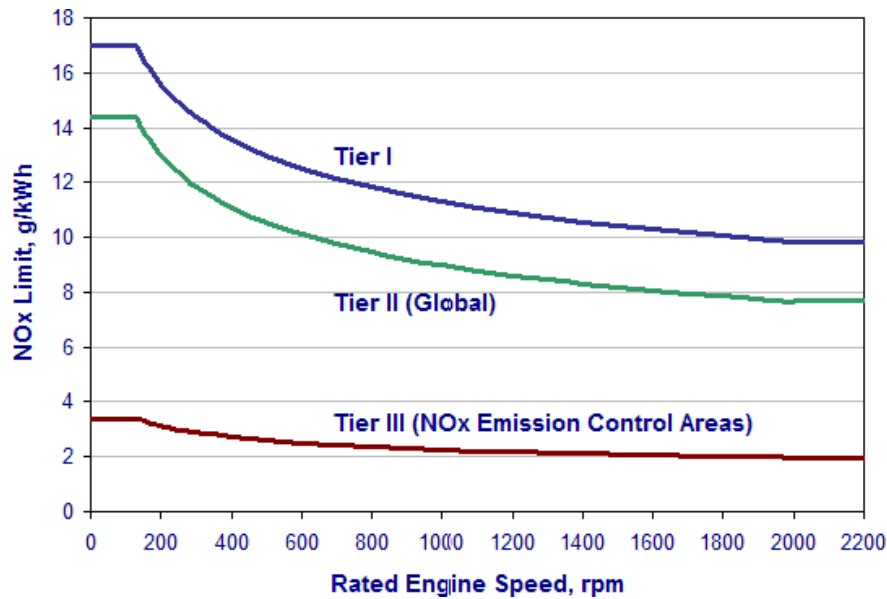


Figure 1-2 NOx emission limits (dieselnet.com)

## 1.2 Proposed alternatives

The maritime industry has to adapt in order to comply with IMO restrictions. There are different solutions proposed. According to Semolinos et al. (2013), only three of the solutions are realistic; use MDO as main engine fuel, install scrubbers on board the ships or convert to natural gas fuelled propulsion.

MDO can be used on existing machineries with no alterations needed and only ships constructed on or after 2016 need to have a selective catalytic reduction (SCR) system installed to limit NOx emissions. This fuel is already used for secondary engines of ships, so it is widely available in ports. In addition, ship-owners are familiar with its use and market characteristics. However, the increase of MDO consumption will require further investments to be made in current infrastructure's capacities to accommodate demand. A similar alternative could be the use of low sulphur HFO, but as reported by Semolinos et al. (2013), this option seems unlikely to materialize due to high cost.

An alternate solution is the use of exhaust-gas scrubbers, which use seawater to wash SOx out of the exhaust gases. This technology allows ship-owners to continue using HFO as propulsion fuel. Nevertheless, the scrubbers have to be installed on top of the exhaust gas stack, as a result may cause stability problems for some ships. For this reason, ferries appear to be poor candidates for this solution (Semolinos et al., 2013). Additionally, scrubbers increase fuel consumption by 1% to 3% and maintenance cost and OPEX are also higher (Semolinos et al., 2013).

Another option proposed is using natural gas to fuel the propulsion system. Natural gas allows ships to achieve compliance with IMO restrictions for SOx, NOx and PM emissions. As a bonus, Semolinos et al. (2013) state that the combustion of natural gas is cleaner, therefore engines need less maintenance. On the other hand, due to low energy density of gas, the storage equipment requires much more space than the counterpart does for MDO or HFO. An added drawback in choosing this solution is the unavailability of bunkering facilities in ports.

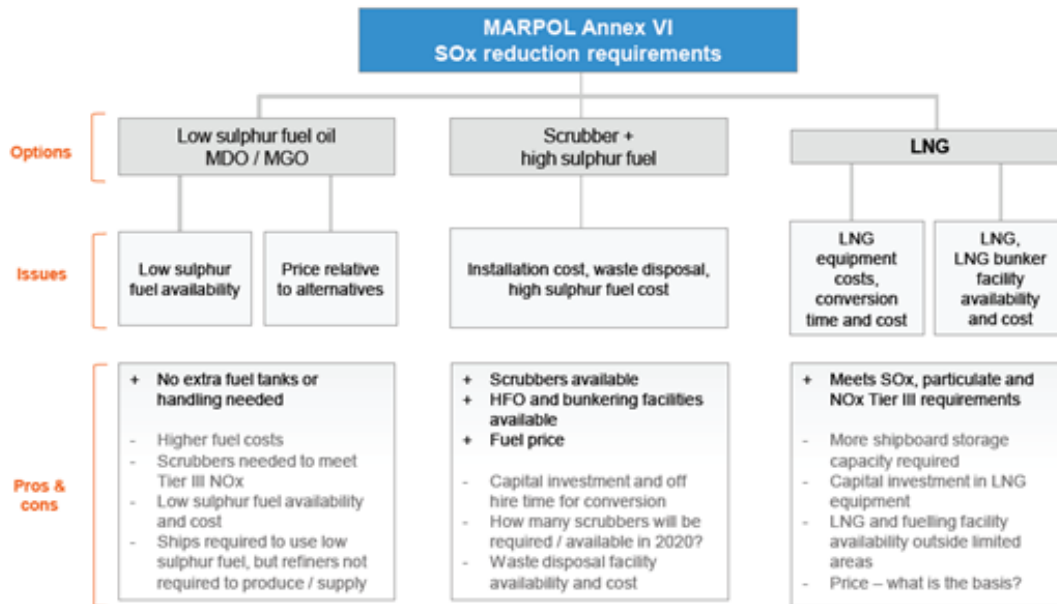


Figure 1-3 Pros & Cons of the three alternatives (Adamchak and Adede, 2013)

### 1.3 Natural Gas as an alternative fuel

Natural Gas (NG) is a gas mixture of light hydrocarbons consisting primarily of Methane (CH<sub>4</sub>). It is a colourless and odourless fossil fuel. It also contains amounts of other light hydrocarbons (like ethane, propane and butane), and a small percentage of higher alkanes and other gases such as carbon dioxide, oxygen and nitrogen (Wikipedia, 2006). However, its composition and chemical characteristics depend on the source and the production process. A typical composition is shown in Table 1-1. It is lighter than air, non-toxic and cannot contaminate water. In addition, it is safe against explosion because its flammability range is narrow (4.3% to 15.2% by volume in air (Khan et al., 2015)).

Table 1-1 Typical component and content of natural gas (Wei and Geng, 2016)

Component	Typical analysis (vol. %)	Range (vol. %)
Methane	94.9	87.0–96.0
Ethane	2.5	1.8–5.1
Propane	0.2	0.1–1.5
Isobutane	0.03	0.01–0.3
n-Butane	0.03	0.01–0.3
Isopentane	0.01	Trace to 0.14
n-Pentane	0.01	Trace to 0.14
Hexane	0.01	Trace to 0.06
Nitrogen	1.6	1.3–5.6
Carbon dioxide	0.7	0.1–1.0
Oxygen	0.02	0.01–0.1
Hydrogen	Trace	Trace to 0.02

Its clean combustion makes it an environmentally friendly fuel, suitable for transportation use. It has been used as an automotive fuel since 1930s. Nevertheless, natural gas vehicles (NGVs) became attractive in 1970s when the oil prices rose due to oil crisis (Khan et al., 2015). According to Khan et al. (2015), there are over 18 million NGVs globally, mainly on non-OECD countries, with the majority of them (93%) being light duty cars and commercial vehicles. Lately, because of the MARPOL Annex VI regulation more and more ship-owners consider natural gas as an alternative fuel. Adamchak and Adede (2013) declare that in 2013, 78 LNG fuelled ship were existing and another 115 were in order.

Although natural gas has a similar low heating value to diesel (the exact value depends on the source of gas), its low energy density is a significant drawback. Natural gas has to be liquefied (LNG) by cooling it to approximately  $-162^{\circ}\text{C}$ , or compressed (CNG) by compressing it at a pressure of 200-250 bar (3000-3600 psi), in order to be stored on vehicle, but even in those forms its density is approximately 2 times for LNG and 5 times for CNG lower than diesel's. As a result, the space needed to store natural gas on board is a lot bigger than for diesel. Besides, both forms demand specially designed cylindrical or spherical storage tanks and additional equipment to maintain desired pressure and temperature. The above suggest that retrofitting is not feasible for all existing ships due to insufficient space.

**Table 1-2 Physicochemical properties of natural gas and diesel (Wei and Geng, 2016)**

Fuel properties	Natural gas	Diesel
Low heating value (MJ/kg)	48.6	42.5
Heating value of stoichiometric mixture (MJ/kg)	2.67	2.79
Cetane number	-	52.1
Auto-ignition temperature ( $^{\circ}\text{C}$ )	650	180–220
Stoichiometric air–fuel ratio (kg/kg)	17.2	14.3
Carbon content (%)	75	87

An advantage of natural gas is that it can be burned in a conventional diesel engine. Even though, natural gas has a very high octane number (130) making it suitable for spark-ignited engines, marine diesel engines can burn it in a dual fuel mode with only slight modifications in their structures. A modified dual fuel diesel engine use natural gas as main fuel and a small amount of diesel as pilot fuel, usually in a ratio of approximately 97%-3% (MAN, 2014). The auto-ignition temperature of natural gas is very high corresponding to diesel and its cetane number very low (see Table 1-2), so an ignition source is needed to ignite the natural gas in the cylinder (Wei and Geng, 2016). As stated by Papagiannakis and Hountalas (2004), the primary fuel (natural gas) is mixed with air outside the chamber and then the mixture is inducted in the cylinder and then is compressed like in a conventional diesel engine. The pilot fuel (diesel) is injected in the chamber near the end of the compression stroke, it autoignites and becomes the ignition source for the surrounding gaseous mixture. According to Wei and Geng (2016), the engine power decreases when operates in dual fuel mode, the maximum decline found to be 2.1%. However, the dual fuel

mode decreases significantly NO<sub>x</sub>, CO<sub>2</sub>, and PM emissions, which are limited by MARPOL Annex VI restrictions.

From an economic point of view, natural gas is considered an affordable source of energy and as a result it has been used for domestic and transportation use for years. Khan et al. (2015) state that the cost of CNG, which is used for land transportation, is 0.56\$ per litter diesel equivalent on average (globally), whereas diesel costs 0.93\$ per litter on average. Even though the cost advantage of CNG over diesel for land transportation is significant, the price, that gas will be traded at bunkering stations when the global demand grows, remains uncertain. It is expected to cost less than MDO and to be comparable with HFO (sgmf, 2014, Adamchak and Adede, 2013).

## **1.4 CNG in shipping industry**

### **1.4.1 CNG and LNG**

CNG is natural gas pressurized at 200-250bar for ease of storage and transport. It occupies less than 1 per cent of the volume that natural gas occupies at standard atmospheric pressure. It is stored in cylindrical vessels made of steel, aluminium, or composite materials. It is widely used for land transportation, primarily in public transportation vehicles, like city busses, because it is a low-cost and environmentally friendly fuel. The international number of CNG fuelled vehicles has grown rapidly (average annual growth rate 24%) over the past years. As reported by Khan et al. (2015), there are over 18 million vehicles operating with CNG globally, with the world leader being Iran with approximately 4.1 million NGVs and following closely behind Iran is China with 4 million NGVs.

LNG is natural gas that has been converted to liquid form. It is made by cooling natural gas to -162 °C. It is stored in cylindrical or spherical shaped cryogenic tanks. The energy density of LNG is 2.4 times greater than CNG, thus it is more cost efficient to transport natural gas over long distances as LNG (Wikipedia, 2005b, Kumar et al., 2011). LNG carriers have been using boil off gas to fuel their propulsion system since the first ship put on operation in 1964 (Einang and Haavik, 2000) and it has been used on ferries in Norway (Mosaad, 2013). Nowadays, ship-owners consider converting their ships to operate with LNG in order to achieve compliance with IMO emission restrictions.

CNG and LNG are both proven technologies and can be used in shipping industry. As mentioned above, LNG has 2.4 times greater energy density than CNG, so seems to be the chosen methodology for cargo ships whereas CNG is more feasible for shorter routes where frequent refuelling is accepted (Stuer-Lauridsen et al., 2010). The bunkering time needed is shorter for CNG and is easily available from existing infrastructure for domestic use. However, both technologies require investments to be made on infrastructure and logistics. LNG refuelling and storage require special cryogenic equipment and safety procedures, whereas land transportation use has proven that CNG refuelling is safe and simple. Furthermore, LNG requires extra cost in order to be kept at liquid form.

### **1.4.2 CNG fuelled ships**

The first classed ship approved to run on CNG is the 8140 DWT limestone carrier “Accolade II”. It was built in Australia in 1982 and it is classed by Lloyd’s Shipping Register. It belongs to Adelaide Brighton Cement and it is powered by two dual-fuel engines.

CNG is stored in 21 cylinder tanks at pressure of 160 bars located in a compartment in the bow of the ship. Each tank is measured 9m length and 0.5m diameter and is installed vertically. According to Mosaad (2013), Lloyd's Register accepted the design provided that the ship operates in daytime only, refuelling takes place only at night, CNG tanks are placed away of accommodation and a periodic survey of gas fuel system and equipment will be carried out.



**Figure 1-4 The 8140DWT limestone carrier "Accolade II" (L=108m, B=23m, T=6.1m)  
(ShipSpotting.com, 2015a)**

In 1985, MV Klatawa became the first vehicle/passenger licensed to operate on dual fuel. It was built in 1972 for the Ministry of Transport and Highways in British Columbia, Canada (Einang and Haavik, 2000). The ferry has a capacity of 26 cars and 146 passengers and it was operating on the route Albion - Fort Langley on Fraser River until July 2009. The 2 Caterpillar 3406-B engines (650 HP in total) were converted to dual fuel engines and 8 aluminium hoop wrapped cylinders were placed in two compartments (one for each engine) on main deck for CNG storage. Refuelling was scheduled for every 4.5 hours for 3-4 minutes each time (M.D.A. Marine Design Associates, 2000). As reported by Einang and Haavik (2000), the on-shore compressor station store the gas at 250 bar filling on board storage to about 160 bar. Gas storage, gas piping, and engines were arranged on main deck for safety. Due to significant cost savings achieved by the conversion of MV Klatawa, owner decided to convert the sister ferry MV Kulleet to natural gas operation in 1988 (Mosaad, 2013). MV Kulleet has 4 CNG cylinders made of steel, so the investment costs were reduced (Einang and Haavik, 2000).

Mosaad (2013) mentions two additional cases of CNG usage for propulsion. The first case is about two canal boats in Amsterdam, which consumes minimal amounts of fuel due to low operating speed. The second case refers to a passenger ferry in the harbour of Norfolk, Virginia, USA that was put into service in 1995. Both cases had the reduction of emission as main motive factor.



According to Yang and Hu (2010), on 2009 the world's first commercial single CNG fuelled ship, MV NP Jenjosh, was delivered to the owner, Jenjosh Group based in Thailand. The ship is classed by China Classification Society (CSS) and it operates on the route of Chao Phraya River and Gulf of Thailand as a small open-top containership. The entire route lasts about 8 hours. The ship is designed with one cargo hold and two separate quarters of aft and fore parts. The CNG storage tanks are arranged inside two 20ft containers (one port and one starboard) mounted on main deck of the aft part. Yang and Hu (2010) state that exceptions on safety requirements (e.g. requirements that cover gas fuel storage, piping and rescue conditions) have been made because the ship operates mainly in a river.



**Figure 1-5** The containership MV NP Jenjosh (ShipSpotting.com, 2015b)

Another instance of usage of CNG as fuel in shipping industry is the seventh of the Urban Sprinter 2000 series of passenger ferries (HHP Insight, 2014b). It is an aluminium double ended ferry designed by CoCo Yachts Holland and build in Afai Southern Shipyard in China (HHP Insight, 2013). It possesses Caterpillar 3512 engines converted for dual fuel operation, which will use 70% gas and 30% diesel to propel the ship up to 18 knots. The 78.4m long ferry is able to carry 2000 passengers and it is operating in the route Rio de Janeiro – Niteroi. The six remaining ferries are designed in a way to be able to be retrofitted for use of CNG in the future (Marine Log, 2014b).

The first CNG fuelled tug is intended to be launched in 2016. It is designed by Damen Shipyards in collaboration with the engine manufacturer MTU Friedrichschaffen and Danish company Svitzer (Damen, 2014). It will have a 2000 kW MTU gas engine which will comply with IMO Tier 3 emission legislation (Marine Log, 2014a).

In 2016, the first European ferry to sail on CNG, “Texelstroom”, was built at the LaNaval shipyard in Spain (NGV Global News, 2015) and is classed by Lloyd's Register (LR.com, 2016). The ship is 135m long and 28m wide and it is designed by “C-Job” and “Oliver Design” (ship-technology.com, 2017). It is a double ended ferry operating between the port of Den Helder and the island of Texel at the north of The Netherlands (HHP Insight, 2014a). The ship, which is able to carry 1750 passengers and 350 vehicles, is fitted with 2x2000kW dual fuel 12DZD engines by Anglo Belgian Corp and it has a supporting solar

panel system to reduce the consumption of fossil fuels (HHP Insight, 2015). The German company Xperion is the manufacturer of the Type IV (polymer liner) CNG tanks, which are installed on the top deck (ship-technology.com, 2017).



**Figure 1-6** The CNG-fuelled ferry "Texelstroom" (ship-technology.com, 2017)

### **1.4.3 Rules and Standards for tank location and arrangement on ship**

IMO adopted the IGF Code (Gas and low-flashpoint fuels code) on 2014. The Code addresses all areas that need special consideration for the usage of low flashpoint fuels and provides mandatory provisions for the arrangement, installation, control and monitoring of machinery, equipment, and systems needed. The Code applies to new ships and to existing ships converting from the use of conventional oil fuel to the use of gas or other low-flashpoint fuels (I.M.O., 2014). The Classification Societies have published guides for classification of gas fuelled ships based on IGF code. Some of the more important requirements are summarized below.

#### **1.4.3.1 ABS**

American Bureau of Shipping has published "Guide for Propulsion and auxiliary systems for gas fuelled ships" (A.B.S., 2014a). Section 2/2.2 regulates gas storage tanks location and arrangement of spaces. ABS accepts CNG storage tanks stored above deck level if they are located in such a way to facilitate sufficient natural ventilation and are located at least  $B/5$  from the ship's side. For ship's other than passenger ships a tank location closer than  $B/5$  but nowhere less than 800mm from the ship's side may be accepted, where  $B$  is the

greatest moulded breadth of the ship at or below the deepest draught (summer load line draught). Additionally, the gas storage tanks are to be shielded with class A-60 insulation towards accommodation, service spaces etc.

Storage of compressed natural gas on enclosed spaces would be acceptable provided that adequate means to depressurize the tank in case of fire, a fixed fire extinguishing system and means to relieve pressure resulting from a catastrophic failure are provided. In addition, all surfaces within such enclosed spaces are to be provided with thermal protection against any high pressure gas leakage and resulting condensation. The location of gas storage tanks should be as close as possible to the ship centreline and minimum the lesser of  $B/15$  and 11.5m from the ship's side and minimum the lesser of  $B/15$  and 2m from the bottom plating and nowhere to be less than 800mm from the shell plating. For ships other than passenger vessels or where gas storage tanks are located adjacent to accommodation, service or control stations, the gas storage tanks may be located closer than  $B/5$  from the ship side provided that additional criteria are applied (minimum the lesser of  $B/15$  and 2m for the bottom plating and nowhere less than  $d$  where  $d$  is depended from the 100% of the gross design volume of the individual storage tank at 20°C). In all cases fuel containment system are not to be located adjacent to category A machinery spaces and other high fire risk spaces. The separation is to be at least 900mm by means of a cofferdam.

#### 1.4.3.2 *BV*

Bureau Veritas' "Safety Rules for Gas-Fuelled Engine Installations in Ships" Chapter 8 is dedicated to gas fuel storage tanks (B.V., 2011). Storage on open deck for compressed gas is acceptable. The gas tanks and equipment are to be sufficiently naturally ventilated and the gas tanks are to be located at least  $B/5$  from the ship's side. For ship's other than passenger vessels a tank location closer to ship side but not less than 760mm may be accepted and approved by BV. Tanks located on open decks are to be protected against mechanical shocks and from green seas. Section 8.3 also denotes additional measures to protect against gas leakage and fire damage.

According to section 8.5, storage of compressed gas with a pressure higher than 10 bar is normally not acceptable in enclosed spaces, but may be permitted after special consideration provided that adequate means to depressurize the tank in case of fire and a fixed fire extinguishing system are installed and all surfaces inside the tank room are provided with thermal protection against any lost high pressure gas and resulting condensation. The gas tank shall be located as close as possible to centreline, minimum the lesser of  $B/5$  and 11.5m for the ship side, minimum the lesser of  $B/15$  and 2m from the bottom plating and not less than 760mm from shell plating. For ships other than passenger ships and multi-hulls a tank location closer than  $B/5$  from the ship side may be accepted provided that additional conditions are satisfied. The aforementioned section includes additional requirements for the construction and arrangement of the tank room and bilge suction of the tank room.

#### 1.4.3.3 ClassNK

Class NK has published “Guidelines for gas fuelled ships” (ClassNK, 2016). Chapter 5 of the guideline includes functional and general requirements for the location and arrangement of gas tanks. The fuel tanks shall be located in such a way to minimize the probability to be damaged by a collision or grounding. For this reason, the fuel storage tanks shall be located at a minimum distance of  $B/5$  or 11.5m, whichever is lesser, from the ship side. In no case shall the boundary of the ship fuel tank be located closer to the side shell or aft terminal of the ship than as follows:

- For passenger ships  $B/10$ ; and
- For cargo ships:
  - For  $V_c$  below or equal  $1,000 \text{ m}^3$ , 0.8 m;
  - For  $1,000 \text{ m}^3 < V_c < 5,000 \text{ m}^3$ ,  $0.75 + V_c \frac{0.2}{4,000}$  m;
  - For  $5,000 \text{ m}^3 \leq V_c < 30,000 \text{ m}^3$ ,  $0.8 + \frac{V_c}{25,000}$  m; and
  - For  $V_c \geq 30,000 \text{ m}^3$ , 2m;

where  $V_c$  corresponds to 100% of the gross design volume of the individual fuel tank at 20°C, including domes and appendages.

Additionally, the lowermost boundary of the fuel tank shall be located above the minimum distance of  $B/15$  or 2 m, whichever is less, measured from the moulded line of the bottom shell plating at the centreline and the fuel tanks shall be abaft a transverse plane at  $0.08L$  measured from the forward perpendicular in accordance with SOLAS regulation II-1/8.1 for passenger ships, and abaft the collision bulkhead for cargo ships. The guideline also includes an alternative calculation method for the above arrangements. Last but not least, fuel storage tanks or and equipment located on open deck shall be located to ensure sufficient natural ventilation, so as to prevent accumulation of escaped gas.

#### 1.4.3.4 DNV-GL

“DNV-GL Rules for Classification of Ships” Part 6 Chapter 2 Section 5 is referred to gas fuelled ship installations (DNV-GL, 2016). According to paragraph 4.1 of section 5, fuel containment system shall be located and arranged in such a way to minimize certain risks. In particular, these risks are the risk of excessive heat input from a fire, the risk of mechanical damage from ship and cargo operations and green seas, and the risk of mechanical damage from explosions. DNV-GL proposes to minimize the above risks either by locating the gas storage tanks away from such hazard or by providing mechanical protection. Additionally, the fuel containment system shall be designed and arranged not to cause damage to other structures due to low temperature leakage. For gas storage tanks requiring a complete or partial secondary barrier, fuel storage hold spaces shall be segregated from the sea by a double bottom and the ship shall also have a longitudinal bulkhead forming side tanks.

As mentioned in paragraph 4.1 of section 5, compressed natural gas shall not be stored below deck, but this may be accepted on case-by-case basis. In addition, a fuel gas containment system located in enclosed spaces shall be gas tight towards adjacent spaces and the space containing gas storage tanks shall be separated from the machinery spaces of

category A or other rooms with high fire risks by a cofferdam of at least 900 mm with fire insulation.

#### 1.4.3.5 *Lloyd's Register*

Section 5.3 of “Rules and Regulations for the classification of natural gas fuelled ships” of Lloyd’s Register is dedicated to gas storage tank location (Lloyd's Register, 2015). Gas storage tanks located on open deck are to be protected from possible mechanical damage and the area to be naturally well-ventilated. The storage tanks can be located in enclosed or semi-enclosed hold spaces. Gas storage tanks are to be located as close as possible to the centreline of the ship. No part of the outer shell of the tank and tank master isolation valve is to be less than a distance of:

- B/5 from the ship side, where b/5 is measured inboard from the ship’s side at right angles to the centreline at the level of the summer load line. At any other point the distance from the ship’s side is not to be less than 2 m for passenger ships and ships with tanks located below accommodation, and 0.8m for other ship types; and
- A minimum of 2 m from the bottom of the ship.

The value of B is the greatest moulded breadth of the ship in metres. The 2 m and 0.8 m distances are to be measured from the shell plating to the outer shell of the gas storage tank and from the shell plating to the tank master isolation valve.

In addition, section 5.3 includes requirements for the fuel storage hold space such as to maintain its integrity in the event of a release of gas from the primary barrier, to be separated from machinery spaces and other ‘high fire risk’ areas and shall not be adjacent to, or below accommodation spaces, service or control stations where practicable. Although, gas storage tanks located below or adjacent accommodation may be accepted provided that additional protection measures are considered. These considerations are to include but shall not be limited to increased structural protection of tanks from collisions and groundings, increased protection of accommodation from gas fires and enhanced navigational aids to reduce likelihood of collisions and groundings.

## 1.5 Scope of the thesis

The climate change is a phenomenon, which affects the way and the quality of living of every human being on this planet. The recent international agreements (Paris MoU, Kyoto Protocol), which focus on the restriction of emissions responsible for the phenomenon, affect any human activity. In that context, the International Maritime Organization (IMO) has implemented regulations limiting the permissible quantities of SO<sub>x</sub> and NO<sub>x</sub>, which a ship can emit. As a result, the use Heavy Fuel Oil, which has been the main fuel for the propulsion of ships, has been restricted.

Nowadays, the maritime industry is at crossroads. The one possible alternative is to continue the use of fuel oil either by installing special equipment, in order to restrict the emissions or by using a more expensive quality of fuel oil, which contains less sulphur. The other alternative is the use of natural gas as a fuel, whose use has been tested before in domestic use and the automotive industry. However, in order to be used in the maritime

industry, certain issues must be taken into account.

One of the most important issues is its onboard storage. The natural gas can be stored in two different ways. The first is being used in the maritime industry, in order to carry huge quantities of natural gas from the origin countries to consuming countries. The natural gas is carried in a liquefied state (LNG) in specially designed insulated tanks capable to keep the temperature below  $-162^{\circ}\text{C}$  and the pressure above 5 bars. This demands special equipment in order to prepare the natural gas for storage and to maintain it in that state throughout the voyage, increasing in that way the investment cost for dedicated shore infrastructure and the operating cost of the ship. The other way has been successfully used in the automotive industry and in some cases in the maritime industry. The natural gas is stored in a pressurized state at the environment temperature. However, the pressure must exceed the 200 bars in order to store sufficient quantity of natural gas. Therefore, the gas must be stored in tanks capable to withstand these pressures.

Such tanks have a cylindrical shape and are constructed by aluminium, which is wound with a carbon fiber reinforcement. The recent years, car companies have invested in research of efficient designs of such pressure vessels, in order to minimize their weight and their manufacturing cost. However, the maritime industry cannot use those designs as the power for propulsion of a ship demands a lot more quantities of fuel to be stored onboard, thus the dimensions of the storage tanks must be a lot greater. Therefore, an independent research must be made.

As there is no analytical expressions to calculate the required design parameters, the only options to do so are the experimental testing and the numerical simulation. The experimental testing requires the manufacturing of several slightly different designs and their destruction. Thus, this procedure is significantly costly. The research cost can be decreased with the use of simulation software, which utilize the Finite Element Method (FEM), for the modelling of the construction and the evaluation of its strength and structural response. The evolution of such simulation software (like ANSYS and Abaqus which were used in this diploma thesis) has given the opportunity to predict the performance of the construction accurately without destructive testing. However, the classification societies (ABS, DNV-GL etc.) still require the experimental testing of the final design in order to approve its use. Although the numerical simulation cannot yet replace completely the experimental testing, it can reduce the design cost by determining effectively and precisely an initial design of the construction, without the need of manufacturing and destruction of a series of different test specimens.

The goal of this diploma thesis is to propose a feasible design of a pressure vessel capable to be used in marine applications. In order to do so, certain steps must be followed. Firstly, the different design and manufacturing parameters of a pressure vessel manufactured with the filament winding method must be determined. This knowledge was derived by studying relative literature and it was used for a better accuracy of the simulation, which followed. However, in order to end up to the optimal design, the importance of the different parameters and their impact on the strength and structural response of the construction must be investigated. This study resulted in a design, which complied with the regulations and the operating requirements and it had the minimum required thickness and as a result the minimum weight.

This diploma thesis was conducted in Shipbuilding Technology Laboratory of the National Technical University of Athens. The motivation of the Laboratory is to improve its knowledge on the designing and manufacturing of composite pressure vessels and by using its prior knowledge on the mechanics of composite material and composites numerical modelling, to deliver feasible and effective alternatives to the maritime industry.



## Chapter 2 CNG Pressure Vessels

### 2.1 General

For the transportation of Natural Gas at a gaseous state (CNG), special tanks able to withstand internal pressure above 200 bars are needed. Such tanks are called pressure vessels and they are usually cylindrical. In fact, they consist of a cylindrical portion, which is covered at both ends with end caps called domes or heads. The shape of the domes is usually spherical or elliptical, but there are also other special shapes like geodesic-isotenoid design (Zu, 2012). Each dome has an opening at its top called polar boss opening. The optimal shape for domes from isotropic material is the spherical, but this does not apply to fiber reinforced domes due to the anisotropic character of the material (Zu, 2012).



**Figure 2-1** The cylindrical portion (background) and the dome (foreground) with its polar boss opening of a Type III pressure vessel. ([www.cngschool.com](http://www.cngschool.com))

The pressure vessels are being used in the transportation sector, especially in automotive industry, as the use of CNG as a fuel offers a low emission alternative to the traditional fossil fuels. Some of the limitations for its widespread use are the weight, volume and cost of the pressure vessels. For this reason, the performance of a pressure vessel is calculated by means of the following index (Funck and Fuchs, 2001):

$$I = \frac{P V}{W}$$

where  $P$  is the burst pressure,  $V$  is the containing volume and  $W$  is the weight of the pressure vessel. For that reason, certain car manufacturers, like Mercedes (Piellisch, 2012) and Audi (Audi, 2013), are preferring to install in their cars Type IV pressure vessels, which are manufactured completely with non-metallic materials, in order to reduce the weight.

In fact, the pressure vessels are categorized in different types based on the material with which they are manufactured. The Type I pressure vessels are manufactured solely from



metal alloys. The alloy is usually steel or aluminium. They are the heaviest and the least expensive of all the other pressure vessel types. The next type is the Type II, which is manufactured with both metal alloys and composite material. In particular, the pressure vessel is similar to the Type I, with the difference that its cylindrical portion is reinforced with glass or carbon fibers wound in the hoop direction. In this way, the total thickness of the pressure vessel can be reduced, as the composite reinforcement increases the total strength of the construction, thus the total weight is lower than the weight of the respective Type I pressure vessel. In addition, as Type III are classified the fully wrapped pressure vessels. By that, it is meant that a thin metal liner is reinforced at its entire surface with CFRP or GFRP. The metal liner is used for insulation, in order to avoid gas leakage, and the fiber reinforcement provides the structural strength of the construction. The liner can also bear a small part of the load (Shen, 1995). This type is lighter than the other two types, but is also more expensive. The last type of pressure vessel (Type IV) includes vessels that are constructed solely by non-metallic material. The liner is made by plastic (polyethylene or nylon) and it is again reinforced with GFRP or CFRP (Bakar et al.), but it cannot carry any part of the load. In this way, the total weight of the pressure vessel is further reduced. According to (Funck and Fuchs, 2001), this reduction can reach up to 75% comparing a Type II hoop wrapped steel liner with a Type IV pressure vessel.



Figure 2-2 Schematic representation of the four types of pressure vessels and their main characteristics (Dillard, 2015)

## 2.2 Manufacturing of pressure vessels with the filament winding method

The composite pressure vessels are being manufactured with the filament winding fabrication technique. The concept of the method is that resin-impregnated fibres are wound around a rotating mandrel. Then, the resin is cured by usually placing the part in an oven or

under radiant heaters (Wikipedia, 2005a). Finally, either the mandrel remains as a liner (mainly for pressure vessels) or it is removed. This method is one of the oldest composite manufacturing methods and it can be fully automated, offering a cost-effective alternative for mass production (Zu, 2012).

A simple filament winding machine consists of the spindle, where the rotating mandrel is placed, and the carriage, from where the fibres are fed to the mandrel. The fibre rovings are taken by spools and they are usually combined together to form a continuous fibre bundle. The total width of the fibre bundle is an important manufacturing parameter, both for the manufacturing process and the speed of the process, and it is called bandwidth. Then, the fibre bundle passes through a resin bath and passing through the feed-eye of the carriage is placed on the mandrel's surface.

The minimum number of axis of motion of the machine is two. The first is the rotation of the mandrel and the second is the horizontal movement of the carriage. However, for more accurate placement of the fibre bundle, especially at the ends of the domes, two additional degrees of freedom are needed. The third axis is usually the perpendicular to the mandrel rotation axis movement of the carriage and the fourth is the rotation of the feed-eye (Shen, 1995). Nowadays, there are filament winding machines with up to 7 degrees of freedom (Zu, 2012).

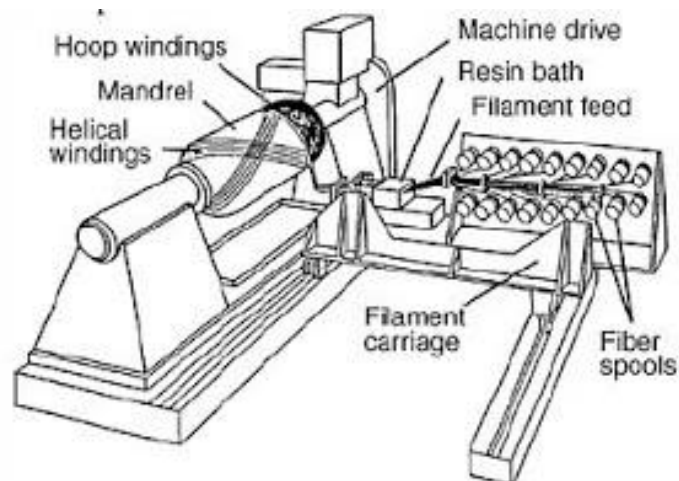


**Figure 2-3 Schematic representation of a simple filament winding machine (www.fibre-reinforced-plastic.com, 2009)**

There are three different winding patterns that can be used; the planar, the helical and the hoop winding. The selection of the appropriate winding pattern for each appliance is based on the shape of the wound geometry and the direction in which the reinforcement is more necessary. With the polar winding, the fibres are wound in a direction close to the longitudinal axis of the mandrel, thus the winding angle is less than 5deg. Therefore, the fibre rovings are passing close to the polar boss openings of the mandrel. The way that the fibres are placed create a reinforcement of a single layer for each completed polar winding pattern (Shen, 1995). On the other hand, the helical winding is used when the desired reinforcement orientation is between 5deg and 80deg with respect to the longitudinal axis of the mandrel. Due to the increased winding angle, the fibers are wound in alternating positive and negative

orientations, resulting in a double layered reinforcement for each completed winding pattern. The fiber bundle may pass around the polar boss openings, but it is not necessary (Shen, 1995). It is also used for the gradual transition from polar or helical winding to hoop winding without cutting the fibers by increasing gradually the winding angle. Finally, hoop winding are used to place the fibers close to 90deg with respect to the longitudinal axis. In fact, it can never be exactly 90deg as each fiber roving is placed adjacent to the previous winding pattern. The real winding angle is determined by the bandwidth and the diameter of the mandrel according to (Wang et al., 2011):

$$\alpha = \cos^{-1}\left(\frac{BW}{\pi D}\right)$$

where BW is the bandwidth and D is the diameter of the mandrel. It should be noted that the hoop windings are only applied to cylindrical or straight portions of the mandrel and result in a single layer reinforcement (Zu, 2012) (Shen, 1995).

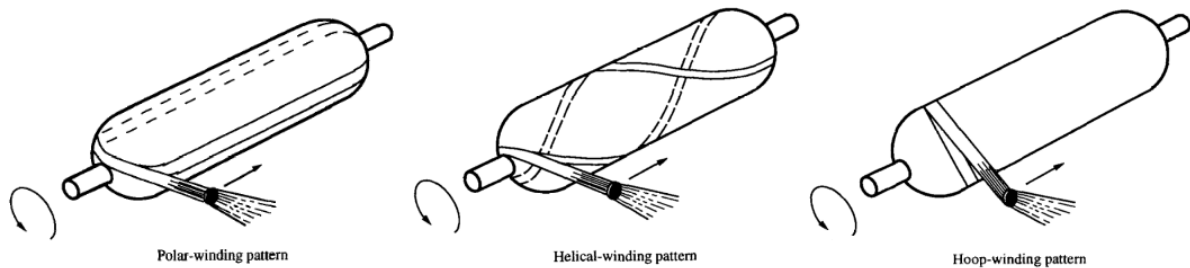


Figure 2-4 The three different winding patterns (Shen, 1995)

## 2.3 Rules and Standards for Designing, Manufacturing and Testing

### 2.3.1 The ASME Boiler and Pressure Vessel Code

The American Society of Mechanical Engineers has published standardizing rules for pressure vessels manufactured with composite materials. The fiber-reinforced pressure vessels are covered in Section X of the “Boiler and Pressure Vessel Code (BPVC)” (ASME BPVC Section X, 2015).

The code classifies the design for acceptance in three different classes. The Class I includes design that require a prototype testing to be accepted. The qualification pressure of the prototype must be at least 6 times greater than the design pressure. The design pressure must not be greater than 1 MPa for bag-molded, centrifugally cast and contact-molded vessels. For filament wound pressure vessels the design pressure must not exceed 10 MPa and for filament wound vessels with polar boss openings the maximum design pressure is limited to 20 MPa. The Class II pressure vessels are designed according to mandatory rules and acceptance test, which are included in the “BPVC Section X”. Finally, the Class III pressure vessels are qualified with prototype testing, where the minimum qualifying pressure must be at least 2.25 times the design pressure for vessels fabricated with carbon fibers and 3.5 times the design pressure for vessels fabricated with glass fibers. Hybrid designs can be

also qualified. The maximum design pressure must be greater than 20.7 MPa and less than 103 MPa.

The operating pressure of the CNG pressure vessels is usually over 20 MPa (200bar), so this thesis will concentrate solely in the Class III pressure vessels. The design and testing rules of Class III pressure vessels are presented in Mandatory Appendix 8 of the Code.

The appendix covers pressure vessels with both metallic and non-metallic liners. The metallic liners can be both load-sharing and nonload-sharing, whereas the non-metallic liners are always nonload-sharing. The metallic load-sharing liner must comply with the requirements of BPVC Section VIII, Division 3, whereas the metallic non-load sharing liners must comply with the requirements of BPVC Section VIII, Division 1,2, or 3. The burst pressure of a nonload-sharing liner shall be less than 10% of the nominal burst pressure of the finished vessel, whereas the respective burst pressure must not exceed 50%.

The general section covers also other aspects of the pressure vessel design and fabrication such as its service life, which shall be limited to 20 years, and the fabricator's and inspector's responsibilities. In the "Materials" section, the types of fibers and resins that can be used are presented. In addition, the codes with which the materials must comply and the certification tests of the materials are listed.

Finally, the qualification and production tests, which must be followed are described. For each test, the procedure and the acceptance criteria are described. These tests are the following:

- Hydraulic pressure test
- Hydraulic expansion test
- Burst test
- Fatigue test
- Temperature creep test
- Flaw test
- Leak test
- Torque test on vessel nozzle neck
- Penetration test
- Environmental test.

It should be noted that regular production tests are required to be contacted even after the qualification of the design. A burst test and a fatigue test must be contacted for one vessel per 200 finished vessels. If the production rates are less than 200 vessels per year, then a vessel must be tested each year.

## **2.3.2 Rules and Regulations of Classification Societies**

### **2.3.2.1 ABS**

"Guide for Propulsion and auxiliary systems for gas fuelled ships" (A.B.S., 2014a) of ABS regulates the design of CNG storage tanks. In Section 3.1, it is stated that for single fuel installations the fuel storage is to be divided in two or more tanks of approximately equal size located in different compartments. Section 3.1 contains also a summary list of plans and data to be submitted for approval by the society.

According to Section 3.4, the design of the storage tanks is to be in accordance with ABS's "Guide for vessels intended to carry compressed natural gases in bulk (CNG Guide)" (A.B.S., 2014b) and the tanks to be fitted with pressure relief valves with a set point below design pressure. The location of the outlet from the pressure relief valves is required to be at least  $B/3$  or 6m, whichever is greater, above the weather deck and 6 m above the working area and gangways. In addition, the outlets are to be located at least 10 m from the nearest air intake, air outlet or opening to accommodation, service or control space or other non-hazardous space and from exhaust outlet from machinery or from furnace installation.

In "Guide for vessels intended to carry compressed natural gases in bulk (CNG Guide)" (A.B.S., 2014b) the design of storage tanks are categorised as follows:

- Type 1 Cargo Tanks are metallic tanks with nominal diameter 200 mm (8 in.) or less with length-to-diameter ratio greater than or equal to 1000.
- Type 2 Cargo Tanks are metallic tanks with nominal diameters above 200 mm (8 in.) or greater with length-to-diameter ratio less than or equal to 100.
- Type 3 Cargo Tanks are tanks constructed from composite materials or combination of metallic and nonmetallic materials.
- Type 4 Cargo Tanks are tanks constructed with an inside metal liner and wrapped outside with high strength steel wires.

In Chapter 5 Section 1 of the Guide is stated that type 1 is to comply with Probabilistic Limit State Design, whereas type 2, 3, 4 are to be in accordance with a recognised pressure vessel code or in substantial agreement with a recognised pressure vessel code and any deviations from the latter are supported by Probabilistic Limit State Design outlined in Chapter 5 Appendix 1 of the Guide.

Chapter 5 Section 2 contains definitions used in the Guide such as the design pressure, the maximum allowed operating pressure (MAOP), the normal storage pressure and the burst pressure. In all cases, design pressure is not to be less than MARVS (maximum allowable relief valve setting of cargo tank). The normal operating pressure shall not exceed MAOP, which is less than design pressure.

Furthermore, chapter 5 of the Guide denotes the design loads (section 3) to be considered and the structural analysis to be followed (section 4). The structural analysis can be either deterministic or probabilistic with a goal to determine the suitability of the cargo tank under all operating conditions with respect to local yielding, plastic collapse, crack propagation, fatigue failure and burst. Other sections of the chapter regulate allowable stresses and corrosion allowances, thermal protection and insulation of cargo tanks and the installation and support of cargo tank.

Section 10 of chapter 5 is dedicated to cargo tank fabrication and testing. ABS states that all manufacturing and fabrication processes (welding, testing, inspection etc.) are to follow applicable standards/codes used in the design of cargo tanks. Welding, non-destructive testing and inspection are regulated at this section too. In addition, the pressure testing that is to be followed is described. Each cargo tank is to be pressure tested for acceptance. Type 3 and 4 tanks pressure testing procedures are to be developed and submitted for review and may include burst test. Type 1 and 2 tanks are to be subjected to a hydrostatic or hydro pneumatic test described. The tanks are tested at a pressure measured at the top of the cargo

tanks of not less than 1.25 times design pressure, but in no case during the pressure test is the calculated primary membrane stress to exceed 90% of the yield stress of the material. All new tank designs are to be prototype tested. A minimum of four cylinders are to be prototype tested. Type 3 tanks are to be tested for a combination of loads to prove fatigue and burst performance. The prototype testing is to be carried out after pressure testing.

Regarding materials of construction of tanks, chapter 7 of the Guide state that type 3 and 4 CNG tanks designed and built using metallic/composite/hybrid materials will be specially considered and are to be designed and constructed in accordance with the requirements of the ASME Boiler and Pressure Vessel Code, Sections VIII and X or equivalent.

#### 2.3.2.2 *BV*

According to BV's "Safety Rules for Gas-Fueled Engine Installations in Ship"(B.V., 2011) Section 2 Paragraph 8.2, the design and construction of CNG tanks are to comply with recognized codes and standards. In addition, the tanks are to be fitted with pressure relief valves with a set point below the design pressure of the tank and an outlet located as required by ABS. As stated at section 7.2 tank and testing is to be in accordance with IGC Code Chapter 4.10 and 4.11 or equivalent standards accepted by BV.

BV has published "Classification of Compressed Natural Gas Carriers" guide (B.V., 2007). Section 4.2 of the guide defines the types and categories of gas tanks. Type 2 are cargo tanks consisting of assembly of multiple individual vertical or horizontal cylindrical pressure vessels connected by a common manifold and supported individually inside the cargo hold up to first stop valve and can be metallic, composites or hybrids. There are two categories of cargo tanks; type B and type C. Type B are tanks which are designed using model tests, refined analytical tools and analysis methods to determine stress levels, fatigue life and crack propagation characteristics, whereas type C are tanks meeting pressure vessel criteria. Other subsections of section 4 of the guide contain information about the design loads to consider for the design, the structural analysis to be followed and materials to be used.

Section 4.10 of the aforementioned guide regulates the construction and testing of the tanks. It summarizes the welding and manufacturing procedures to be followed and denotes the minimum required controls to be carried out with non-destructive testing. In addition, each independent tank is to be subjected to a hydrostatic or hydro pneumatic test. For type B tanks, the tests are to be performed so that the stresses approximate to the design stresses and that the pressure at the top of the tank corresponds at least to the MARVS. The maximum primary membrane stress or maximum bending stress in primary members under test conditions are not to exceed 90% of the yield strength of the material (as fabricated) at the test temperature. Type C independent tanks are to be subjected to hydrostatic test in accordance with recognized standards, but in no case during the pressure test the calculated primary membrane stress at any point is to exceed 90% of the yield stress of the material.

### 2.3.2.3 *Class NK*

Chapter 6 of “Guidelines for gas fuelled ships” (ClassNK, 2016) contains the conditions to be satisfied in order to Class NK approve the tank design. A general requirement is that the maximum allowable working pressure (MAWP) of the gas tank shall not exceed 90 per cent of maximum allowable relief valves setting (MARVS). In section 6 of chapter 6 it stated that tanks shall be fitted with pressure relief valves with a set point below the design pressure of the tank and with outlet located at least 10 m from the nearest air intake or outlet or opening to accommodation, service or control spaces or exhaust outlet of machinery installations.

Chapter 16 contains regulations for material testing, manufacturing and welding procedures, non-destructive testing, and inspection. Manufacturing, testing, inspection, and documentation shall be in accordance with recognised standards and the requirements of Class NK. Non-destructive testing is required at least for all butt welds over their full length, all welds over 10% of their length and reinforcement rings around holes, nozzles, etc. over their full length.

Type C independent tanks shall be subjected to hydrostatic test at a pressure measured at the top of the tanks, of not less than 1.5 times design pressure. In no case during the pressure test shall the calculated primary membrane stress at any point exceed 90% of the yield stress of the material. The pressure shall be held for 2 hours per 25 mm of thickness, but in no case less than 2 hours. After completion and assembly, the tank shall be subjected to a tightness test, which may be performed in combination with the pressure test.

### 2.3.2.4 *DNV-GL*

According to Part 6 Chapter 2 Section 5.4.3 of DNV-GL’s “Rules for Classification of Ships” (DNV-GL, 2016), tanks for compressed natural gas shall be certified as Class I pressure vessel in accordance with Pt.4 Ch.7, or they may be alternatively certified based on requirements in Pt.5 Ch.8. The set point of the pressure relief valves shall be below the design pressure.

Part 5 Chapter 8 of DNV-GL’s “Rules for Classification of Ships” concerns the compressed natural gas tankers. Section 1.3.1 limits maximum allowable operating pressure to 95% of the design pressure. According to Section 5 gas tanks are divided in 3 types; coiled type, cylinder type and composite type tanks. Subsection 4 of Section 5 contains design and testing regulations about composite type tanks. A typical composite type tanks is consisted by an inner liner (fluid barrier that it may also be designed to carry part of the loads), the composite laminate that carries the pressure loads and the outer liner that is a protective layer against external loads/ environments and typically it does not carry any loads. Subsection 4.2 denotes the potential failure modes (bursting, buckling etc.), which shall be considered in the designing, the fatigue calculations to be carried out and the operating temperatures to be defined. In addition, it is stated that the maximum operating pressure should be 5% or more below the design pressure.

Each tank shall be pressure tested at a test pressure equal to 1.3 times the design pressure. The tank shall be tested on the ship after the installation at the same pressure as a

final acceptance test. Furthermore, a full-scale prototype test is required. Section 4 contains also the design requirements for the inner and the outer liners.

## **2.4 Literature Review**

The increased environmental awareness has driven the maritime industry to adopt environmentally friendly propulsion alternatives. A feasible alternative is the use of CNG (Compressed Natural Gas) as a fuel. CNG has been successfully used in the automotive industry. The annual growth of the number of natural gas vehicles (NGVs) has been 24% (Khan et al., 2015). It is an option, which ensures full compliance with the MARPOL Annex VI as it produces low NO<sub>x</sub> and SO<sub>x</sub> emissions. Another advantage is that it can be burned in existing diesel engines after slight modifications (Adamchak and Adede, 2013). However, its storage differs from the storage of traditional marine fuels. CNG is stored in specially designed pressure vessels able to withstand operating pressures above the 200bar.

Such pressure vessels have been designed and manufactured for use in the automotive industry, the aerospace industry, and other sectors. The same designs are also used for the transportation of hydrogen and other gasses under high pressure. However, the use of CNG in the maritime industry demands the manufacturing of a lot bigger pressure vessels than those are used in the automotive industry.

The use of composite material for the fabrication of pressure vessels has reduced the total weight compared to full metallic pressure vessels by 75% (Funck and Fuchs, 2001), but it has also made their structural design more complex due to the anisotropic nature of the material. The stress analysis can be made either with analytical calculations or with Finite Element Analysis.

The analytical calculations can be carried out only under certain circumstances (dome shapes, winding trajectories). Koussios (2009) searched for the dome shapes that maximize the pressure vessel performance index with the use of integral optimization. In this way, the dome shape is derived by the optimization procedure, so it cannot predefined. In addition, the aforementioned analysis is directly depended on the winding patterns that will be followed in the manufacturing procedure. Vasiliev et al. (2003) also approached the structural design of pressure vessels with analytical methods. Their analysis aimed to propose alternatives for more reliable designs of pressure vessels for commercial use. Firstly, they proposed various optimal shapes for geodesic isotensoid pressure vessels, which are the most popular pressure vessels, based on the anisotropic factor of the material and the ratio of the radius of polar boss opening to the radius of the dome. However, they state that a geodesic isotensoid design remains unreliable as it is highly affected by manufacturing and operational imperfections. As a more reliable alternative, they proposed the circumferential winding of pressure vessels with angle-ply tapes, because the circumferential winding is simpler and it can be done with filament winding machines with 2 degrees of freedom reducing, thus the deviation of the final product from the design would be small.

Numerical methods have been widely used for the structural design and the stress analysis of pressure vessels. Utilizing the Finite Element Method, Kabir (2000) examined the effect of different dome shapes on the stresses distribution at the dome areas. He also examined the same effect of different metallic liners by creating three models with no liner,



elastic liner and elasto-plastic liner respectively. His analysis used geodesic trajectories with increasing thickness at the dome area and the pressure vessel was intended to operate at 22MPa with a safety factor equal to 1.5. The Finite Element Method was also used by Liu et al. (2010) for the nonlinear analysis of the structural response of a CFRP pressure vessel at working pressure, hydraulic testing pressure and destructive pressure. With the use of numerical methods Xu et al. (2009) and Liu et al. (2012) implemented progressive failure analysis on composite pressure vessels intended to store high-pressured hydrogen. Xu et al. (2009) used four different failure criteria for their analysis. They used the maximum stress criterion, the Hoffman failure criterion, the Tsai-Wu criterion, and the Tsai-Hill criterion. Comparing the results with experimental results, they concluded that the numerical results were in agreement with the experimental results for the four of the criteria, but the Tsai-Wu failure criterion led to most accurate failure pressure among all failure criteria. The results derived by FEM analysis can be also used for the implementation of genetic algorithms or other optimization methods in order to search for an optimal pressure vessel design (Kim et al., 2005b) (Kim et al., 2005a).

The increase of the demand for lightweight CNG pressure vessels, mainly for the automotive industry, led Velosa et al. (2009) and Barboza Neto et al. (2011) to investigate the feasibility and structural behaviour of Type 4 pressure tanks. Velosa et al. (2009) examined the mechanical behaviour of pressure vessels with a liner manufactured with HDPE (high-density polyethylene). Firstly, they predicted the internal pressure that the liner standalone can withstand by creating a FEM model of the liner in Abaqus software. Then, they modified the model to include the composite reinforcement, in order to analyse the behaviour of the entire construction. Their numerical results were verified by experimental testing, which was carried out later. Respectively, Barboza Neto et al. (2011) using both experimental and numerical analysis made the structural design of a CNG pressure vessel able to withstand a working pressure of 20.7MPa and a burst pressure of 40MPa manufactured with a plastic liner. The material that was used for the construction of the liner was a 95wt.%-5wt.% mixture of LLDPE (low linear density polyethylene) and HDPE. The liner was manufactured with the rotational moulding method. The liner was analysed separately both with Finite Element Analysis and experimental testing and it was verified that the central section of the liner is its weakest region, as there happened the brittle fracture. It should be noted that the pressure vessel is designed with two unequal domes, as there is polar boss opening only at the one dome. In addition, non-geodesic trajectories were used for the winding of the structure.

The popularity of the use of FEM for the structural analysis of composite pressure vessels as well as their complex geometry has driven the manufacturer of the commercial FEM program Abaqus to include in the software an add-in tool dedicated for this purpose. The add-in is called “Wound Composite Modeller” and it has been used by Gray and Moser (2004), Willardson et al. (2009) and Barboza Neto et al. (2011) in their research. Willardson et al. (2009) compared the results derived by FEM analysis with the results derived by experimental testing of the designed pressure vessels and found a 7.6% difference between the actual burst pressure and the burst pressure that had been predicted with the FEM analysis. The FEM analysis was, then, adjusted and repeated for lower elastic modulus in the fibre direction, according to the experimental testing, and predicted the burst pressure accurately. In this way, it is indicated that the “Wound Composite Modeller” can be used for

a moderately accurate prediction of the structural response of a pressure vessel if it has accurate input.

However, in order to create a representative simulation of the structural response of a composite pressure vessel, certain designing and manufacturing parameters must be understood. One of the main aspect of the construction that must be simulated accurately is the fiber trajectories along the dome. The winding angle of the fibers plays an important role in the structural response of the pressure vessel, as the material is anisotropic and it is stiffer in the direction of the fibers. Although, the winding angle is constant at the cylindrical portion of the tank, this does not happen at the dome regions. The winding angle of the fiber is increasing as it approaches the polar boss opening, where it becomes equal to 90deg and returns towards the cylindrical portion from the opposite side of the dome. The way that the fiber increases from the winding angle at the cylindrical portion up to 90deg can alter the stress distribution and the mechanical behavior of the construction at that region. Therefore, it is vital to be included precisely in the simulation. To do so, analytical formulations describing the trajectories can be used. Koussios (2004) and Zu (2012) have included in their works analytical formulations describing a vast variety of different type of trajectories. This formulations do not describe solely fiber trajectories of pressure vessels, but they also describe trajectories manufactured with the filament wound technique around various shapes. Numerous works have been made on the topic from the same authors or others, covering relative to the topic subjects, like the correlation between the fiber trajectory and the winding patters (Koussios et al., 2007) (Johansen et al., 1998) (Beukers et al., 2007) or the optimization of filament wound parts based on the non-geodesic trajectories (De Carvalho et al., 1995). A notable work concerning the fiber trajectories was made by Zu et al. (2010). They used the continuum theory in order to quantify the improvement of the structural performance of a dome that can be achieved with the use of non-geodesic trajectories. They concluded that the performance of the dome improves for greater values of the maximum static friction coefficient, thus for trajectories that differ a lot from the geodesic trajectory. A newer research on the subject was also made, which was dedicated on the dependence of the performance of pressure vessels from the maximum static friction coefficient, verifying the conclusions of the first work (Zu et al., 2016). It is indicated, in this way, that the maximum static friction coefficient is a vital parameter for the structural design and manufacturing of a pressure vessel.

For this reason, Wang et al. (2011) and Koussios and Bergsma (2006) searched for the manufacturing parameters that affect the maximum static friction coefficient. Both teams used experimental testing in order to measure the value of the coefficient under certain conditions. They focused on the effect of the roving tension, the fiber material, the bandwidth, the quality and the material of the underlying surface and the viscosity of the resin. It was obvious from both the works that there are parameters irrelevant with the maximum static friction coefficient (winding speed, roving tension) and there are other parameters which affect it slightly (fiber material) or highly (bandwidth, viscosity of the resin, underlying surface).

Another aspect of a pressure vessel that has to be included in the simulation in order to be precise is the increase of the composite thickness along the domes. As the fibers are wound along the dome, they are concentrated in a smaller radius, causing overlapping of the

fibers. Therefore, the thickness of the dome increases near the polar boss opening. This phenomenon changes the local stiffness of the dome and it was described with analytical formulations by Koussios (2011). However, the applicability of these formulations is limited to geodesic trajectories. In fact, there are no analytical formulations that describe the thickness build-up along the dome derived by non-geodesic trajectories. For this purpose, only certain approximations can be used. In addition, the thickness build-up changes the fiber trajectory of the overlapping layers, as each new layer is wound over an altered meridian profile, thus the fiber trajectory of each layer is slightly different. The effect of this phenomenon on the structural response of a pressure vessel was studied by Park et al. (2002).

## Chapter 3 Theory of Filament Winding

### 3.1 Winding Trajectory

#### 3.1.1 Geodesic and non-geodesic trajectories

One of the main parameters of the design of a pressure vessel is the winding angle of the fibres. The winding angle is the angle between the fibre path and the longitudinal axis of the cylinder (for cylindrical shapes) or the meridian profile, which crosses the particular location at which the winding angle is measured, of a general shell of revolution (Peters et al., 2011). The winding angle is usually denoted with the Greek letter  $\alpha$  and this symbolism will be followed throughout this thesis. The Figure 3-1 shows the fiber path along a general shell of revolution and the winding angle at a particular location. In this figure, the radius of the polar boss opening is symbolized with  $r_0$  and the radius of the equator of the shape with  $R$ .

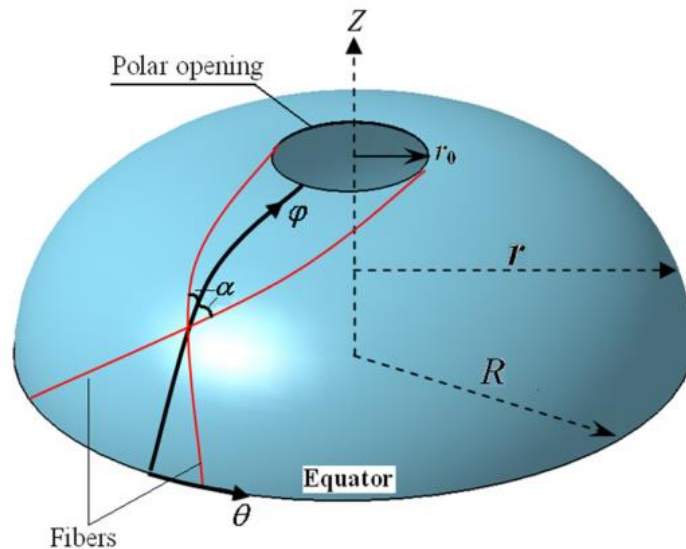


Figure 3-1 The winding angle on a general shell of revolution (Zu, 2012)

The winding trajectories are categorised in geodesic and non-geodesic. The geodesic trajectories are the trajectories, which connect two arbitrary points on a surface following the shortest route (Koussios, 2004). On the other hand, the non-geodesic trajectories deviate from this path, enlarging in that way the design space. It is obvious that the geodesic trajectories are a special case of winding trajectories and the non-geodesic a general one.

This can be concluded also by examining the equation, which calculates the winding angle at a location of the surface. According to Zu (2012), the winding angle is given by:

$$\frac{d\alpha}{dz} = \lambda \left[ \frac{\sin \alpha \tan \alpha}{r} - \frac{r''}{1 + r'^2} \cos \alpha \right] - \frac{r' \tan \alpha}{r} \quad \text{Eq. 3.1}$$

In this equation,  $\mathbf{r}$  and  $\mathbf{z}$  denote the radial and axial coordinate respectively and  $\lambda$  stands for the slippage coefficient, which will be explained later. It should be noted that  $\mathbf{r}$  is a function of  $\mathbf{z}$  and  $\mathbf{r}'$  and  $\mathbf{r}''$  are the first and second derivatives of  $\mathbf{r}$  respective to  $\mathbf{z}$ . In fact, the function  $\mathbf{r}$  is a parameterization of the shape of the geometry, which is examined.

The slippage coefficient  $\lambda$  is given by Zu (2012):

$$\lambda = \frac{k_g}{k_n} \quad \text{Eq. 3.2}$$

where  $\mathbf{k}_g$  is the geodesic curvature and  $\mathbf{k}_n$  is the normal curvature. The geodesic curvature is associated with the friction force applied to fiber bundle, which is tangential to the mandrel surface. Respectively, the normal curvature is associated with the normal force applied to the fiber bundle, which is perpendicular to the surface. For further explanation, please refer to Zu (2012), as the mathematical proof of the equation is beyond the scope of this thesis.

The slippage coefficient is a measurement of the tendency of the fiber bundle to slip over the supporting surface, either the supporting surface is the liner or the previous composite layer (Zu et al., 2010). In order to prevent fiber sliding, the friction force  $\mathbf{F}_f$  should be less than the maximum static friction between the fiber bundle and the supporting surface (Zu, 2012):

$$|F_f| \leq \mu_{max}|F_n| \quad \text{Eq. 3.3}$$

where  $\mu_{max}$  is the coefficient of the maximum static friction between the two surfaces (the supporting surface and the fiber bundle) and  $\mathbf{F}_n$  is the force normal to the surface applied to the fiber bundle. The normal force depends on the winding tension, whereas the coefficient of maximum static friction depends on the quality of the two surfaces and other parameters, which will be discussed thoroughly in section 3.1.2.

According to Zu (2012), the non-slippage criterion is defined as:

$$\left| \frac{k_g}{k_n} \right| \leq \mu_{max} \quad \text{Eq. 3.4}$$

and with the substitution of equation (3.2) into (3.4) yields:

$$|\lambda| \leq \mu_{max} \quad \text{Eq. 3.5}$$

Therefore, in order to prevent fiber sliding, the slippage coefficient of eq. (3.1) should never exceed the value of the coefficient of maximum static friction.

Having explained the meaning of the slippage coefficient, it should be added that the geodesic curvature of a geodesic trajectory is null, thus the slippage coefficient  $\lambda$  is also null (Zu, 2012). As a result, the equation, which gives the winding angle of a geodesic trajectory of a general shell of revolution at a particular location is:

$$r = \sin \alpha r_0 \quad \text{Eq. 3.6}$$

On the other hand, the winding angle of non-geodesic trajectories is given solely by equation (3.1) for  $\lambda \neq 0$ , which do not have an analytical solution. The winding angle is calculated step by step using the Runge-Kutta iterative method. In order to use this method, an initial condition is needed. The initial condition is the winding angle at the polar opening (for  $r=r_0$ ), which is 90deg in any case.

However, the slippage coefficient must also be defined in order for the Rung-Kutta method to be applied. As it was mentioned above, the slippage coefficient  $\lambda$  should always be less than the maximum static friction coefficient  $\mu_{max}$ , but its value cannot be taken as constant along the fiber path. Zu et al. (2010) state that in order to maintain the  $C^1$  continuity at the dome-cylinder conjunction of the roving path, the derivative of the winding angle must have the same value as the derivative of a geodesic path at the same location. As a result, at that place, the slippage coefficient must be equal to zero. To solve this problem, Zu et al. (2010) proposed the use of a distribution for the slippage coefficient for the calculations. The equation that they proposed is the following:

$$\lambda = \mu_{max} \cos\left(\frac{\pi}{2} \frac{r - r_0}{R - r_0}\right) \quad \text{Eq. 3.7}$$

Finally, with the use of the equations (3.1) and (3.7) for a specific geometry (shape,  $r_0$  and  $R$ ) and by defining the maximum static friction coefficient for the specific design, the designer can determine the maximum initial winding angle  $\alpha_{init}$  with which the fiber sliding is avoided. For a pressure vessel, the initial winding angle  $\alpha_{init}$  is also the winding angle at the cylindrical portion.







The reverse procedure can also be done. If the initial winding angle  $\alpha_{init}$  and the slippage coefficient are given, then the radius of the dome at which the fiber will turn around can be calculated. At this case, the turnaround radius is not necessarily the same as the geometrical  $r_0$  of the pressure vessel as the fiber will turn around earlier in order to avoid sliding. In this way, a proportion of the dome will only be covered by the fibers. Therefore, it is obvious that the  $r_0$  in equations (3.1) and (3.7) is in fact the radius of the dome at which the fiber turns around and it is equal to the radius of the polar boss opening only in the case at which the whole dome is covered.

It can be concluded that the three parameters (turnaround radius  $r_0$ , slippage coefficient  $\lambda$  and initial winding angle  $\alpha_{init}$ ) cannot be defined at the same time. The third parameter derives from the combination of any of the other two. However, in order to avoid fiber sliding the slippage coefficient must be defined and be equal to or lower than the maximum static friction coefficient, so one of the two defined parameters must be the slippage coefficient.

It should be noted that for the rest of the thesis only non-geodesic trajectories have been used.

### 3.1.2 Maximum static friction coefficient

The determination of the maximum static friction is important for both the design process and the manufacturing process. In the design process, it is needed in order to calculate the maximum winding angle with which the fibre sliding will be avoided. However, the value of the maximum static friction is depended on different manufacturing parameters and its value can only be calculated with experimental testing. Different experimental methods can be used, some of which are presented in Figure 3-2.

Mandrel shape measurement	Measurement
1. Bullet shape mandrel 	Winding with angle $\alpha \approx$ constant till the fiber tows slips
2. Coaxial cones mandrel 	Hoop winding, tangent of the cone angle gives the friction coefficient
3. Cylindrical shape mandrel 	Winding with angle $\alpha$ changed till the fiber tows slips
4. Trumpet shape mandrel 	Two different forces, increase on till fiber tows slips
5. Arbitrary shape mandrel 	Block with roving on the underside will slip at a certain inclination angle
6. Plane shape mandrel 	One fiber tow will slip at a certain inclination angle

**Figure 3-2 Several methods for maximum static friction coefficient method measurement (Wang et al., 2011)**

In order to define the parameters, which affect the value of the static friction coefficient, Koussios and Bergsma (2006) and Wang et al. (2011) used the first method showed in Figure 3-2. The roving is being wound over a bullet shaped mandrel with a constant angle until it slips. The mandrel shape is designed in such way that there is a linear proportion relation between either the position on the longitudinal axis of the mandrel (which is also the axis of the translation of the carriage of the machine) (Koussios and Bergsma, 2006) or the radius of the mandrel at each longitudinal position (Wang et al., 2011) and the slippage coefficient. In that way, the determination of the longitudinal position or the radius, respectively, at which the fibre sliding happens gives the value of the slippage coefficient over which slippage cannot be avoided, thus the maximum static friction coefficient. A schematic view of the experimental set up used by Koussios and Bergsma (2006) is presented in Figure 3-3. The winding angle, which was used, was approximately 90deg. However, in reality the winding angle is equal to:

$$a(r) = \tan^{-1} \left( \frac{2\pi r}{BW} \right) \quad \text{Eq. 3.8}$$

where  $r$  is the radius at each longitudinal position and  $BW$  is the width of the fiber bundle (bandwidth).

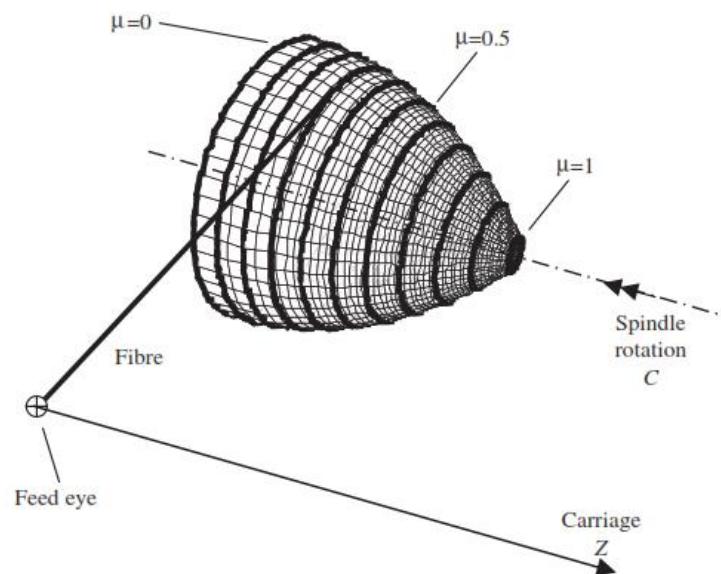


**Figure 3-3 Schematic view of the experimental layout. The bold lines represent a static friction coefficient increment equal to 0.1 (Koussios and Bergsma, 2006)**

Both research teams investigated the effect of winding speed, roving tension, fibre materials, bandwidth, winding method (wet or dry winding), and the type of the underlying surface in the value of the maximum static friction coefficient. Wang et al. (2011) also investigated the effect of the resin viscosity.

The results showed that the effect of the winding speed on the friction coefficient between the tow and the mandrel is negligible. Koussios and Bergsma (2006) used 3 different winding speeds (3.6, 12 and 60 RPM) and Wang et al. (2011) used 5 different speeds (7.2, 9.6, 12, 36 and 60 RPM), but the value of the coefficient did not change. Both teams agreed that the roving tension do not practically affect the value of the static friction coefficient.

As for the fibre materials, it is concluded that the type of the carbon fibre (T300, T700, T800 or T1000) do not affect the coefficient (Wang et al., 2011). However, the coefficient obtained by glass fibre is slightly different for Wang et al. (2011) (from 0.33 for glass fibres to 0.32 for glass fibres) and negligible for Koussios and Bergsma (2006) (in the order of 0.003). Koussios and Bergsma (2006) also add that there are references with experimental results significantly different for glass fibre and carbon fibre and this difference may be due to the treatment of the surface of the fibers or the mandrel.

The results of the experiments of both teams indicate that the bandwidth is a decisive factor for the value of the friction coefficient. The experiments of Koussios and Bergsma (2006) showed that an increase of the bandwidth from 0.3mm to 3mm increased the friction coefficient approximately 35% (from 0.14 to 0.2). Respectively, the results of Wang et al. (2011) showed that an increase of the bandwidth from 3mm to 12mm brought an increase in the value of the coefficient from 0.35 to approximately 0.38. It is noted that the values between the two experiments are different because the parameters used by Koussios and



Bergsma (2006) and Wang et al. (2011) are not common. However, the indication of the dependence of the coefficient on the bandwidth is present in both cases.

Both teams also investigated the importance of whether the winding is dry or wet. Koussios and Bergsma (2006) concluded that the friction coefficient for wet winding is approximately 3 times higher than the respective coefficient for dry fibers. However, the results of Wang et al. (2011) do not completely agree with Koussios and Bergsma (2006) findings. They agree that the friction coefficient for wet fibers is greater, but the increase is lower as their results showed that coefficient is 0.33 for dry winding and 0.35 for wet winding.

The investigation of the effect of the underlying surface is not common for the two studies. Koussios and Bergsma (2006) investigated three different qualities of mandrel surface. In the first case the aluminum surface was polished, in the second case was covered with a dry epoxy layer and in the last case it was covered with a roughened epoxy layer (achieved with the use of a sandpaper). As expected, the polished surface has lower friction coefficient compared to the surfaces covered with epoxy resin. Its value is approximately 3 times greater in the latter cases compared to the polished surface, but the difference between the two cases covered with epoxy is negligible. On the other hand, Wang et al. (2011) compared the friction coefficient obtained when the underlying surface is the mandrel and when the underlying surface is a composite layer. The results showed that in the latter case (where the underlying surface is the composite layer) the coefficient is decreased from 0.33 (which was when the underlying surface was the mandrel) to 0.24.

Finally, Wang et al. (2011) included in their study the importance of the resin viscosity. Their analysis showed that as the viscosity of the resin decreased, the value of the static friction coefficient was also decreased.

Koussios and Bergsma (2006), in the end of their study, propose certain values of the friction coefficient, which could be taken into account in the design process. If the surface of the aluminium mandrel is polished, the coefficient should be considered to be 0.15 for dry fibers and 0.4 for impregnated (wet) fibers. In addition, for dry fibers wound on a smooth surface covered with epoxy, the friction coefficient is 0.5. Finally, the friction coefficient is equal to 0.6, when the underlying surface is covered with a roughened layer of epoxy resin.

Respectively, Wang et al. (2011) present their measurements of the static friction coefficient for certain manufacturing parameters. The winding speed was chosen to be 12 rpm, the fiber bandwidth was 3mm, the roving tension was 5N and the resin viscosity was 151.24 mPa s. The measurements were taken for dry and wet carbon fibers on a 2A12 aluminium alloy mandrel and on a composite layer. The measured values are summarized in Table 3-1.

**Table 3-1 Measured values of static friction coefficient from experiments of Wang et al. (2011)**

Underlying Surface	Fiber bundle	Static friction coefficient
Mandrel	Dry	0.33
Mandrel	Wet	0.35
Composite	Wet	0.24

### 3.1.3 The winding equation used in Wound Composite Modeller of Abaqus

The FEM analysis in the framework of this thesis will be done in Abaqus. Abaqus includes a toolkit developed for modelling of composite pressure vessels called “Wound Composite Modeller.” This toolkit, though, uses a different equation from this described in section 3.1.1 to simulate the winding path. The equation used is the following (Simulia, 2016):

$$\alpha(r) = \sin^{-1} \left( \frac{r_0}{r} \right) + \delta \left( \frac{r - r_0}{R - r_0} \right) \quad \text{Eq. 3.9}$$

It is noted that the equation is similar to equation (3.6), which describes the geodesic trajectories, with an adding term. The second term of the equation is used to simulate non-geodesic trajectories. If the user decides to use geodesic trajectories, then the algorithm equals  $\delta$  to zero and the equation (3.9) describes the geodesic trajectories precisely. On the other hand, in the case of non-geodesic trajectories, the variable  $\delta$  is different from zero.

Another notable fact is that the equation do not include the slippage coefficient, which is needed in non-geodesic trajectories. This happens because the software permits the user to define both the initial winding angle  $\alpha_{\text{init}}$  and the turnaround radius  $r_0$ . In this way, it is up to the knowledge of the user to define a proper pair of these two parameters in order to avoid fiber sliding.

The way, in which the fiber bundle path is defined, is a bit more complex. The software, basically, uses the linear interpolation of two different geodesic trajectories in order to create a non-geodesic trajectory. The first geodesic curve is derived using as a parameter only the initial winding angle  $\alpha_{\text{init}}$ , which is defined by the user. Obviously, the turnaround radius of this curve is not, in general, the turnaround radius, which was asked by the user. For that reason, the second geodesic curve is based on an initial winding angle  $\alpha_{\text{init}}$ , which would reproduce the turnaround radius given (Simulia, 2016). Then, the software calculates the difference between the two initial winding angles. This calculated value is used as the variable  $\delta$  of the equation (3.9) for the linear interpolation.

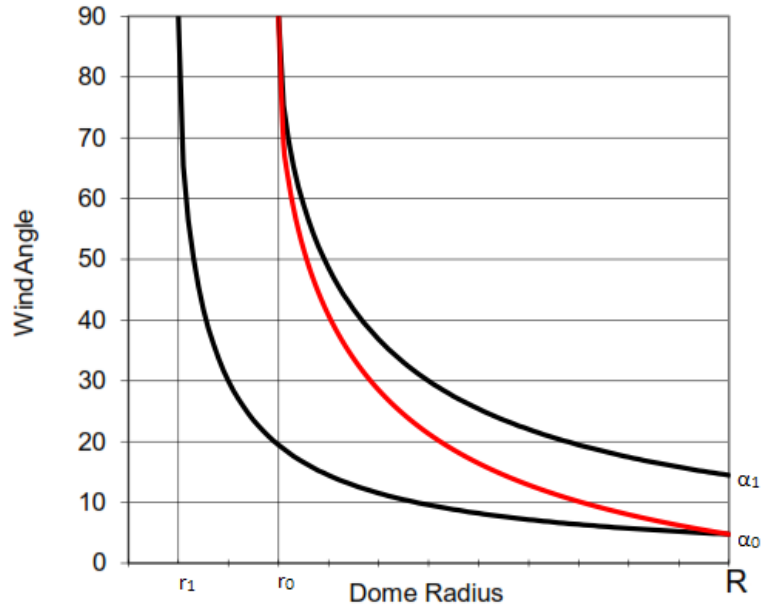


**Figure 3-4** The two geodesic curves (in black) and the derived non-geodesic curve (in red). The given values of winding angle and turnaround radius are denoted with the number 0 (Simulia, 2016)

### 3.1.4 Winding angle diagrams

From the previous sections is obvious that equations (3.1) and (3.9) did not produce exactly the same results. For this reason, a comparison between these two equations is necessary. It is also necessary to investigate how much the slippage coefficient affects the winding angle distribution along the dome derived by equation (3.1).

The aforementioned investigation must be based on a certain geometry in order to be feasible, as for different geometry, the winding angle distribution changes. The investigation that was carried out was based on spherical and ellipsoidal domes. The parametric equation that describes both geometries is common and is the following:

$$r(z) = R \sqrt{1 - \frac{z^2}{c^2}} \quad \text{Eq. 3.9}$$

$$\text{for } 0 \leq z \leq c \sqrt{1 - \frac{r_0^2}{R^2}}$$

$$\text{and } r_0 \leq r(z) \leq R$$

where  $c$  is the length of the minor axis. If  $c=R$  then the described geometry is a sphere. If  $c$  is different from  $R$ , then eq. (3-9) describes an ellipsoid. The  $z$  is the coordinate on a longitudinal axis of the dome, starting at the dome-cylinder conjunction and directed to polar boss opening. The parameters are shown in Figure 3-1.

In order to solve the differential equation (3.1) (along with the use of equations (3.7) and (3.9)) an algorithm in the Matlab software was created. The algorithm uses the 4<sup>th</sup> order Runge-Kutta method to solve numerically the differential equation. The algorithm is presented in Appendix A.

Firstly, for three spherical domes with different radii the effect of the maximum friction coefficient and the radius of the polar boss opening were investigated. The first dome has a radius equal to 150mm, the second equal to 200mm, and the last equal to 250mm. In addition, for each dome, three different winding angle distributions with different radius of polar boss opening (12.5mm, 25mm, and 50mm) and for a maximum static friction coefficient equal to 0.2 were created. Then, these three curves were recalculated and three new curves for a maximum static friction coefficient equal to 0.5 were created. All these six curves for each dome are shown in Figure 3-5, Figure 3-6 and Figure 3-7 respectively.

It should be noted that the three figures show the winding angle distribution along the dome for full coverage of the dome with composite reinforcement. Additionally, as equation (3.1) has been solved for defined polar boss openings and maximum static friction coefficients, the winding angle at the dome-cylinder conjunction of each curve shown in the figure below, is the max possible winding angle which can be used at the cylindrical portion without having fibre sliding at the dome region.

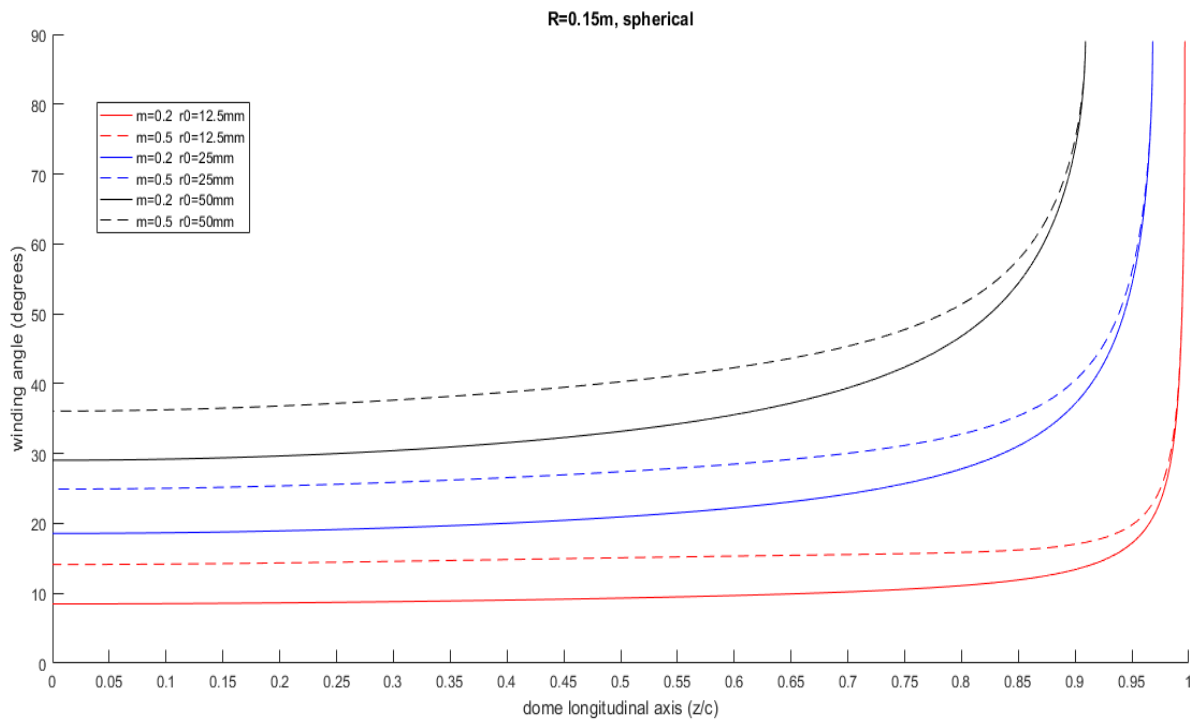


**Figure 3-5 Winding angle distributions along a spherical dome with a radius of 150mm with respect to the dome longitudinal axis. The curves are plotted for different static friction coefficient (m in the legend) and radius of polar boss opening (r0 in the legend)**

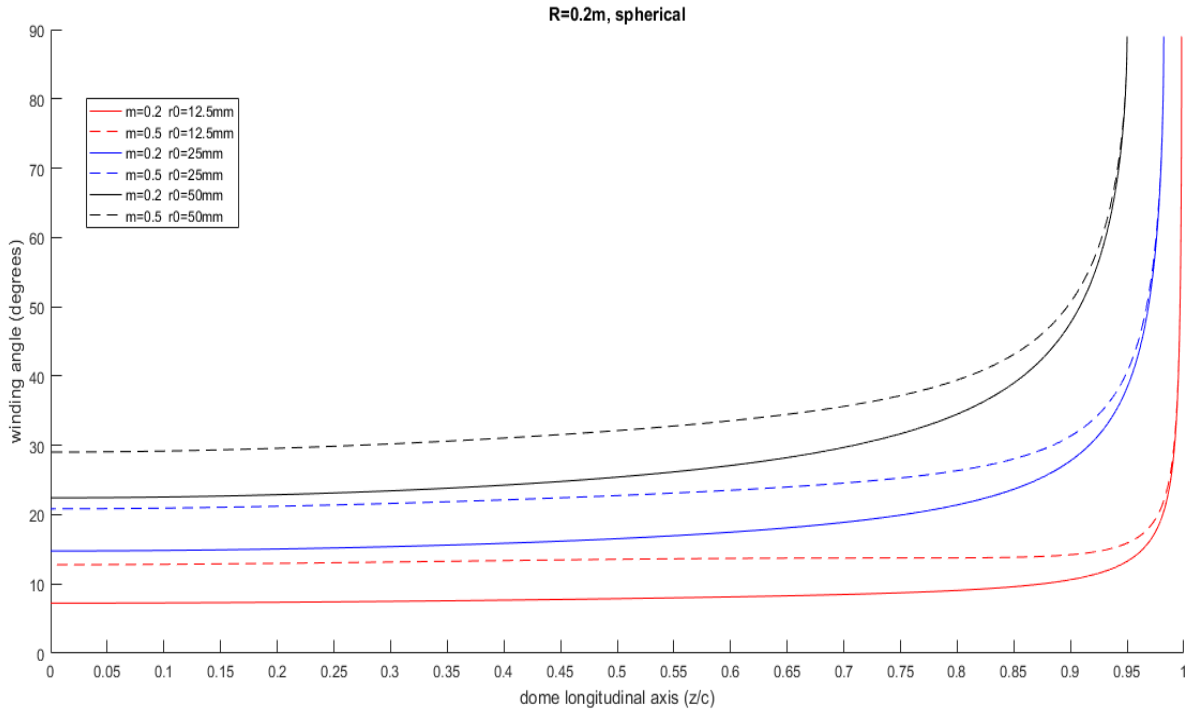


**Figure 3-6** Winding angle distributions along a spherical dome with a radius of 200mm with respect to the dome longitudinal axis. The curves are plotted for different static friction coefficient ( $m$  in the legend) and radius of polar boss opening ( $r_0$  in the legend)

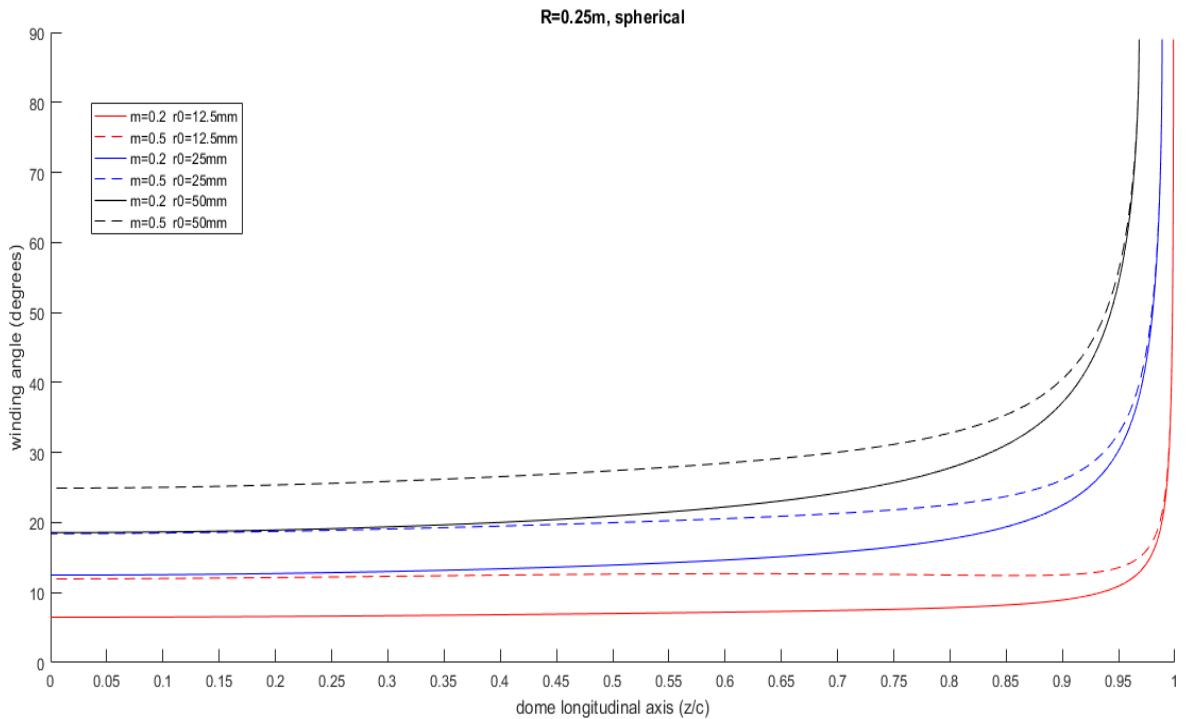


**Figure 3-7** Winding angle distributions along a spherical dome with a radius of 250mm with respect to the dome longitudinal axis. The curves are plotted for different static friction coefficient ( $m$  in the legend) and radius of polar boss opening ( $r_0$  in the legend)

From these three figures, it can be concluded that the radius of the polar boss opening affects significantly the maximum possible winding angle for the same static friction coefficient. It is also shown that the increase of the maximum static friction coefficient

resulted in a slight increase of the maximum possible winding angle (approximately 6deg). In addition, it is notable that the increase of the winding angle along the dome, in any case, is considerably steep and the winding angle remains almost equal to the initial winding angle in a big part of the dome. However, this phenomenon is becoming more significant with the increase of the radius of the dome, as the increase of the winding angle is more gradual for the dome with the smallest radius. Finally, it can be concluded that the increase of the radius of the domes resulted in a slight decrease of the maximum possible winding angle at the dome-cylinder conjunction.

Another comparison was made between a spherical dome (the one showed in Figure 3-6) and an ellipsoidal dome with the same radius and a minor to major axis ratio of 0.7. The ratio was chosen based on relative literature and usual engineering practice (Katsounis and Tsouvalis, 2014). The derived winding angle distribution is showed in Figure 3-8.

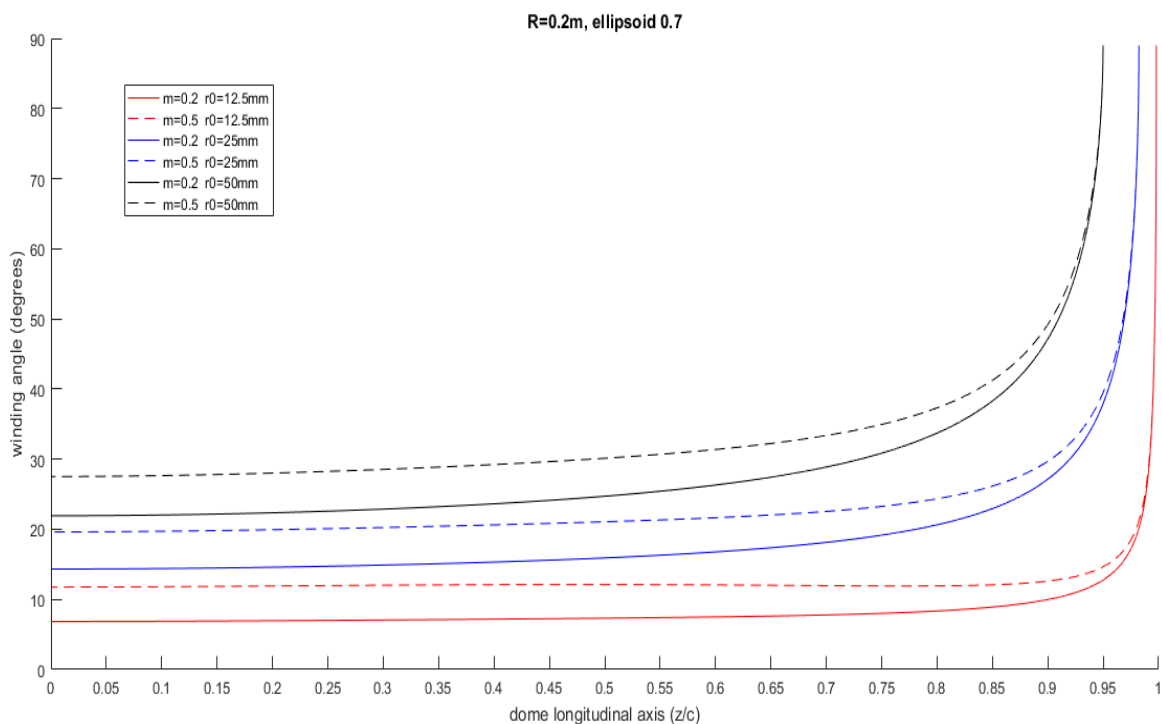


**Figure 3-8 Winding angle distributions along an ellipsoidal dome (ratio of minor to major axis equal to 0.7) with a radius of 200mm with respect to the dome longitudinal axis. The curves are plotted for different static friction coefficient (m in the legend) and radius of polar boss opening (r0 in the legend)**

From the comparison of Figure 3-6 and Figure 3-8, it can be concluded that the difference is insignificant. In fact, there is a slight decrease of the maximum possible winding angle (approximately 0.5deg). However, the general shape of the distribution remains the same.

In sum, it can be concluded that the radius of the polar opening and the maximum static friction coefficient affect the distribution and the maximum possible winding angle significantly. As the values of both parameters increase, the maximum possible winding angle also increases. On the other hand, the radius of the dome and the shape do not affect considerably either the distribution or the maximum initial winding angle.

However, in the FEM analysis that will follow, equation (3.9) will be used instead of the equation (3.1), which was investigated and it describes the fibre paths accurately. For this reason, a comparison of the results of the two equations is needed.

The comparison of the two equations must be based on the same parameters in order to be accurate. For this reason, equation (3.9) was implemented for the same turnaround radius. In addition, the initial winding angle is also needed for the implementation of equation (3.9). Therefore, the value of the maximum possible winding angle which had been previously calculated with equation (3.1) was used for the implementation of equation (3.9).

The two equations were compared on two different geometries. The first geometry was a spherical dome and the second geometry was an ellipsoid dome with a minor to major axis ratio equal to 0.7. Both domes had an equator with a radius equal to 0.2m (200mm). For each different geometry, three different radius of polar opening were examined (12.5mm, 25mm and 50mm). The results of the analysis for the spherical dome are shown in Figure 3-9 and for the ellipsoidal dome in Figure 3-10.

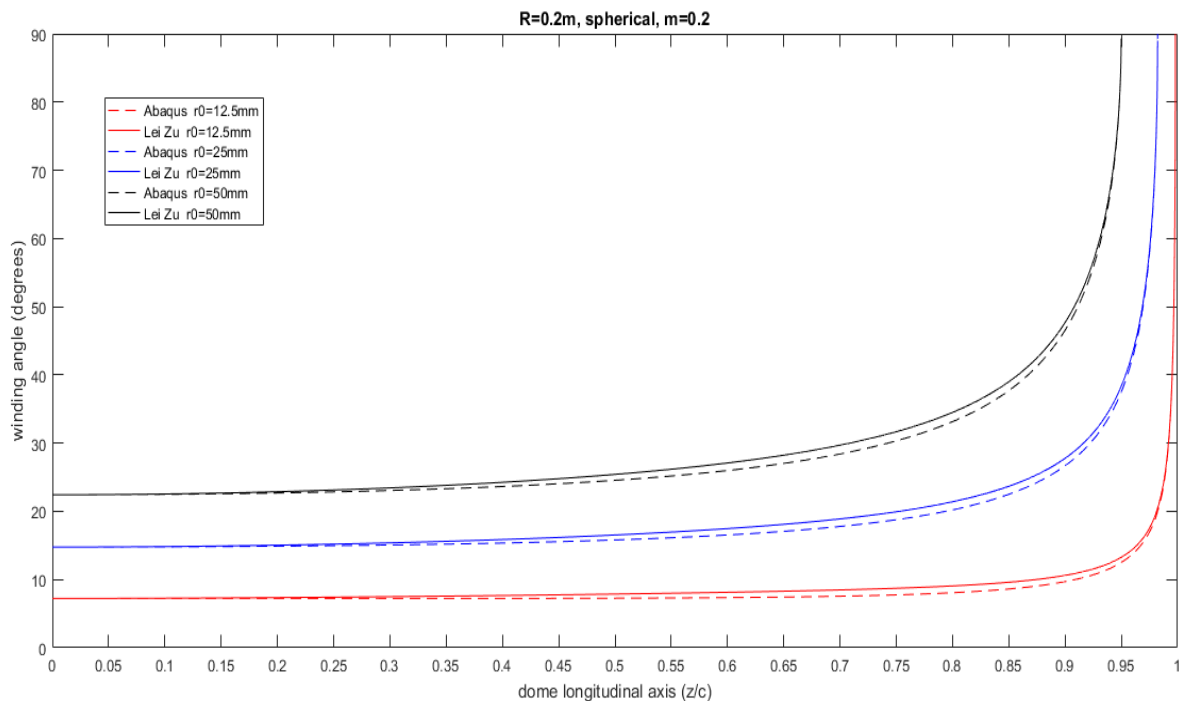


**Figure 3-9** Winding angle distributions along a spherical dome with a radius of 200mm respect to the dome longitudinal axis. The winding angle distribution has been calculated for different radius of polar boss openings (different colours) with the equation proposed by Zu (2012) (continuous lines) and the equation used by Abaqus (Simulia, 2016) (dashed lines).

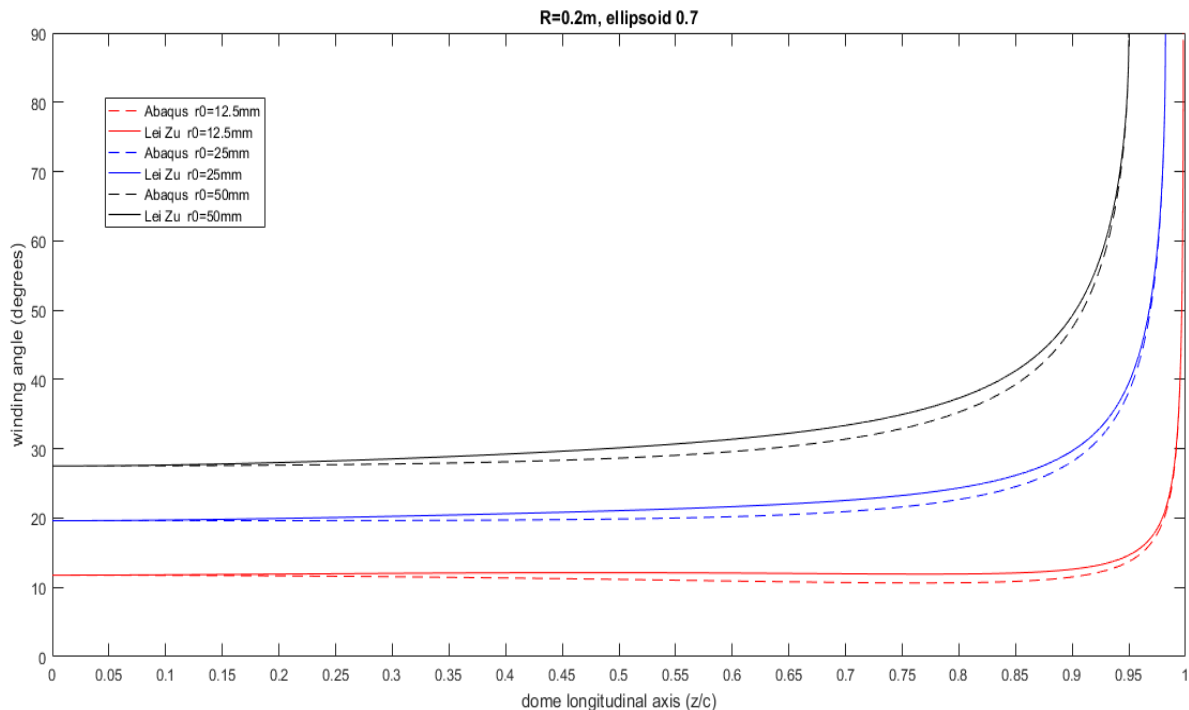


**Figure 3-10 Winding angle distributions along an ellipsoidal dome (ratio of minor to major axis equal to 0.7) with a radius of 200mm respect to the dome longitudinal axis. The winding angle distribution has been calculated for different radius of polar boss openings (different colours) with the equation proposed by Zu (2012) (continuous lines) and the equation used by Abaqus (Simulia, 2016) (dashed lines).**

The two figures show that the difference in the calculated values of the winding angle by the two different equations for both geometries is negligible. In fact, the difference does not exceed 2deg in any location of the path. In addition, it can be noted that the winding angles produced by the equation used by Abaqus are, in any case, smaller than those of the equation of Zu (2012). Thus, the equation of Abaqus can be used for the simulation, as it represents the actual path with great accuracy, without the possibility of fibre sliding

## 3.2 Thickness variation along the dome

### 3.2.1 Theoretical equations and comparison

The thickness of the composite laminate at the cylindrical portion of the pressure vessel is constant at its entire length. However, the same does not happen at the dome areas. The thickness at the equator of the dome is equal to the thickness at the cylindrical portion, but it is growing proceeding to the polar boss area. The rovings are wound the one adjacent to the other at the equator, but the same number of roving are distributed in a smaller periphery at the polar area, resulting in overlapping of the fiber bundles and growth of the thickness (Koussios, 2011). At the same time, the winding angle increases, thus the fibers are wound in a more parallel way, resulting in more overlapping and a more rapid growth of thickness (Koussios, 2011).

Koussios (2011) is proposing various equations, which simulate the thickness build-up along the dome, but they are only fitted in integral optimized geodesic domes, so they are omitted in this thesis.



According to Park et al. (2002), the thickness build up can be simulated with the following equation:

$$t(z) = \frac{R \cos \alpha_{init}}{r(z) \cos \alpha(z)} t_c \quad \text{Eq. 3.10}$$

where  $t_c$  is the composite thickness at the equator. The equation can be implemented under two assumptions. The assumptions demand that the fiber volume fraction is maintained consistent and the number of fibers in any cross-section is always the same (Park et al., 2002).

Examining equation (3.10), it can be concluded that the thickness build-up is not depended on the initial thickness at the equator, as the build-up is described only by the fraction term of the equation. The initial thickness affects only the final value of the thickness and not how much the thickness will increase. Furthermore, the winding angle at the polar area becomes 90deg, thus the equation (3.10) becomes infinity. However, Park et al. (2002) state that ,in reality, thickness convergence is achieved. For that reason, the thickness can be corrected and assumed as constant from 98% to 100% of the meridian length measured from the dome-cylinder intersection (Park et al., 2002). A similar assumption is also proposed by Koussios (2011). He proposes that the thickness can be simulated as constant for a length equal to the fiber bundle bandwidth, measured from the polar boss opening towards the dome-cylinder conjunction. The latter assumption is used in the framework of this thesis.

The Wound Composite Modeler of Abaqus also uses a similar equation for the thickness build-up along the dome. The equation that is being used is (Simulia, 2016):

$$t(z) = \frac{t_c \cos \alpha_{init}}{\cos \alpha(z)} \frac{R}{r(z) + 2BW \left( \frac{R - r(z)}{R - r_0} \right)^4} \quad \text{Eq. 3.11}$$

where BW is the width of the fiber bundle (bandwidth). Comparing equations (3.10) and (3.11) it can be concluded that the only difference is an added correction factor in equation (3.11). This correction factor is only depended on the bandwidth. Abaqus allows the user to choose the location where the thickness build-up stops. In this thesis the location is chosen according to the aforementioned proposal of Koussios (2011).

Equations (3.10) and (3.11) were compared for different bandwidths (20, 30 and 40mm) and different radii of polar boss opening (12.5, 25 and 50mm) for a spherical dome with a radius of 200mm. The thickness derived by this analysis is shown in Figure 3-11. The results are plotted for a value of the longitudinal coordinate to minor axis ratio greater than 0.6, as up to that point the thickness build up is small. The thickness is plotted dimensionless with value 1 being the initial thickness.

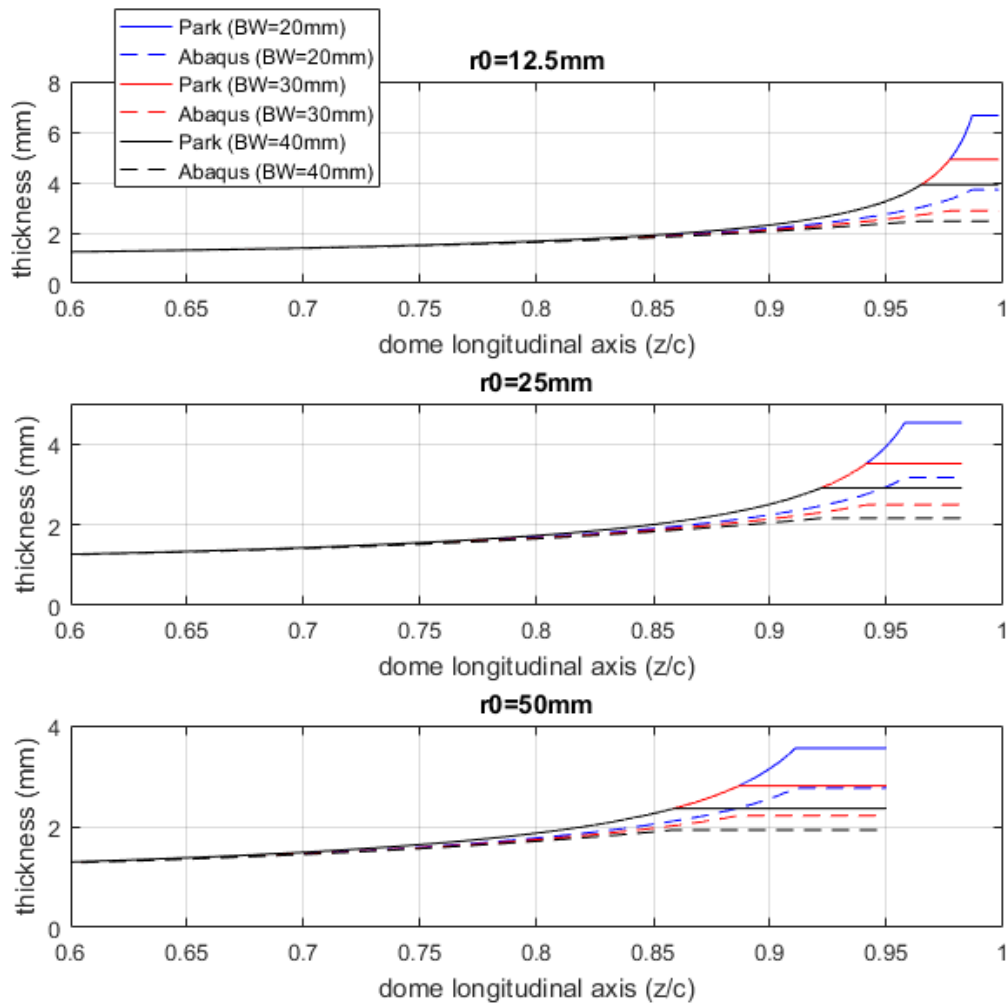


**Figure 3-11** The thickness build-up along a spherical dome with a radius equal to 200m.

From Figure 3-11, it can be concluded that equation (3.11), in any case, produces lower thickness than equation (3.10). Therefore, the FEM analysis in Abaqus underestimates the strength of the dome region, as the thickness is lower (approximately 40% at the polar opening region). In that way, there is an extra safety factor in the simulation. Furthermore, it can be noticed that the decrease of the bandwidth increases the developed thickness. This happens, because the fiber bundles are concentrated in a smaller area and there is more overlapping.

This analysis is not required to be repeated for different radius of equator, as it has been done in section 3.1.4, because it is obvious that the increase of the radius will result in an increase of the developed thickness. This is explained by the fact that for the same bandwidths, more fiber bundles are needed to cover the periphery in the equator. Therefore proceeding to the polar area (smaller periphery) the increased number of rovings produces greater thickness as the overlapping is more significant.

On the other hand, the same analysis can be repeated for a different geometry. The selected geometry that was examined is an ellipsoidal dome with a minor to major axis ratio equal to 0.7 and a radius of equator equal to 200mm. The results are shown in Figure 3-12.

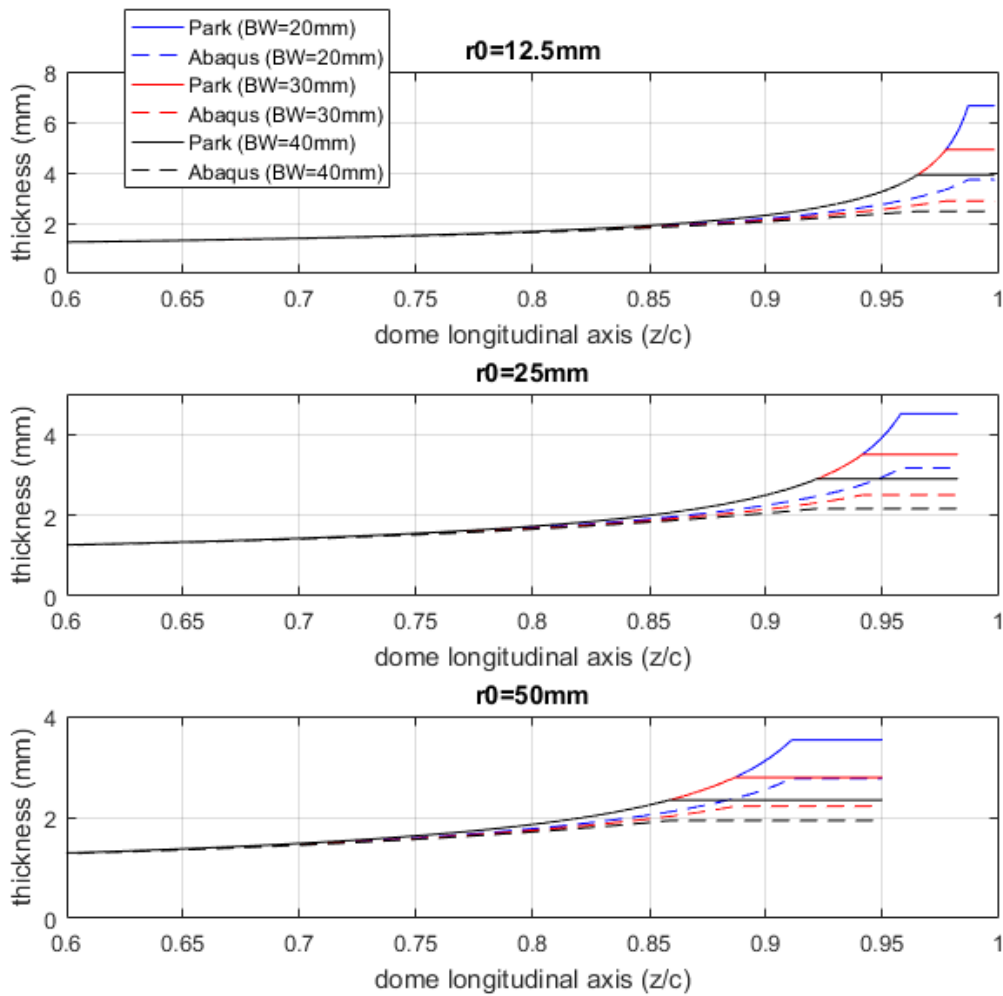


**Figure 3-12 The thickness build-up along an ellipsoidal dome (ratio of minor to major axis equal to 0.7) with a radius equal to 200m.**

From the two figures, it can be concluded that the effect of the dome shape in the thickness build up is negligible. There is a slight decrease of the thickness with the use of the ellipsoidal dome, but the difference is in the order of 0.02mm. The same conclusion can be derived for the results obtained from both the equations that were compared.

### 3.2.2 Experimental results

An attempt to measure the thickness build-up in reality was carried out in the Shipbuilding Technology Laboratory in the context of this thesis. The pressure vessel, which was used for this purpose, had been designed and manufactured in the context of a previous research project (Katsaounis and Tsouvalis, 2014).

The nominal internal radius of the cylindrical portion was 145mm and its length was equal to 1000mm. The two ellipsoidal domes had a minor axis equal to 100mm. The pressure vessel also had two cylindrical extensions at the polar boss opening with a length equal to 32mm and internal diameter equal to 25.4mm (Katsaounis and Tsouvalis, 2014).

The thickness of the aluminium liner was designed to be 6mm at the cylindrical part and 12mm at the domes. The aluminium liner was wound with carbon reinforcement. The reinforcement consisted of a helically wound reinforcement with a total thickness of 9mm, which covered the entire surface of the pressure vessel (cylindrical portion and domes), and a hoop wound reinforcement with a total thickness of 13.5mm, which covered only the cylindrical portion and it was wound after the helical reinforcement. The helical reinforcement was wound with a winding angle equal to 10deg (Katsaounis and Tsouvalis, 2014). A design drawing of the pressure vessel is presented in Figure 3-13.

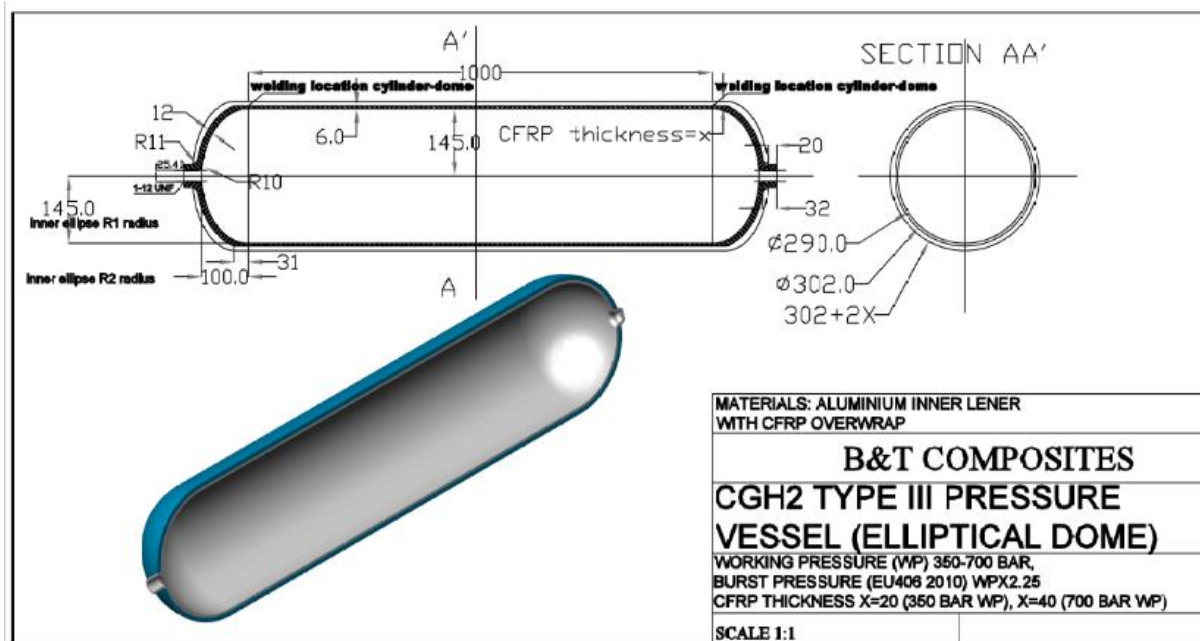
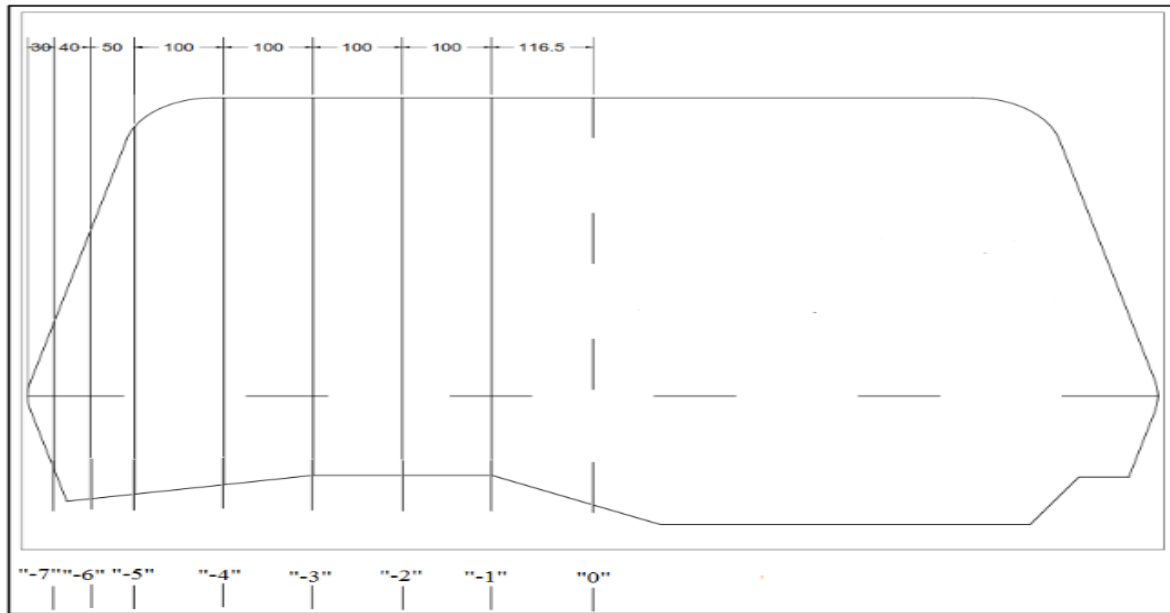


Figure 3-13 Design drawing of the examined pressure vessel (Katsaounis and Tsouvalis, 2014)

In the context of the aforementioned previous research project, the pressure vessel had been divided in areas. It had been divided in 12 areas in the circumferential direction (each at every 30deg) and in 14 areas in the longitudinal direction (7 at each symmetrical side of the tank). The division in the longitudinal direction is shown in Figure 3-14. This segmentation was also used for the purposes of this thesis.



**Figure 3-14** The longitudinal division of the pressure vessel (Sarafoglou and Tsouvalis, 2015)

The initial thought was to measure the thickness of the CFRP by drilling it with a hole saw and measuring the thickness of the extracted specimen. Unfortunately, this method could only be used in the cylindrical portion, as the increased thickness and the curved surface of the domes made unfeasible the drilling of the domes with that method.

The hole saw, which was used at the cylindrical portion, had a diameter equal to 34mm and it was able to cut both the CFRP and the aluminium liner. During the cutting, fresh water was being poured on the cutting surface in order to cool the hole saw and to diminish the produced dust. The aluminium was proved to be very destructive for the blades of the hole saw. For that reason, only one specimen of the aluminium was obtained. This specimen was taken in order to verify the position of the starting point of the dome.



**Figure 3-15** Various holes made with a hole saw in order to measure the thickness of CFRP at the cylindrical portion of the pressure vessel. At the left of the picture, the hole, where the starting point of the dome was verified, can be distinguished. The white lines shown divide the pressure vessel in different location areas.

At every hole, two measurements were taken at symmetrical positions. The measurements are summarized in Table 3-2. The average value of the cylindrical part thickness measurements is 23.11mm and the standard deviation 0.18mm. The measured values are close to the nominal thickness, which was 22.5mm.

**Table 3-2** Measurements of thickness of CFRP at the cylindrical portion

Location		Distance of measurement from the middle of tank (mm)	thickness (mm)
Longitudinal Area	Circumferential Area (deg)		
0	330	-16	22.9
		16	22.98
4-5	60	479	23.02
		514	23
1	30-60	101	23.41
		137	23.29
2	30	208	23.28
		242	23.02

It should be noted that the helical and the hoop windings were distinguishable by examining the cross section of the cut pieces. As it shown in Figure 3-16, the helical layers are darker than the hoop windings.



**Figure 3-16** Photo of a specimen of CFRP from the cylindrical portion of the pressure vessel

Before taking measurements at the dome areas, the starting position of the dome must be defined in order to have an accurate longitudinal coordinate. This was made by cutting the liner at a position close to the 5<sup>th</sup> line at 60deg (shown in Figure 3-15). From the specimen that was taken, the exact position of the welding of the dome at the cylinder was defined. The joint of the two surfaces was visible with naked eye as the two surfaces have different thicknesses, so a step at the joint was existed. The step was visible only in the internal surface of the liner and it is shown in Figure 3-17 and Figure 3-18.



**Figure 3-17** The external surface of the specimen cut from the aluminium liner at the dome-cylinder joint. The line in the middle is where the joint is. The surface at the right (roughened surface) is at the dome region, whereas the left surface (polished) is at the cylindrical portion





**Figure 3-18** The internal surface of the specimen cut from the aluminium liner at the dome-cylinder joint. The line in the middle is where the joint is. The dark surface is at the dome region and the lighter surface at the cylindrical portion.

The dome-cylinder conjunction was measured to be at a distance of 495mm from the middle of the cylinder, which coincides with the design, as the total length of the cylinder is 100cm.

Due to the increased thickness and the curved surface of the CFRP at the dome region, the hole saw could not be used. It was only used once at a location close to dome-cylinder conjunction, where the thickness was small. For the rest of the dome, a drill with a diameter equal to 16mm was used. The drilling was attempted to be as perpendicular to the surface of the liner as possible. The required angle to achieve this had been calculated analytically according to the shape of the dome.

Two thickness measurements were taken in every hole and their average was used in order to have more accurate results. Their longitudinal position from the starting position of the dome was also measured. Because the distance, which could be measured, was at the external surface of the composite, whereas the desired position is according to the internal surface of the composite, the angle at which the measurement was taken was also measured. In that way, using trigonometric equations, the exact longitudinal coordinate of the measurement of thickness was calculated. The five holes, which were made at the dome region are shown in Figure 3-19.

It should be noted that the two measurements from the two holes, which were made with a hole saw, were not averaged, as the measuring was done on the cut specimen. In addition, an extra measurement at the polar boss area was taken by measuring the thickness at polar boss region externally. The thickness at that location was measured at four symmetrical locations circumferentially and, then, the value was averaged. The average value was 23.68mm and the standard deviation was 0.44mm. The measurements of thickness at the dome and their location before the averaging are shown in Table 3-3 and after the averaging in Table 3-4.





**Figure 3-19** The five holes, which were made at the dome region. The first was made with a hole saw, whereas the rest of them with a drill.

**Table 3-3** The thickness measurements from the dome before averaging

Location		Longitudinal coordinate (mm)	thickness (mm)
Longitudinal Area	Circumferential Area		
4-5	60	0	9.11
		12.1	9.12
5-6	60	51.3	9.47
		69.6	11.49
7	30	86.1	25.95
		90.5	31.88
7	60	88.2	29.47
		97.7	32
6-7	90	80.4	17.08
		89.0	21.18
6-7	120	84.6	24.57
		92.4	30.03
Polar Boss Opening	30	105.3	23.75
	120	105.3	24.1
	210	105.3	23.05
	300	105.3	23.8

**Table 3-4 The averaged measured thickness at various locations at the dome. The results are sorted in ascending order of the longitudinal coordinate**

Longitudinal coordinate (mm)	thickness (mm)
0	9.11
12.1	9.12
51.3	9.47
69.6	11.49
84.7	19.13
88.3	28.92
88.5	27.30
92.9	30.74
105.3	55.68

The results were plotted in the same diagram with the theoretical curves of thickness build up proposed by Park et al. (2002) and used by Abaqus (Simulia, 2016), which were described in section 3.2.1. The two equations were implemented for the particular geometry and for a bandwidth equal to 20mm, as this value was used for the manufacturing of the pressure vessel. The curves and the experimental measurements are shown in Figure 3-20.

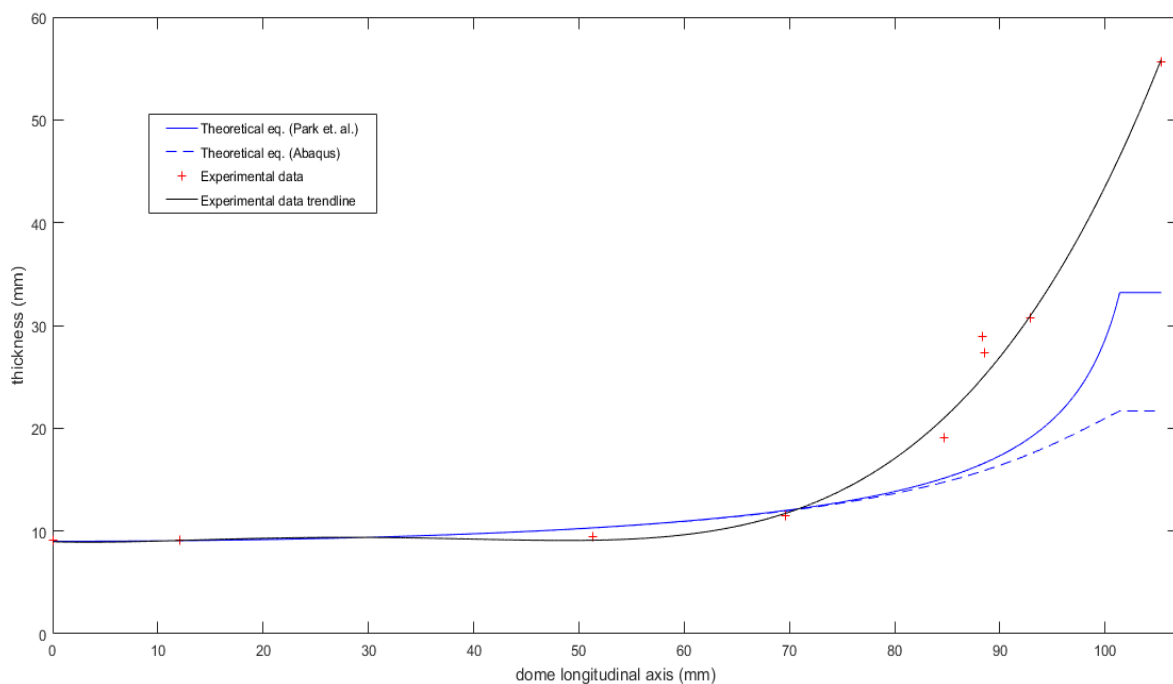


**Figure 3-20 The experimental measurements of thickness at the dome region, alongside the theoretical values of the thickness derived by eq. (3-10) (Park et al., 2002) and eq. (3-11) (Simulia, 2016). The examined geometry is an ellipsoidal dome with minor to major axis ratio equal to 0.7 and radius equal to 145mm. The used bandwidth is equal to 20mm.**

In Figure 3-20, it can be noticed that the measured thickness at the dome region is greater than the analytically calculated with equations (3-10) and (3-11). This difference may be partly due to the accuracy of the way that the thickness was measured, as a measurement error could not be avoided. On the other hand, the general distribution of the thickness build

up can be verified, as there is the characteristic steep increase of the thickness near the polar boss region. However, a more precise method of measurement and more points of thickness measurement could produce results that are more concrete.

## Chapter 4 Numerical Simulation

### 4.1 Description of the reference model

For the implementation of the theory of filament winding that was mentioned in Chapter 3, a model was created with the utilization of Finite Element Analysis. The final model was created in Abaqus software, but a formerly created model in ANSYS by Katsaounis and Tsouvalis (2014) was used as a reference model.

The aforementioned reference model is a pressure vessel consisting of a cylindrical portion, which has a length of 1000mm and an internal diameter equal to 290mm, and two spherical domes. There is also a polar boss opening at the top of each dome, which has 25.7mm internal diameter. In each opening there is a cylindrical extension at the edge of which there is a closing cap. The geometry of the pressure vessel is shown in Figure 4-1.

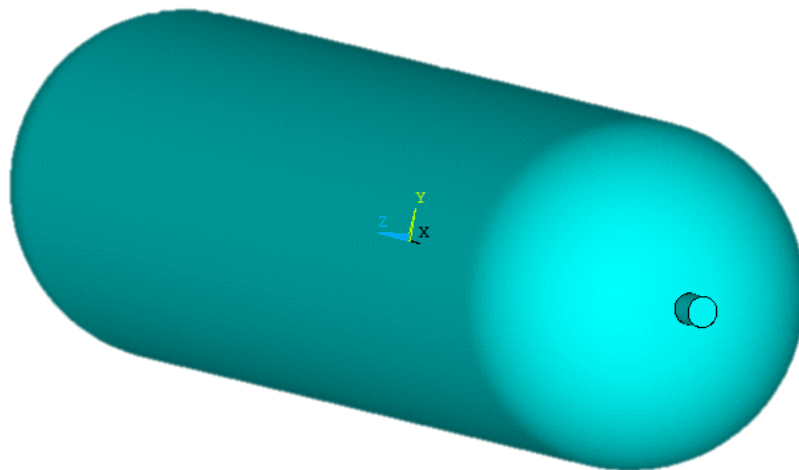


**Figure 4-1 Geometry of the model created in ANSYS by Katsaounis and Tsouvalis (2014). The spherical dome and the cylindrical extension at the polar boss are also depicted.**

The pressure vessel consists of an aluminum liner and carbon fiber reinforcement. The aluminum liner has a thickness of 6mm at the cylindrical portion and 12mm at the domes. The composite reinforcement consists of 4 helical layers and 6 hoop layers. The thickness of each layer is 2.25mm, creating a composite reinforcement with a thickness of 22.5mm. The material properties of aluminum alloy are summarized in Table 4-1 and those of the composite material in Table 4-2. The winding angle of the helical layers in the cylindrical portion is 10deg. The stacking sequence of the cylindrical part is shown in Figure 4-2 where material 1 corresponds to aluminium and material 2 corresponds to CFRP.

The material properties of the aluminum alloy and the composite material are obtained by literature and are summarized in Table 4-1 and Table 4-2.

**Table 4-1 Material properties of aluminum alloy (MPa) (Katsaounis and Tsouvalis, 2014)**

E	68900	Elastic modulus
E <sub>T</sub>	1378	Tangent modulus, equal to 2% of E
ν	0.33	Poisson ratio
σ <sub>y</sub>	276	Yield stress
σ <sub>u</sub>	310	Ultimate stress

**Table 4-2 Material properties of composite material (MPa) (Katsaounis and Tsouvalis, 2014)**

E <sub>1</sub>	132500	from tests
E <sub>2</sub>	8120	from tests
E <sub>3</sub>	8120	equal to E <sub>2</sub> (assumption)
G <sub>12</sub>	7120	from tests
G <sub>23</sub>	3560	equal to 0.5G <sub>12</sub> (assumption)
G <sub>13</sub>	7120	equal to G <sub>12</sub> (assumption)
ν <sub>12</sub>	0.280	(literature)
ν <sub>23</sub>	0.382	(literature)
ν <sub>13</sub>	0.280	equal to ν <sub>12</sub> (assumption)

The element SHELL281 of ANSYS, which is an 8-node layered shell element, was chosen for the modelling, as the diameter-to-thickness ratio is 10.16 at the cylindrical portion and 19.33 at domes, allowing the modelling of the pressure vessel as thinned wall. The first layer of the element represents the liner and the following layers the composite material. The helical layers cover the entire surface of the vessel, whereas the hoop layers cover only the cylindrical portion. The helical layers are modelled as an angle-ply (alternating positively and negatively orientated layers). The total number of layers that are used is 11. The first layer represents the aluminum liner, the next 4 are used for the helical layers (2 positively orientated and 2 negatively) and the last 6 external layers are used for the hoop layers.

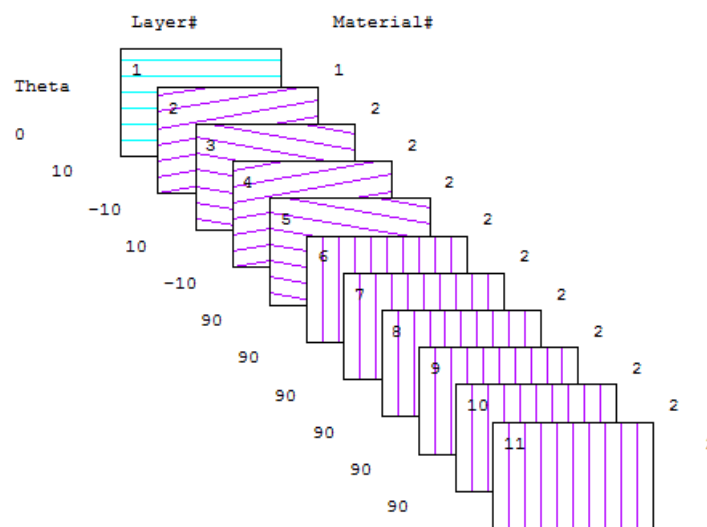


**Figure 4-2 A representation of the stacking sequence. The first layer represents the aluminium liner and the rest layers represent the composite reinforcement.**

The coordinates of the nodes and the construction of the mesh are generated by a software created for that purpose by Katsaounis and Tsouvalis (2014). The user specifies the number of elements to be used in each direction (longitudinal and circumferential) and then the software outputs a text file which can be imported in ANSYS in order to mesh the geometry of the model. The mesh is categorized in sections based on the orientation of the fiber in the region. In that way, the change of the winding angle along the dome can be discretized. As a result, the elements of the cylindrical portion are in the same section, as all of them have the same material properties (constant winding angle), whereas the domes are segmented in rings, which each ring belongs to a different section with different winding angle. The number of the rings in which each dome is segmented is chosen from the user. The aforementioned categorization of elements is shown in Figure 4-3.

The way in which the winding angle changes along the dome is specified by the user. The equation (3.9) was used for this purpose, so as to be comparable with the model that would be created in Abaqus environment. However, the modelling was created without the ability to include the development of the layer thickness along the dome. As a result the thickness of the composite layup at the dome regions is constant.

In order to avoid rigid body motions, certain boundary conditions must be applied. For that reason, the transverse displacement ( $U_Y$ ,  $U_Z$ ) and the rotation around the longitudinal axis ( $R_X$ ) are restricted in a central node of each ending cap of the cylindrical extension of the polar boss opening (a node being in the x axis) in both ends of the pressure vessel. In that way, the model cannot move parallel to Y and Z axis or rotate around them. In addition, the longitudinal displacement ( $U_X$ ) and the transverse displacement ( $U_Z$ ) are restricted in a node, which is at the middle of the cylinder and belongs to the X-Y plane, so as to avoid the displacement parallel to X axis and the rotation around it.

Finally, the analysis was static and permitted large displacements. Additionally, the load of the analysis was an internal pressure with a maximum value of 70MPa. The maximum load was chosen so as to the aluminum liner of the pressure vessel has entered entirely in the plastic zone. The maximum value was approached with a load step equal to 1MPa, starting from 0MPa.

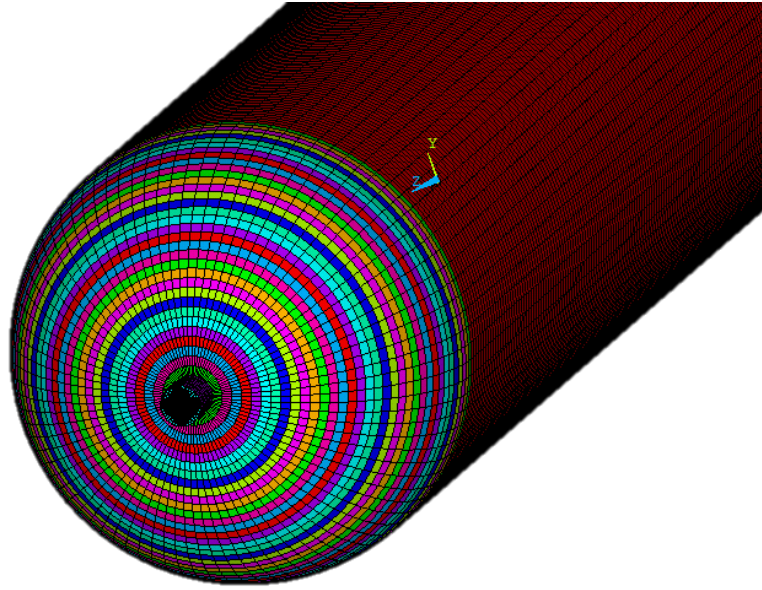


**Figure 4-3 Representation of the segmentation of domes into rings with different material orientations. Each colour corresponds to a different winding angle.**

#### 4.1.1 Mesh Convergence Analysis

Before using the model for extraction of results and conclusions, a mesh convergence analysis must be carried out. This is made in order to verify that the results are consistent and the discretization error is small. In order to check this, four different meshes were made. The first mesh consisted of 9360 elements in total, 130 longitudinally and 72 circumferentially. The second and the third mesh consisted of 88 elements circumferentially, but the second had 210 elements in the longitudinal direction, whereas the third had 230 in that direction. As a result, the total number of elements of the second mesh was 18480 and the total number of elements of the third mesh was 20240. Finally, the fourth mesh consisted of 37740 elements, 260 in the longitudinal direction and 144 in the circumferential direction.

During the construction of the meshes, special care was taken in order to keep the average aspect ratio of the elements, which is the ratio of the length of the longer side of element to the length of the shorter side, under 2 and the percentage of the elements that have an aspect ratio greater than that under 10%. Therefore, the first mesh had an average aspect ratio of 1.46, with 7.7% of its elements having an aspect ratio above 2. The second mesh had an average aspect ratio of 1.63, with 5.71% of its elements having an aspect ratio above. Additionally, the 4.35% of elements of the third mesh had an aspect ratio greater than 2 and the average aspect ratio is 1.72. Finally, the fourth mesh consisted of elements with an average aspect ratio of 1.42, with 7.69% of them having an aspect ratio greater than 2.

The mesh convergence analysis was based on the stiffness of the model. For that reason, the radial and the axial displacement of 4 points of the geometry were calculated. The locations of the 4 points are shown in Figure 4-4. The first and the fourth points have zero displacement in the axial and the radial direction respectively because of the boundary conditions, so these displacements were not included in the analysis. The value that was compared was the slope of the curve of the load displacement diagram of each point for the two aforementioned directions, which corresponds to the local stiffness of the pressure vessel in those locations. The analysis was limited in the region of load where the liner behaves

elastically, so the curve of the displacement is a line in that region and the slope is constant, as both materials behave elastically. For example, the analysis for the radial displacement of the point 1 was limited in the region of 0 to 60 MPa, as in that region the displacement increases linearly with respect to the increase of load as shown in Figure 4-5. For a load bigger than 60MPa, the aluminum liner has entered the plasticity zone. This fact can be noticed by the change of the slope at that region in Figure 4-5.

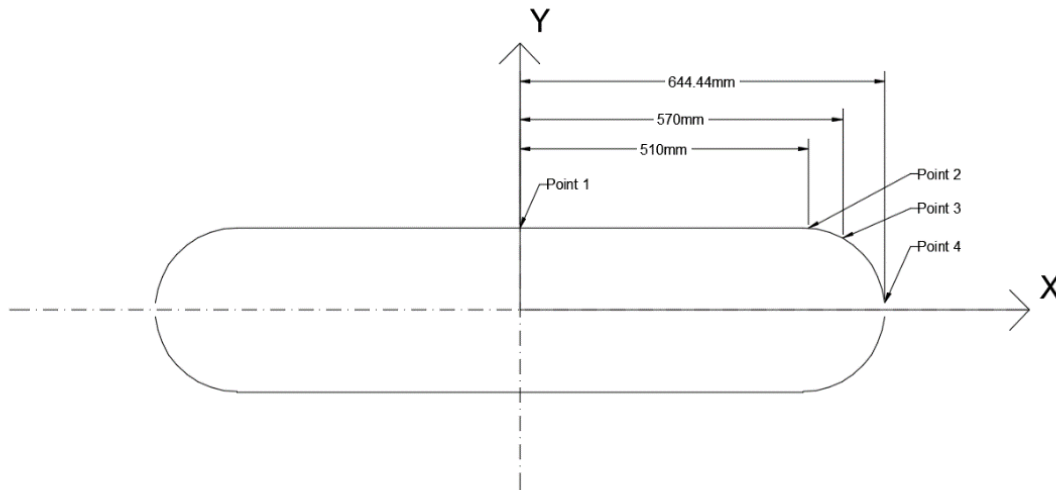


**Figure 4-4** The locations of the 4 points used in the mesh convergence analysis

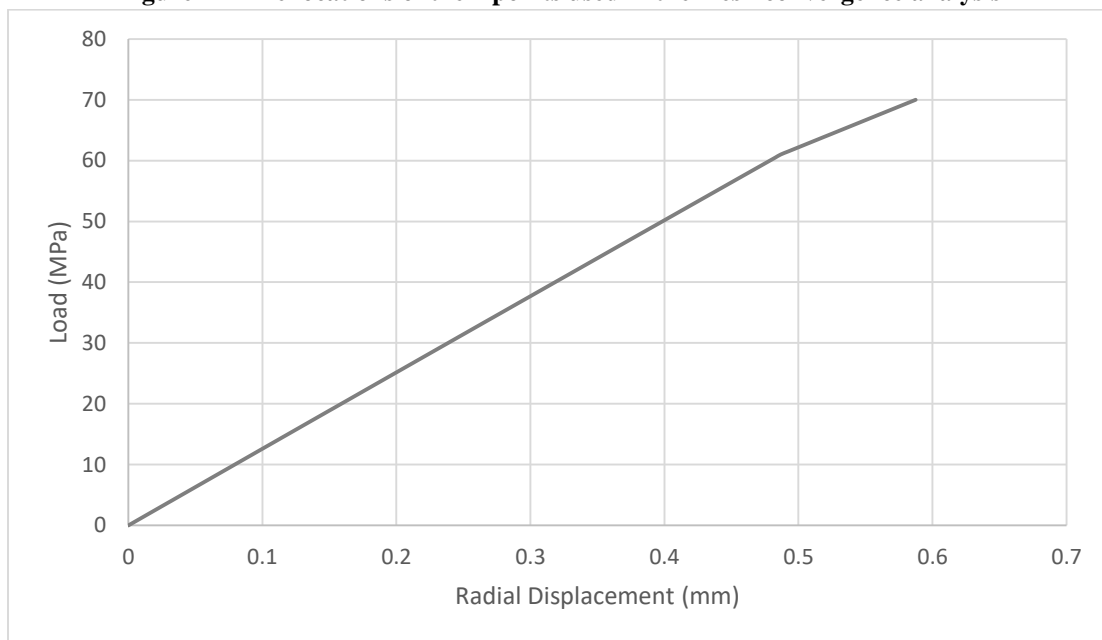


**Figure 4-5** The radial displacement - load curve of the pressure vessel at location 1

The results of the analysis are listed in Table 4-3. It is noted that with the increase of elements, only the slope of the curve of the axial displacement in location 4 changes significantly. This change is 11.7% between the two first meshes and a further increase of 6.0% between the second the third mesh. The change between the third and the fourth mesh is insignificant (approximately 1.9%). All the other slopes remain almost constant with the increase of the number of the elements, as the maximum change is 2.3% for radial



displacement in the second location between the first and the second meshes. For those reasons, the preferred mesh was the third one as it offers more reliable results compared to the first and the second mesh and the duration of its solution is shorter than that for the fourth mesh, as mesh 3 consists of fewer elements and nodes.

**Table 4-3 The slopes of the displacement – load curves. All values are in MPa/m**

Direction/location	Mesh 1	Mesh 2	Mesh 3	Mesh 4
Radial 1	125810	125772	124882	125719
Radial 2	99250	101503	101760	99143
Axial 2	62428	62816	62573	62368
Radial 3	103176	100884	100973	99436
Axial 3	59275	59105	58580	59019
Axial 4	34760	38816	41140	40342

## 4.2 Description of the new model created in Abaqus

The new model was created in Abaqus CAE environment utilizing the Wound Composite Modeler (WCM) plug-in provided by Simulia (Simulia, 2016). This plug-in creates the geometry and the mesh and assigns the material properties in each element.

First of all, the user must define the geometry of the liner, which is in fact the internal geometry of the pressure vessel. There are three ways to do so, either by using an imported 3D surface, or using a CAD design or defining analytically the general dimensions. For the purposes of this thesis, the latter option was used. The shape of both domes is spherical and the dimensions used are the same as in the model in section 4.1.

The next step is to define the materials to be used and their properties. The materials that were used, are the material that had been used in ANSYS and their properties are shown in Table 4-1 and Table 4-2. These materials are used for the creation of the liner and composite layup. This is done by the respective dialog box shown in Figure 4-6. The parameters that define the layup are the type of the layer (hoop or helical), the thickness of the layer, the winding angle, the bandwidth and the extension of the layer by defining the coordinate of the ending point as it is assumed that all layers are starting from the middle of the cylinder. As the pressure vessel is symmetrical, the user defines only the parameters for the one end. It should also be noted that each helical layer in the dialog box corresponds to a balanced angle-ply laminate, which consists of one layer with positive angle and the half thickness of the thickness defined by the user and one layer with the corresponding negative angle and the rest of the thickness. The aluminium liner is defined as a hoop layer that covers the entire surface of the pressure vessel.

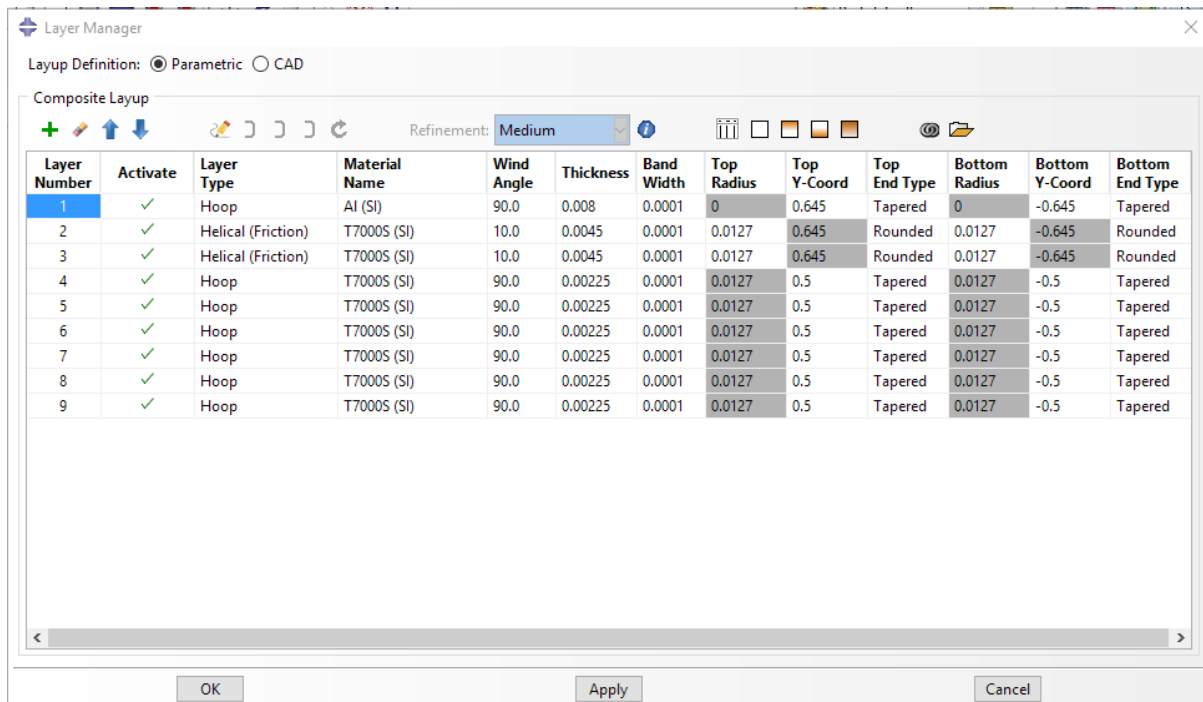


**Figure 4-6** The dialog box for the creation of the composite layup

The creation and the density of the mesh of the tank is defined solely by two parameters. These parameters are the number of elements along the longitudinal axis of the tank and the number of elements in the circumferential direction. This model consists of 230 elements in the longitudinal direction and 88 in the circumferential direction, creating a mesh of 20,240 elements in total.

Then, the material properties are assigned to each element. If the material is isotropic, its properties are assigned directly without any conversion. However, in the case of orthotropic materials, like carbon fibers, the plug-in creates a new material for each different winding angle. The way of how this procedure is made, depends on the type of the layer that it is modelled. The properties for a hoop layer occur by multiplying its stiffness matrix with the rotation matrix for an angle of 90deg. Consequently, its mechanical properties are calculated by the rotated stiffness matrix and are assigned to the elements as a new orthotropic material with these mechanical properties. On the other hand, the procedure for helical layers is more complex. As it was formerly mentioned, each helical layer corresponds to a balanced angle-ply. For that reason, the plug-in calculates the equivalent stiffness matrix of the balanced angle-ply laminate consisting of a positively directed layer and a layer directed at the respective negative angle. Therefore, having the equivalent stiffness matrix, the equivalent mechanical properties can be calculated. This procedure is repeated for every different winding angle exists in the model, as every different winding angle is modelled as a new material with each equivalent mechanical properties. The number of the new materials that are created depends on the increment which is chosen to discretize the curve of the change of winding angle along the dome. For the purposes of this analysis, it was chosen to discretize it every 0.1deg. The change of the winding angle along the dome is defined by equation (3-9).

After the creation of the geometry and the mesh, the internal pressure and the boundary conditions must be defined. The boundary conditions which were implemented are the following. First of all, the displacements in the X and Z directions of all nodes at the perimeter of both polar openings were restricted. As a result, the pressure vessel cannot move or rotate as a rigid body parallelly or around those axis. It is noted that the Y axis is the longitudinal axis of the cylinder in this model, so the displacements were restricted in both X and Z direction to maintain the rotational symmetry around the Y axis. In addition, the displacements in Y and Z direction of a node, which is in the middle of the cylinder and belongs in the X-Y plane, were restricted in order to avoid the rigid body displacement in the Y direction and the rigid body rotation around the Y axis. The node was chosen to be in the middle of the cylinder in order to maintain the symmetry of the model about the plane X-Z. Finally, the internal pressure was implemented as in section 4.1.

#### 4.2.1 Mesh convergence analysis

For the mesh convergence analysis of this model, the same procedure with that in section 4.1.1 was followed. The same values at the same locations were calculated to compare and evaluate the four different meshes. The meshes that were checked were the same as in section 4.1.1 as well. The calculated values are summarized in Table 4-4.

**Table 4-4 Mesh convergence analysis. All values are in MPa/m**

Direction/location	Mesh 1	Mesh 2	Mesh 3	Mesh 4
Radial 1	124351	124311	124311	124261
Radial 2	98819	97640	101269	98745
Axial 2	61850	61584	62299	61799
Radial 3	102588	100672	100420	101987
Axial 3	58422	58314	58305	58301
Axial 4	37439	40715	41212	41631

It is noted that the increase of the number of the elements between the first and the second mesh (from 130 elements to 210 elements longitudinally and from 72 to 88 circumferentially) lead to an 8.7% increase of the slope of the axial displacement-load curve of the fourth point. There is no other significant change between these two meshes. On the other hand, the increase from 210 elements in the longitudinal direction to 230 elements between the second and the third meshes lead to a 3.7% increase of the slope of the radial displacement-load curve of the second point. Finally, there are no significant changes between the third and the fourth meshes, so it can be concluded that the mesh has converged. For that reason, and in order to have a consistency between this model and the one created in ANSYS, the third mesh was chosen to be used for the further analysis.

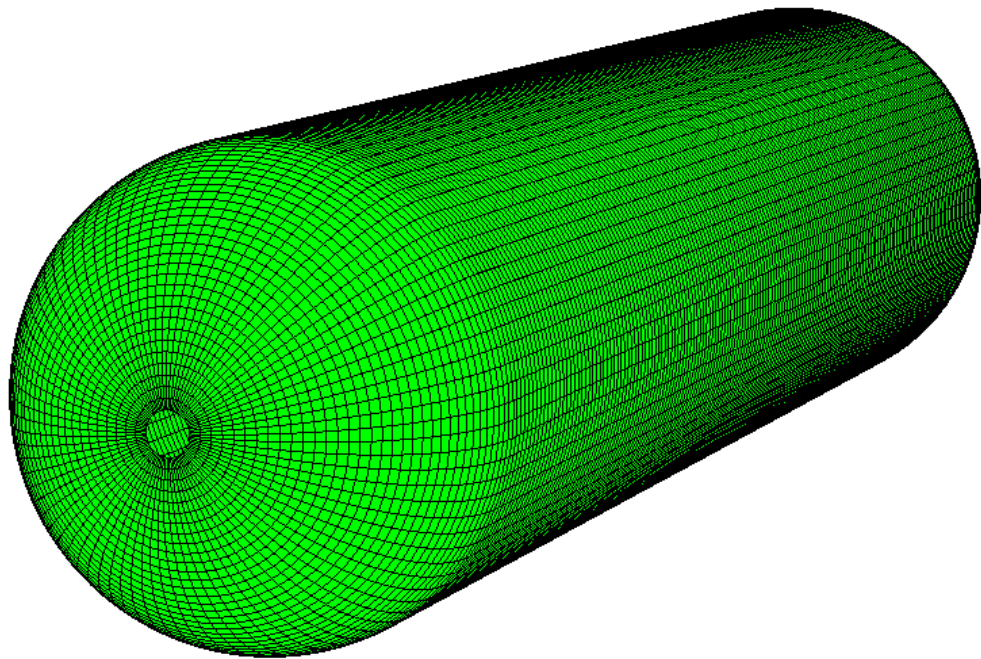


**Figure 4-7** The mesh of the model created in Abaqus that was used for the analysis

### **4.3 Comparison of ANSYS and Abaqus models**

Before the use of the new model created in Abaqus, its accuracy and veracity must be verified. This is made by comparing some results derived by it with the respective results obtained by the ANSYS model, whose veracity has been proved by Katsaounis and Tsouvalis (2014).

It should be remarked that certain modifications were taken place to the ANSYS model in order to be exactly comparable to the model created in Abaqus. First of all, the density of the mesh and its distribution along the dome were chosen to be the same in ANSYS and Abaqus models, taking in notice that in both models mesh convergence has been achieved. Furthermore, the boundary conditions at both ends were changed and they were implemented exactly as in section 4.2, instead of how they had been applied by Katsaounis and Tsouvalis (2014). As a result, there was no reason of existence for the cylindrical extensions at the two polar boss openings, thus they were deleted. Additionally, SHELL181 was used instead of SHELL281, as it is a 4-node element with the respective attributes to the element S4R that was used in Abaqus. Finally, the thickness of the liner was kept constant at 8mm throughout the entire surface of the pressure vessel.

The comparison was based on two aspects. The first aspect was the stiffness of the model, which was estimated by means of the displacements in the 4 points shown in Figure 4-4. The displacements calculated were the axial and the radial displacement of the nodes being at these points in a cylindrical coordinate system. The origin of the axis was the middle of the cylinder, the Z axis (longitudinal axis) was directed in the longitudinal direction of the cylinder and the R axis was placed in the direction of the radius of the cylinder. Therefore, the axial displacement is calculated in the direction of the Z axis and the radial displacement in the direction of the R axis of this cylindrical coordinate system.

On the other hand, the stresses at locations 1, 2 and 3 of the Figure 4-4, which are the second aspect of comparison, were calculated in the two in-plane directions of the elements

being at these points. The first direction is the longitudinal direction (parallel to the longitudinal direction of the cylinder) for point 1, which is in the cylindrical portion. The respective direction for points 2 and 3, which are in the dome region, is the meridional direction of the dome. The second direction is common for the three of the points and it is the circumferential direction. It is noted that the locations of these three points were chosen to be at three characteristic regions of the pressure vessel, the middle of the cylinder, the cylinder-dome intersection and the middle of the dome respectively. The stresses were calculated at the internal surface of the liner and at the external surface of the composite reinforcement. Thus, for the points in the dome region, the stresses were calculated at the external surface of the external helical layer and for the first point, which is in the cylindrical portion, the stresses were calculated at the external surface of the external hoop layer.

### 4.3.1 Comparison based on stiffness

As it was formerly mentioned, the comparison of the stiffness was based on the axial and the radial displacement of certain nodes for different loads of internal pressure (0 to 70 MPa). Therefore, the smaller the displacements, the stiffer the pressure vessel in that region.

The first comparison was made for the radial displacement of point 1 (Figure 4-4). Due to its location (middle of the cylinder), there is no axial displacement, as the pressure vessel is symmetrical about the Z-R plane which passes through this point. The increase of the radial displacement at point 1 as the internal pressure increases for both models (the one created in ANSYS and the one created in Abaqus) is shown in Figure 4-8.

In the aforementioned figure, it is noticed that the two curves coincide, indicating that the results derived from the two models are common. Another noticeable thing is that the slope of the curve changes at a load of 61MPa. This happens because at that load the region of the liner around point 1 is entering the plastic zone. Therefore, the stiffness of the pressure vessel in that region is decreased, resulting in greater displacements for the same increase of load (internal pressure).

The displacement-load curves of the two models coincide in any case (at the rest of the points and for both directions), so they are omitted. However, these curves can be seen in 4.4 for the model with constant thickness. Therefore, in order to compare the results of the two models, the displacements at certain loads are presented in Table 4-5 and Table 4-6. Table 4-5 contains the values of displacements at the four points for a load of 35MPa, which is the design pressure for this pressure vessel, and Table 4-6 contains the respective displacements at a load of 70MPa, at which the entire liner has entered the plastic zone.

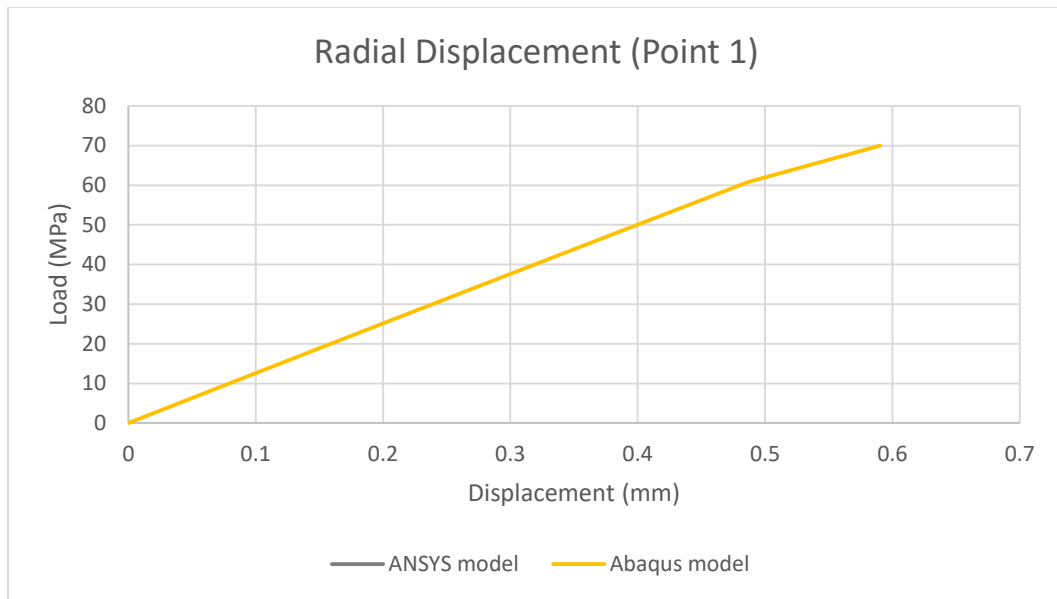


**Figure 4-8 Radial displacement-load curve of the two models at point 1**

**Table 4-5 The displacements at the four points at 35 MPa**

Point	Direction	Displacement (mm)		Difference (%)
		ANSYS	Abaqus	
1	Radial	0.278	0.279	0.2%
2	Radial	0.343	0.344	0.2%
2	Axial	0.557	0.558	0.2%
3	Radial	0.347	0.348	0.3%
3	Axial	0.594	0.595	0.2%
4	Axial	0.918	0.906	-1.3%

**Table 4-6 The displacements at the four points at 70 MPa**

Point	Direction	Displacement (mm)		Difference (%)
		ANSYS	Abaqus	
1	Radial	0.587	0.590	0.5%
2	Radial	1.087	1.097	0.9%
2	Axial	1.331	1.340	0.6%
3	Radial	1.698	1.715	1.0%
3	Axial	1.478	1.490	0.8%
4	Axial	1.196	1.239	3.6%

It is noted that in both cases (35 and 70 MPa) the differences between the two models are negligible. However, at the pressure of 70MPa at point 4 there is a considerable increase of the axial displacement.

All in all, it can be concluded that, in terms of stiffness, the two models are similar.

### 4.3.2 Comparison based on the developed stresses

After the comparison of the stiffness, the developed stresses at certain points were compared. The comparison was divided in the comparison of the stresses developed in the

liner and the stresses developed in the composite reinforcement. The locations of the points, that the stresses were calculated, were chosen to cover three characteristic regions of the pressure vessel. Point 1 is placed at the middle of the cylinder, point 2 is placed at the cylinder-dome intersection, and the third point is placed at the middle of the dome. The stresses were calculated at the design pressure (35MPa) and at a pressure where the entire liner has von Mises stresses over the yield stress of the aluminium (276MPa).

The stresses in the liner were calculated in the circumferential direction at its internal surface. The circumferential direction was chosen, as for isotropic materials, the stresses in this direction are always greater than the stresses in the longitudinal direction. The equivalent von Mises stress was also calculated at the same locations.

The stresses at an internal pressure of 35MPa are shown in Table 4-7 and at the pressure of 70MPa in Table 4-8.

**Table 4-7 Stresses in the liner at an internal pressure of 35MPa**

Point	Direction	$\sigma$ (MPa)		%
		ANSYS	Abaqus	
1	Von Mises	158.0	158.3	0.2%
1	Circumferential	175.0	175.7	0.4%
2	Von Mises	179.0	179.3	0.2%
2	Circumferential	205.0	206.0	0.5%
3	Von Mises	203.0	203.7	0.3%
3	Circumferential	234.0	234.7	0.3%

**Table 4-8 Stresses in the liner at an internal pressure of 70MPa**

Point	Direction	$\sigma$ (MPa)		%
		ANSYS	Abaqus	
1	Von Mises	278.0	277.6	-0.1%
1	Circumferential	305.0	305.4	0.1%
2	Von Mises	284.0	283.0	-0.4%
2	Circumferential	322.0	322.2	0.1%
3	Von Mises	290.0	290.3	0.1%
3	Circumferential	328.0	329.5	0.5%

It can be noticed that for both internal pressures, the differences between the results obtained by the ANSYS model and those obtained by the model created in Abaqus are small. This indicates that the liners of the two models are identical in terms of developed stresses.

Furthermore, the stresses in the external surface of the composite reinforcement were calculated at the same points. For point 1, which is in the cylindrical portion of the pressure vessel, the stress was calculated at the external surface of the external layer of the composite layup, which is the 6<sup>th</sup> hoop layer. For the rest of the points, which are located at the dome regions of the pressure vessel, the stresses were calculated at the external surface of the external helical layer, as there is no hoop layer in that region. The stresses were calculated in both circumferential and longitudinal directions. For the points located at the domes, the longitudinal direction is the meridional direction.

The stresses at a pressure of 35MPa are shown in Table 4-9 and at a pressure of 70MPa in Table 4-10.

**Table 4-9 Stresses in the composite reinforcement at 35MPa**

Point	Direction	$\sigma$ (MPa)		%
		ANSYS	Abaqus	
1	Longitudinal	13.0	13.1	0.8%
1	Circumferential	258.0	258.3	0.1%
2	Meridional	182.0	183.3	0.7%
2	Circumferential	28.6	28.6	0.0%
3	Meridional	179.0	181.9	1.6%
3	Circumferential	32.1	31.0	-3.4%

**Table 4-10 Stresses in the composite reinforcement at 70MPa**

Point	Direction	$\sigma$ (MPa)		%
		ANSYS	Abaqus	
1	Longitudinal	27.9	28.1	0.7%
1	Circumferential	543.0	546.2	0.6%
2	Meridional	383.0	388.9	1.5%
2	Circumferential	84.1	84.9	1.0%
3	Meridional	615.0	631.8	2.7%
3	Circumferential	144.0	142.2	-1.3%

It is notable that at both pressures the differences between the results of the model created in ANSYS and those obtained by Abaqus are relatively small. However, the differences in the composite layup are greater than those in the liner were. This could be explained by the different method of modelling of helical layers presented in section 4.2.

Another notable observation is that the stresses are considerably greater in the direction that is nearer to the direction of the winding. Therefore, the circumferential stress is greater than the longitudinal stress at point 1, as in that region the winding is made in the circumferential direction (the winding angle is 90deg). Respectively, the meridional stress is greater than the circumferential at the other points, as in those regions the winding is made with an angle of 10deg. This happens due to the orthotropic nature of the material, which has greater stiffness in the winding direction. This does not happen in the liner as it is constructed with an isotropic material.

In general, it can be concluded that the model created in Abaqus produces similar results to the model created in ANSYS by Katsaounis and Tsouvalis (2014). Therefore, the accuracy and veracity of the model created in Abaqus can be considered proven.

#### 4.4 Evaluation of the impact of the increasing thickness at domes

After the verification of the accuracy of the general structure of the model, a new feature was introduced. As it was mentioned in section 3.2, the thickness of the composite layup at the domes is not constant. In fact, it builds up along the dome. For that reason, the model described in 4.2 was modified in order to include the building up thickness. The



equation that was used to describe this behavior is eq. (3-11). As it was described in section 3.2, the degree of the building up thickness is depended on the diameter of the dome and the bandwidth. The bandwidth was chosen to be 30 mm taking into account information given from the manufacturer (B&T Composites) and the specific geometry of the pressure vessel. Therefore, the thickness builds up from 9mm to approximately 22mm. A cross-section of a dome with constant thickness and a cross-section of a dome with increasing thickness are shown in Figure 4-9. It should be noted that the thickness at the dome-cylinder conjunction is equal for both models.

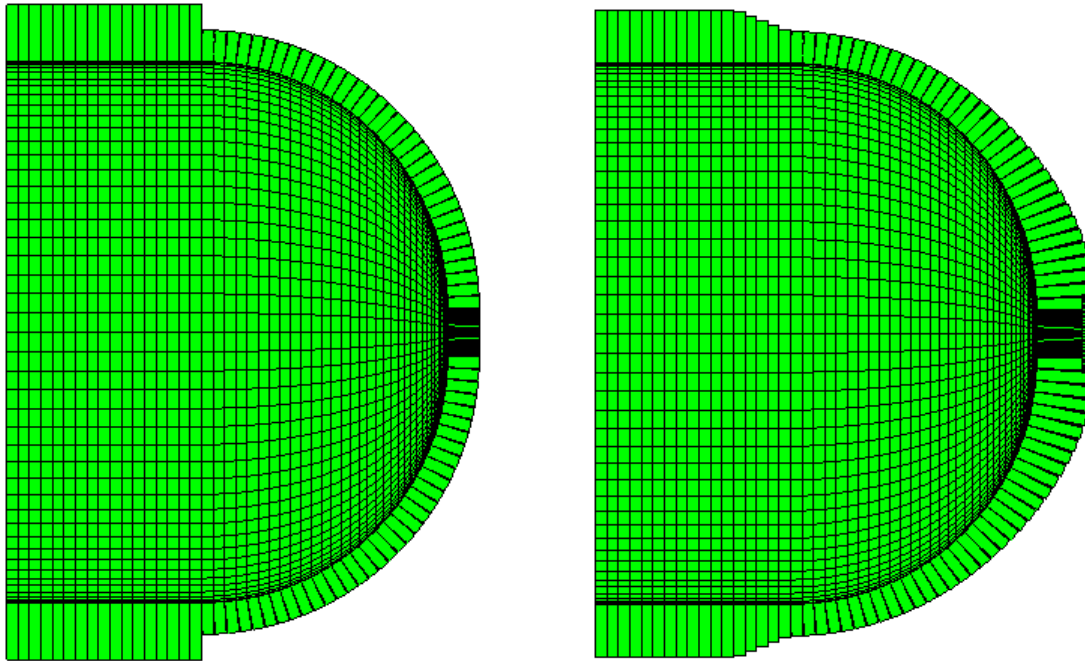


**Figure 4-9 Cross-section of the dome with constant thickness (left) and increasing thickness (right)**

In Figure 4-9, the gradual build-up of thickness along the dome can be noticed. The difference between the thickness at the cylindrical portion and the dome because of the hoop layers can also be noticed. A fillet at the ending of the hoop layers has been added in the Abaqus model for a better simulation of the real construction. The length in which the fillet is extended depends on the bandwidth, which for the purpose of this case was chosen to be 30mm. The fillet had not been used in the creation of the model with constant thickness, in order to be comparable to the older model created in ANSYS. It should be noted that the thickness of the liner is included in the representation.

The comparison between the two cases was based on the displacements of the nodes at the four points which were previously use. The radial displacement of the node at the middle of the cylindrical portion (point 1) is shown in Figure 4-10. The build-up of thickness at the domes results in an approximate 15% increase of the radial displacement at the middle of the cylinder for the same internal pressure. The increase is greater when the stresses in liner have exceeded the yield stress, reaching up to 20%. Finally, it can be noticed that the load in which the stresses in liner at that region exceed the yield stress is decreased, as the slope of the curve of the model with increasing thickness changes for smaller value of load.

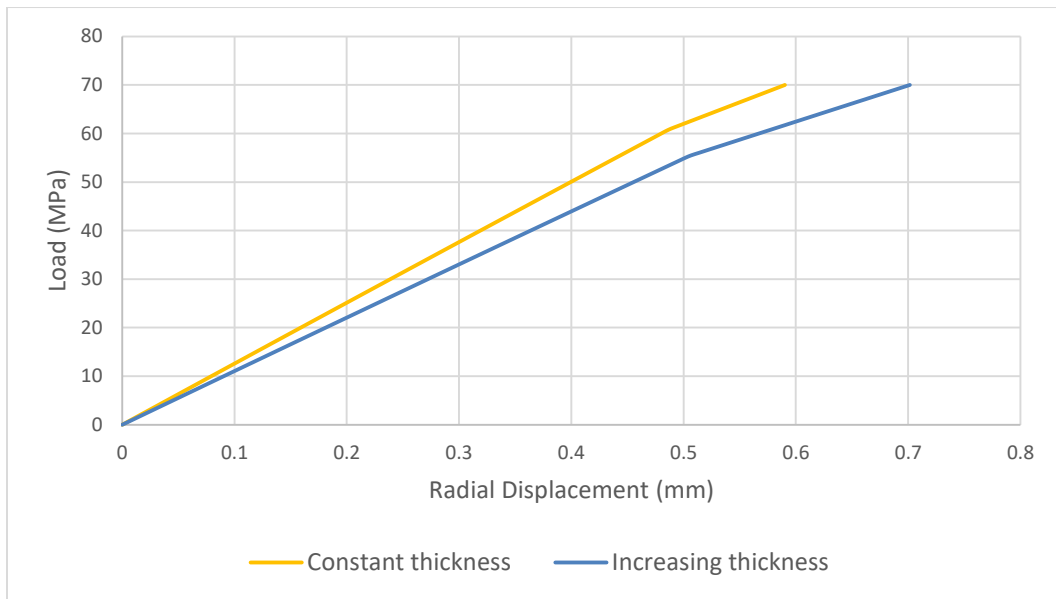


**Figure 4-10 Radial displacement at the middle of the cylinder (point 1)**

The next comparison of the two models is in the region of the dome-cylinder intersection (point 2). The radial and the axial displacement of a node in that location are compared. The radial displacement is shown in Figure 4-11 and the axial displacement in Figure 4-12. It can be noted that the increasing thickness at domes results in a significant increase of the radial displacement in the region, whereas the axial displacement remains almost the same. The increase of the radial displacement is approximately 35%, when the stresses in liner are under the yield stress, and there is a further increase up to approximately 55%, when the yield stress has been exceeded.

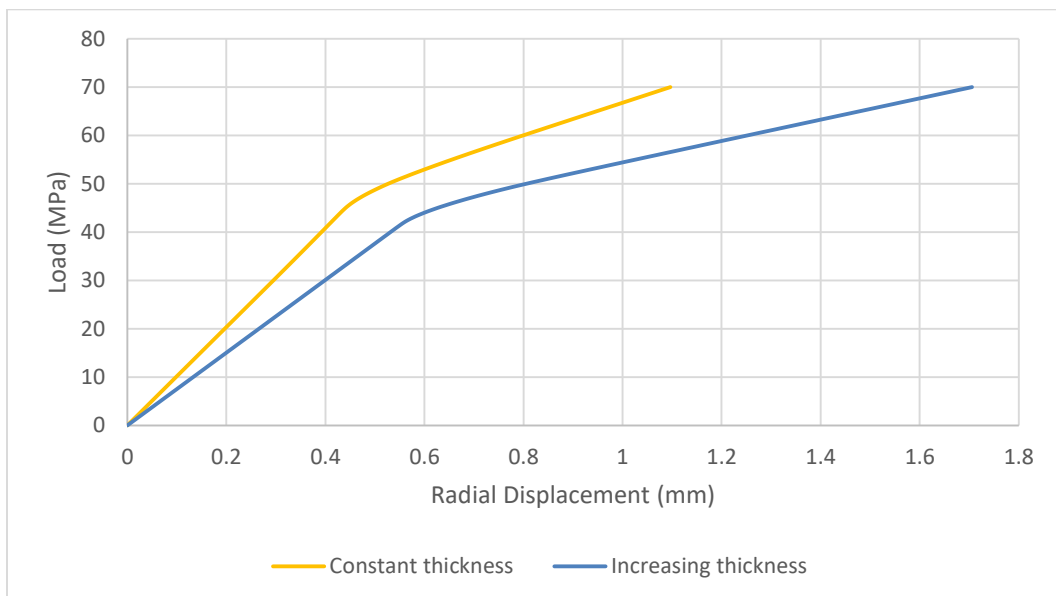


**Figure 4-11 Radial displacement at the dome-cylinder intersection (point 2)**

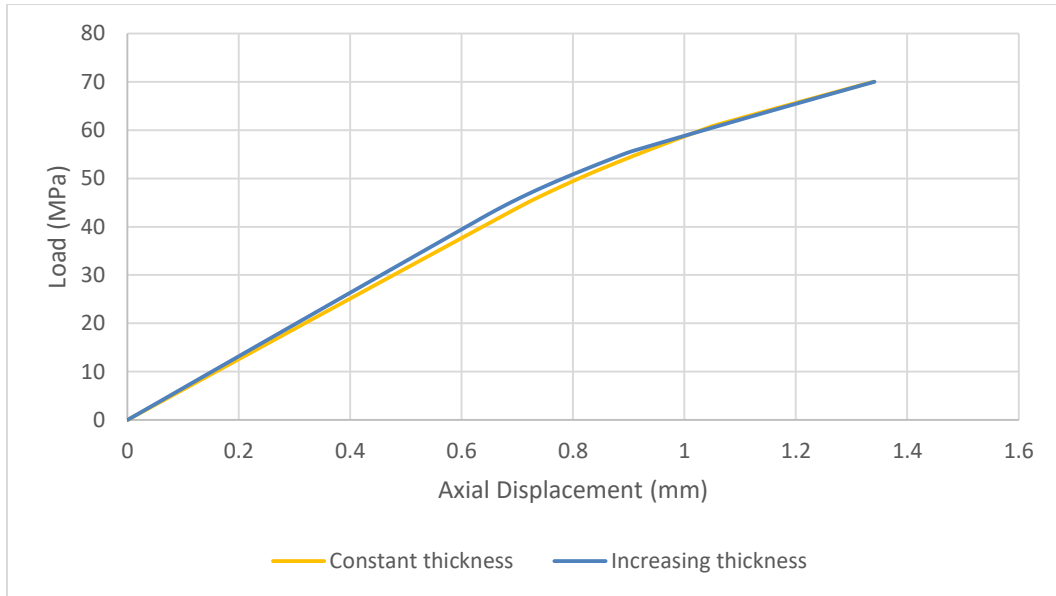


**Figure 4-12 Axial displacement at the dome-cylinder intersection (point 2)**

In addition, the middle of the dome (point 3) was also examined. The radial displacement and the axial displacement in the region are shown in Figure 4-13 and Figure 4-14 respectively. It can be noticed that the displacement in the radial direction is similar, whereas the displacement in the axial direction for the same load slightly decreased. The decrease is approximately 10%, when the liner behaves elastically, and approximately 20% in the load region where there is plastic deformation in the liner. This indicates that the increased thickness of the composite reinforcement in the region increased the stiffness of the pressure vessel in that region.

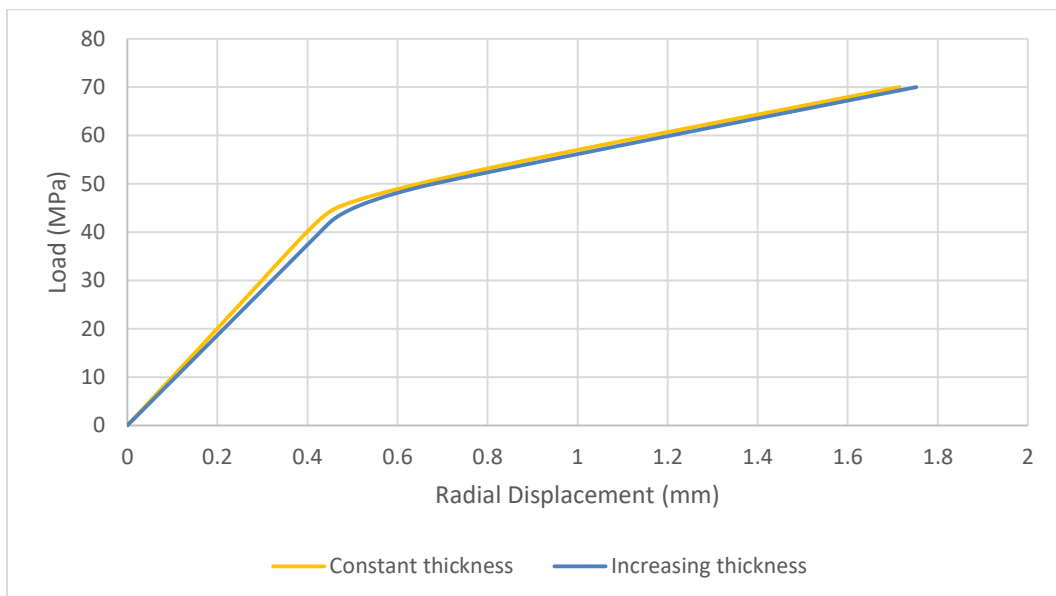


**Figure 4-13 Radial displacement at the middle of the dome (point 3)**

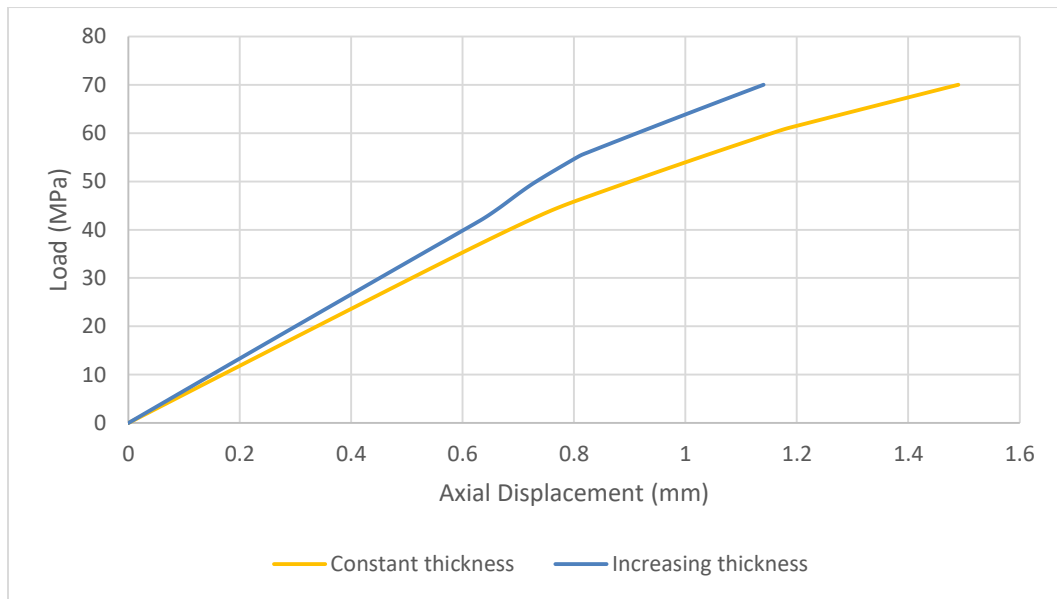


**Figure 4-14 Axial displacement at the middle of the dome (point 3)**

Finally, the top of the dome was examined (point 4). In this location, the radial displacement is restricted by the boundary condition, so the examined node could move only in the axial direction. The curve of the axial displacement is shown in Figure 4-15. The decrease of the displacement for the same load is significant. It is also notable that for load greater than 58MPa the axial displacement becomes negative as the top region of the dome moves towards the middle of the pressure vessel. This happens because the radial displacement at the cylindrical part is increasing rapidly, thus the material of the pressure vessels has the tendency to be concentrated towards the middle of the cylindrical portion. However, this behavior is not realistic as prior to that load the pressure vessels would probably have failed.

To summarize, it can be concluded that the building up of thickness at domes results in greater radial displacements in the middle of the pressure vessel and lower axial displacements at the dome regions. This is made because of the greater stiffness of domes derived from the increased thickness. As a result, the pressure vessel enlarges radially rather than to elongate.

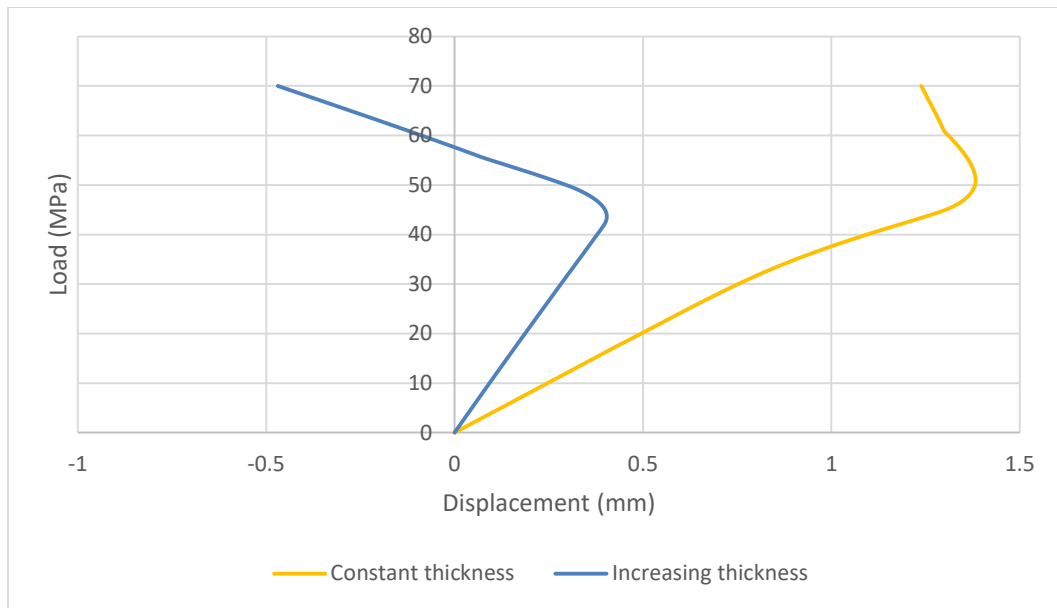


**Figure 4-15 Axial displacement at the top of the dome (point 4)**

A comparison of the deformed shape of the two models can verify the aforementioned conclusions. The comparison was made at a load equal to 35MPa, where both models had Von Mises stresses on the liner lower than the yield stress at their entire surface. The deformed shape and the undeformed shape of the model with constant thickness at the dome region is shown in Figure 4-16 and those of the model with increasing thickness at the dome region in Figure 4-17. It is notable that the pressure vessel with the increasing thickness has increased radial deformation close to the dome-cylinder conjunction and lower axial deformation near the polar boss opening. This happens due to the increased stiffness derived by the increased of the thickness composite reinforcement in that region.

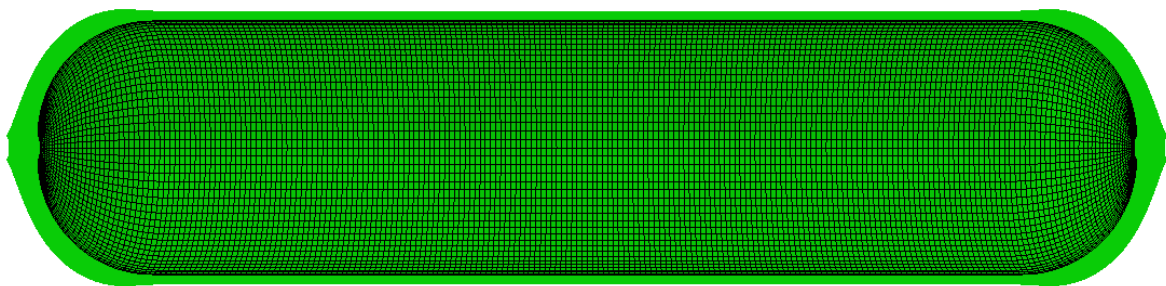


**Figure 4-16 Comparison of deformed (coloured) and undeformed (grid) shape of the pressure vessel with constant thickness at the dome region at 35MPa. The displacements of the deformed shape have been scaled 40 times in order to be distinct**

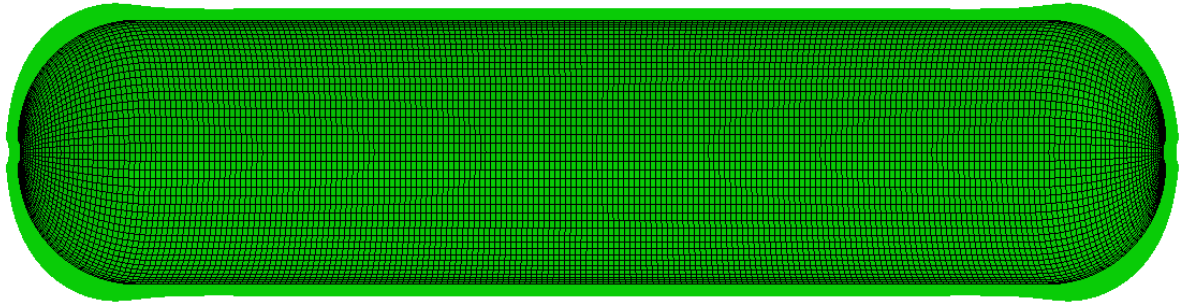


**Figure 4-17 Comparison of deformed (coloured) and undeformed (grid) shape of the pressure vessel with increasing thickness at the dome region at 35MPa. The displacements of the deformed shape have been scaled 40 times in order to be distinct**

## Chapter 5 Case Study

### 5.1 General description of the initial design of the case study

As the accuracy of the model created in section 4.2 is verified, it can be used to create the model of the case study. For that purpose, certain modifications must be made. The size of the pressure vessel is changed. The dimensions of the pressure vessel were selected so that the pressure vessel can be fitted in a standard 20-foot container in the direction of the width. For that reason, the internal diameter of the pressure vessel was chosen to be 0.45m, so that 4 pressure vessels can be stacked the one above the other, as the internal height of the container is 2.385m. In addition, the overall length of the pressure vessel must not exceed the internal width of the container, which is 2.35m (Evergreen, 2017). Therefore, the pressure vessel has approximately 1.95m internal length (1.5m is the length of the cylindrical portion and approximately 0.45m is the length of the two spherical domes together) and 0.45m internal diameter. Finally, there are two boss holes (one at each dome) which have an internal diameter of 25.4mm.

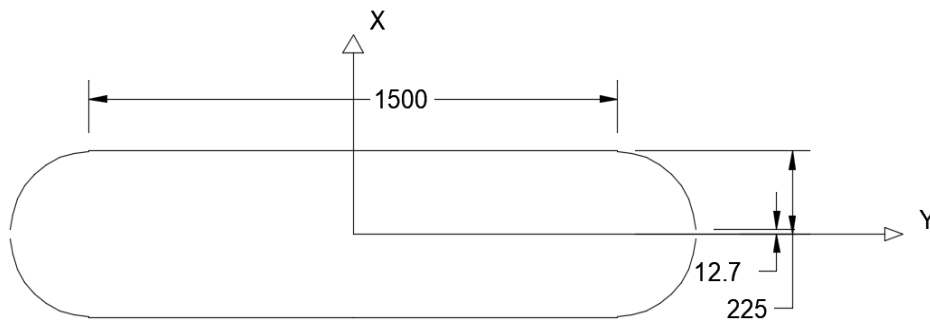


Figure 5-1 The geometry and the internal dimensions of the pressure vessel

The initial design of the case study consists of an aluminum liner with a thickness of 6mm and a carbon reinforcement with a total thickness of 30mm in the cylindrical portion. The liner thickness was chosen to be similar with the liner thickness used by Katsaounis and Tsouvalis (2014) and the total thickness of the composite reinforcement was chosen arbitrarily. The stacking sequence consists of 7 helical layers (each layer is a balanced angle-ply laminate) and 3 hoop layers. The 70-30 distribution of thickness was chosen based on relative literature (Katsaounis and Tsouvalis, 2014) Therefore, the initial thickness at the dome areas is 21mm and it increases along the dome according to equation (3-11). The winding angle was chosen according to equation (3-1), with a slippage coefficient equal to 0.3, in order to avoid the slippage of the fibers at the domes, as it was described in section 3.2.1. As a result, the maximum winding angle for the specific geometry (spherical dome with 450mm internal diameter) is 8.7deg. Another necessary parameter for the winding to be

defined is the bandwidth, which was chosen to be 30mm based on information obtained by the manufacturers (B&T Composites).

The mechanical properties of the materials which were used for the analysis are taken from bibliographic references. The properties of the aluminium for modelling the liner are obtained by Katsaounis and Tsouvalis (2014) and they have been presented in Table 4-1. As for the mechanical properties of the carbon reinforcement, the properties are derived by tests made in the Shipbuilding Technology Laboratory of National Technical University of Athens. In particular, the elastic modulus of the fiber in the direction of the fiber ( $E_1$ ) is different for helical layers and for hoop layers and their values are according to Papadakis et al. (2017). In addition, the rest of the elastic moduli ( $E_2, E_3$ ) and the values of shear moduli ( $G_{12}, G_{13}, G_{23}$ ) are common for hoop layers and helical layers and are according to the results of the tests made by Konstantinidis (2016). Furthermore, the values of Poisson's ratio are derived by Papadakis and Tsouvalis (2015). Finally, the values of the ultimate stresses in the fiber direction for helical and for hoop winding are obtained by Papadakis et al. (2017). Table 5-1 contains the values of the mechanical properties and the ultimate stresses used.

**Table 5-1 The mechanical properties of the carbon reinforcement (in MPa)**

$E_1$ (helical)	151000	from tests (Papadakis et al., 2017)
$E_1$ (hoop)	131900	from tests (Papadakis et al., 2017)
$E_2$	10900	from tests (Konstantinidis, 2016)
$E_3$	10900	equal to $E_2$ (assumption)
$G_{12}$	5700	from tests (Konstantinidis, 2016)
$G_{23}$	2850	equal to $0.5G_{12}$ (assumption)
$G_{13}$	5700	equal to $G_{12}$ (assumption)
$\nu_{12}$	0.32	from tests (Papadakis and Tsouvalis, 2015)
$\nu_{23}$	0.46	from tests (Papadakis and Tsouvalis, 2015)
$\nu_{13}$	0.32	equal to $\nu_{12}$ (assumption)
$\sigma_{utl}$ (helical)	2500	from tests (Papadakis et al., 2017)
$\sigma_{utl}$ (hoop)	1560	from tests (Papadakis et al., 2017)
$\tau_u$ (helical)	625	equal to $\sigma_{utl}$ (helical)/4 (assumption)
$\tau_u$ (hoop)	390	equal to $\sigma_{utl}$ (hoop)/4 (assumption)

The geometry was meshed with S4R shell elements, which are 4-node linear elements. This type of element allows transverse shear deformation as it uses the thick shell theory (Simulia, 2014). It also accounts for finite membrane strains and arbitrarily large rotations making it suitable for large-strain analysis. Finally, it uses reduced integration to form the element stiffness reducing in that way the running time significantly, without affecting the accuracy of the results (Simulia, 2014). Shell elements can be used for the analysis of this structure as the diameter to thickness ratio is 12.5. As for the mesh, 260 elements along the longitudinal direction were used and 104 in the circumferential direction, resulting in a total number of 27,040 elements. The number of the elements were chosen after a mesh convergence study that will be described in section 5.1.1.

In order to simulate better the real situation and to avoid rigid body motion, several boundary conditions were used. Before listing the restricted translations and rotations, it



should be noted that the directions of the boundary conditions are according to a global Cartesian system. The pressure vessel is placed in the space in a way that its longitudinal axis coincide with the Y axis of the system and the starting point of the system is at the middle of the cylindrical portion of the pressure vessel. As a result, the X and Z axis are directed in the radial direction of the pressure vessel. Having said that, the applied boundary conditions can be described. First of all, the translation along the Y axis of a node, which belongs to the X-Y plane and it is located at the middle of the cylindrical portion of the pressure vessel, was restricted. In that way, the rigid body displacement along the Y axis is restricted and the symmetry about the X-Z plane is maintained.

Furthermore, the rest of the rigid body translations and rotations must be restricted. For that reason, two rigid bodies were defined at the two boss holes (one at each boss hole). Each rigid body consists of a reference node, which is the center of the hole and it determines the motion of the rigid body, and several nodes, which are the nodes located at the perimeter of the hole. The nodes are constraint to the reference node with a tie constraint, meaning that their translational and rotational degrees of freedom are associated with the rigid body (Simulia, 2014). As a result, the diameter of the boss hole cannot enlarge and the boss hole functions as a cap. As it is considered as a cap, a force must be applied at the center of each rigid body (reference node) in order to simulate the internal pressure that would be applied at it. The value of this force is defined by the internal pressure applied at the rest of the pressure vessel and the area of the boss hole. Finally, the displacements of the reference nodes (one at each boss hole) along the X and the Z axis are restricted so as to avoid the rigid body motion of the pressure vessel along those axis and the rigid body rotation around them.

The pressure vessel is designed to operate at a pressure of 25MPa (250bar). As a result, in order to comply with the regulations described in section 2.3, the pressure vessel must withstand at least a pressure of 56.25MPa (562.5bar) (safety factor 2.25). Therefore, the internal pressure for the solution is defined at 60MPa, which exceeds the required pressure.

### 5.1.1 Mesh convergence analysis

In order to get consistent and accurate results, the required number of the elements and their distribution must be defined. This is made by conducting a mesh convergence analysis. For that reason, three different meshes were checked. The first mesh had 200 elements in the longitudinal direction and 88 in the circumferential, resulting in a total of 17600 elements. The second mesh had 260 elements in the longitudinal direction and 104 in circumferential direction, thus the total number of elements was 27040. Finally, the third mesh had 330 elements in the longitudinal direction and 112 elements in the circumferential direction. The number and the distribution of the elements were chosen in that way so that the aspect ratio of the elements would not exceed the value 10.

As it was mentioned before, the load-displacement curve of any node of the pressure vessel consists of two regions. In the first region, the pressure vessel behaves elastically and in the second region the pressure vessel behaves plastically at this node. The curve can be approximated by two different straight lines, one for each region. The slope of these two lines were used to determine the convergence of the mesh.

The two locations, at which the displacements were calculated, are the middle of the cylindrical portion and the polar boss region. At the cylindrical portion, the radial displacement was calculated only, as the axial displacement is null due to the X-Z symmetry. Respectively, at the polar boss opening, the axial displacement was calculated, as the radial displacement is null due to the applied constraints at the region (rigid links).

**Table 5-2 Comparison of the three meshes based on the slope of the load-displacement curve of the radial displacement at the middle of the cylinder**

Mesh	Number of Elements			Slope (MPa/m)		Change (%)	
	Longitudinal	Circumferential	Total	Elastic	Plastic	Elastic	Plastic
1	200	88	17600	37273	27066	-	-
2	260	104	27040	38339	27932	2.9%	3.2%
3	330	112	36960	38506	27933	0.4%	0.0%

**Table 5-3 Comparison of the three meshes based on the slope of the load-displacement curve of the axial displacement at the polar boss opening**

Mesh	Number of Elements			Slope (MPa/m)		Change (%)	
	Longitudinal	Circumferential	Total	Elastic	Plastic	Elastic	Plastic
1	200	88	17600	-113443	-22791	-	-
2	260	104	27040	-118466	-23578	4.4%	3.5%
3	330	112	36960	-120903	-23706	2.1%	0.5%

As it can be seen in Table 5-2 and Table 5-3, the increase of the number of elements between the first and the second mesh, resulted in a change of the slopes of the curve of radial displacement of approximately 3% and a change of the slopes of the curve of axial displacement of approximately 4%. This indicates that mesh convergence cannot be achieved with the use of the first mesh. On the other, the respective changes between the second and the third meshes are practically null (with the exception of the change of the slope of the axial displacement curve in the elastic region, where the change is 2.1%). Therefore, it can be concluded that the second mesh can produce accurate results, as the increase of the number of elements did not change significantly the produced results.

As a result, the mesh that will be used for the following analyses consists of 260 elements in the longitudinal direction and 104 elements in the circumferential direction. The aspect ratio of the elements at the cylindrical portion is 1.63 and only the 5.38% of the total 27040 elements have an aspect ratio greater than 2.

### 5.1.2 Results of the initial design

The burst pressure of the pressure vessel must be greater than 56.25MPa. The burst pressure is defined as the pressure where there is fracture either of the aluminium liner or of the composite reinforcement. As a result, the burst pressure is defined as the lower of the pressure where the von Mises stresses in liner exceed the ultimate stress of the aluminium (310MPa) and the pressure where the Tsai-Wu index in the composite exceeds the value 1.

According to the results of the analysis, the pressure vessel failed due to the fracture of the liner at a load equal to 60 MPa. At that pressure, the von Mises stress in the liner exceed the ultimate stress of the aluminium resulting in fracture of the liner. This happens in

a region close to the polar boss opening. The distribution of the von Mises stress on the internal surface of the liner is shown in Figure 5-2.

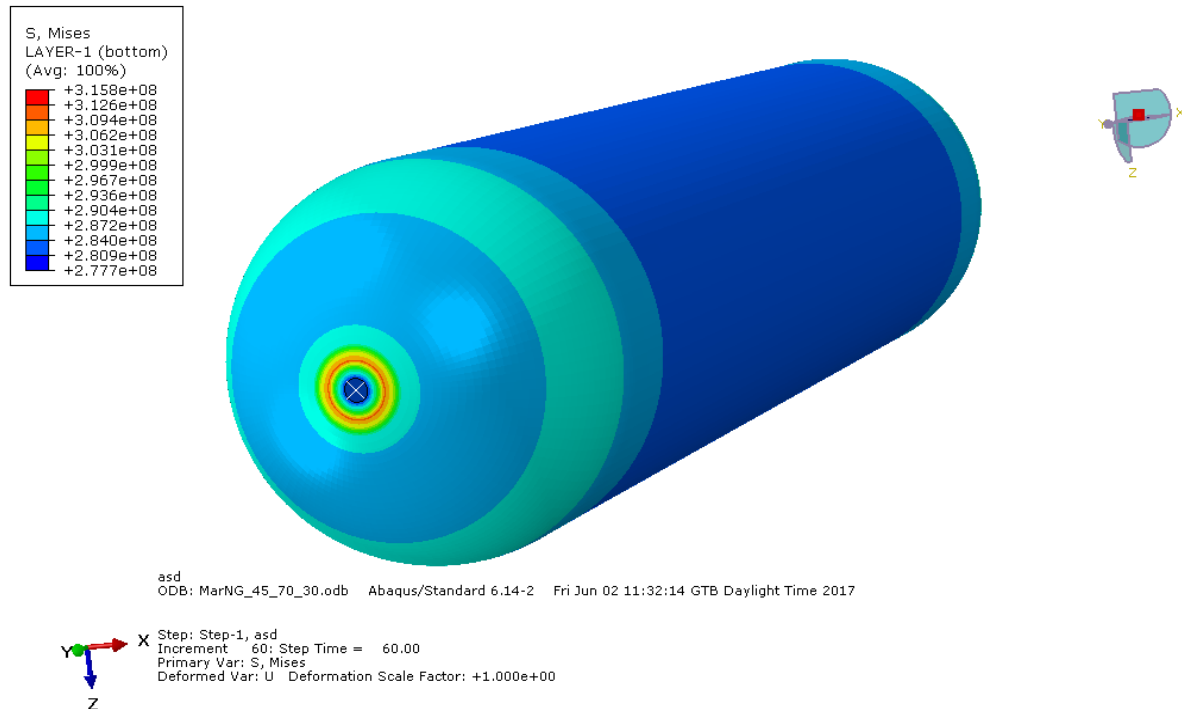


**Figure 5-2 The distribution of the von Mises stress in the internal surface of the liner at an internal pressure of 60MPa (Pa)**

In order to exclude the possibility of failure of the composite prior to the failure of the liner, the maximum value of the Tsai-Wu at the same internal pressure was checked. The maximum value of the index is observed in the 1<sup>st</sup> (internal) hoop layer at the region of the dome-cylindrical portion interface and it is 0.8405. Thus, there is no failure of the composite for internal pressure up to 60MPa, verifying in that way that the failure of the structure is due to the fracture of the liner. The distribution of the Tsai-Wu index in the 1<sup>st</sup> hoop layer is shown in Figure 5-3. The white-grey regions depict the regions of the model, which the layer does not cover.

Firstly, the shape of the deformed model is checked. A cross-section of the deformed shape (coloured) and the undeformed shape of the model (grid) at 60 MPa (failure load) is shown in Figure 5-4. The undeformed shape is scaled 50 times in order to be distinct. It is noticed that there is a region at each dome, near the dome-cylinder intersection, where the radial displacement is the greatest and as a result a local bending is presented. This fact is the reason of the increased Tsai-Wu index in that area, as due to the local bending, the radial displacement increases. Therefore, the hoop stresses, which are also the stresses in the fiber direction for the hoop layers, are increased, resulting in an increased value of Tsai-Wu index. Another noticeable fact is that the top of the dome moves towards the middle of the pressure vessel, resulting in negative axial displacements in the region and bending of the dome.

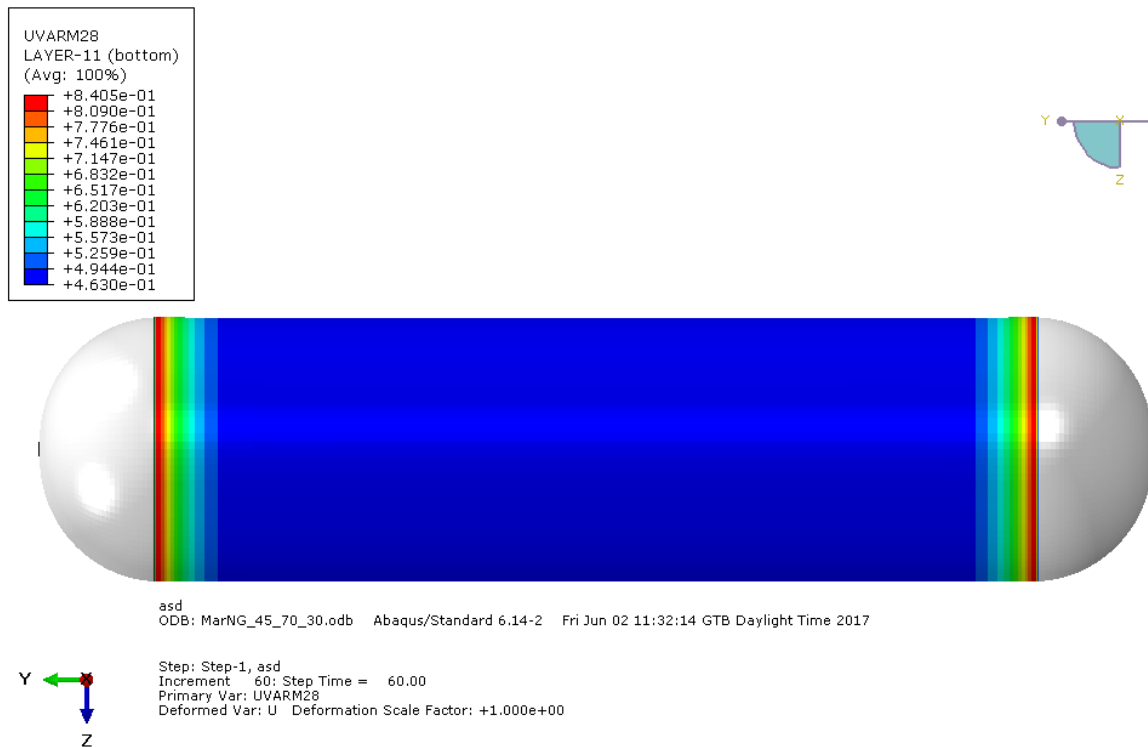


**Figure 5-3 Tsai-Wu index in the 1st (internal) hoop layer at 60MPa**

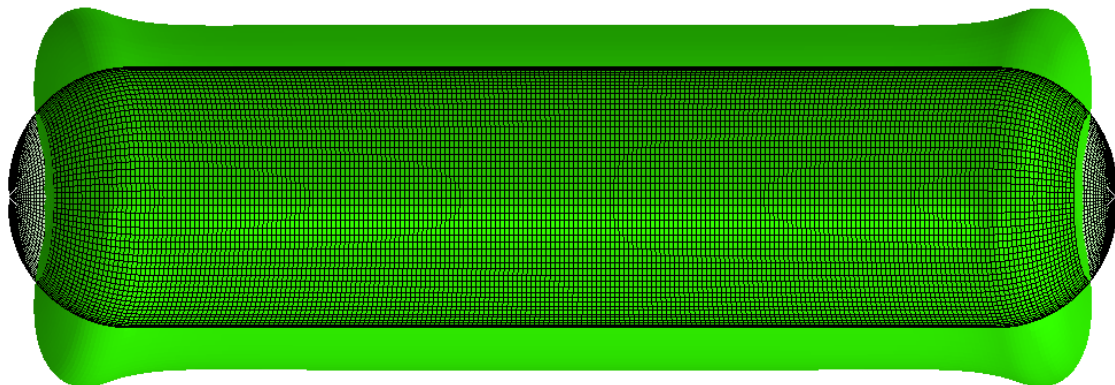


**Figure 5-4 The undeformed shape (grid) and the deformed shape (coloured) of the model at 60MPa. The deformed shape is scaled 50 times in order to be distinct. The coloured distribution shows the magnitude of the displacements**

In order to have an estimation of the stiffness of the structure, the maximum values of the axial and radial displacement were calculated at the operating pressure (25MPa). The displacements were calculated in a global cylindrical coordinate system, with the longitudinal axis of the pressure vessel being in the axial direction. The maximum value of the axial displacement is 0.41mm and it is located at the dome-cylinder intersection region, and the maximum radial displacement is 0.75mm and it is located at the same region. The distribution of the axial and radial displacement at a pressure of 25MPa is shown in Figure 5-5 and Figure 5-6 respectively.

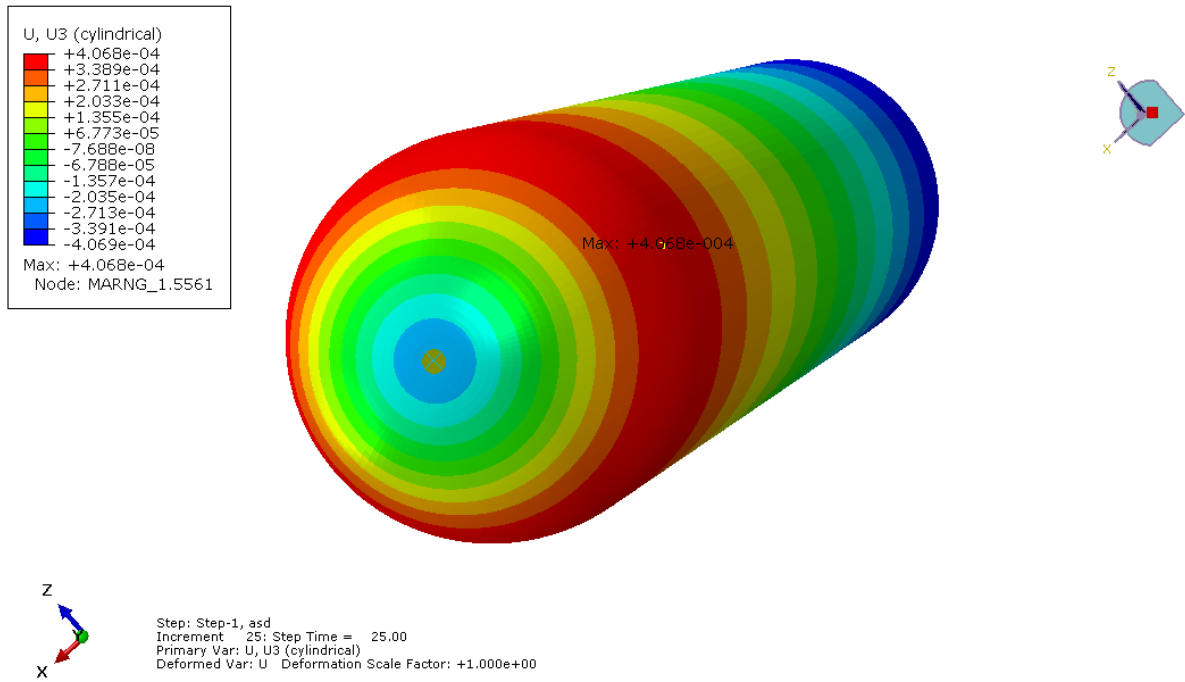


**Figure 5-5** The distribution of axial displacements at operating pressure (25 MPa) (m)

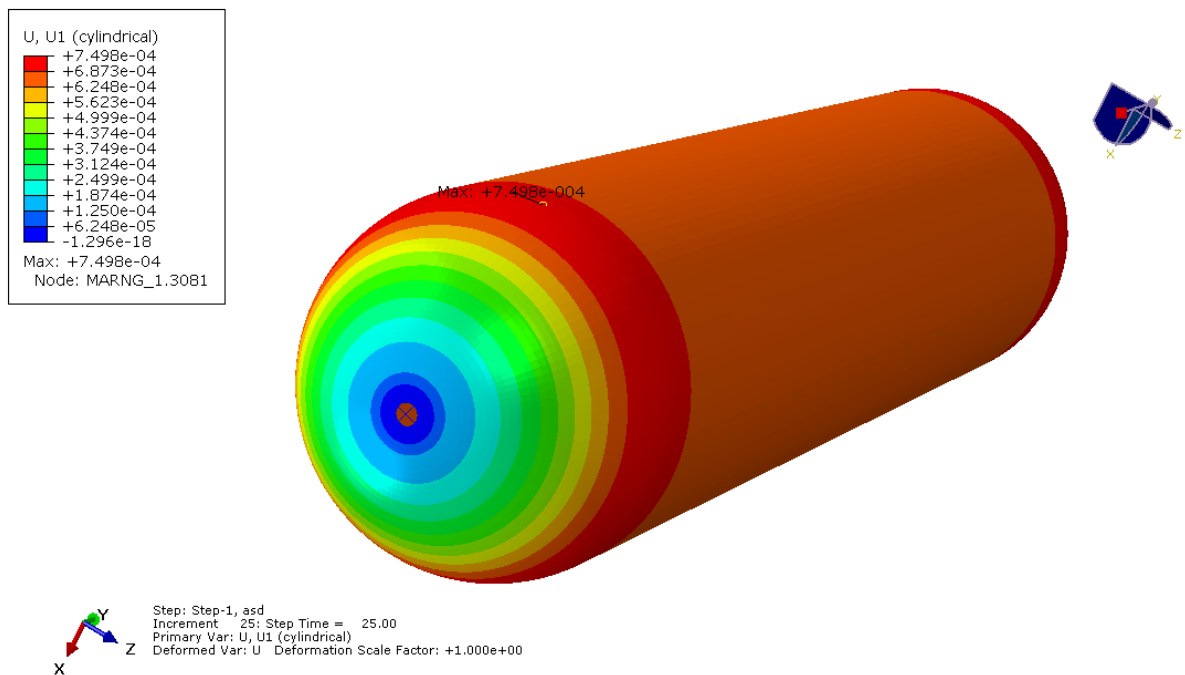


**Figure 5-6** The distribution of radial displacement at operating pressure (25 MPa) (m)

The maximum values of the axial and radial displacement were also calculated at the failure load (60 MPa). The maximum absolute value of the axial displacement is 1.57 mm and it is located at the polar boss opening region. It should be noted that the value is negative for the dome at the positive direction of the Z-axis. This means that this regions moves toward the middle of the cylinder (the starting point of the coordinate system). The distribution of the axial displacement at 60 MPa and the minimum value (maximum absolute value) are shown in Figure 5-7. As for the radial displacement, its maximum value is 2.69

mm and it is located at the dome-cylinder intersection region. The distribution of the radial displacement at 60 MPa is shown in Figure 5-8.

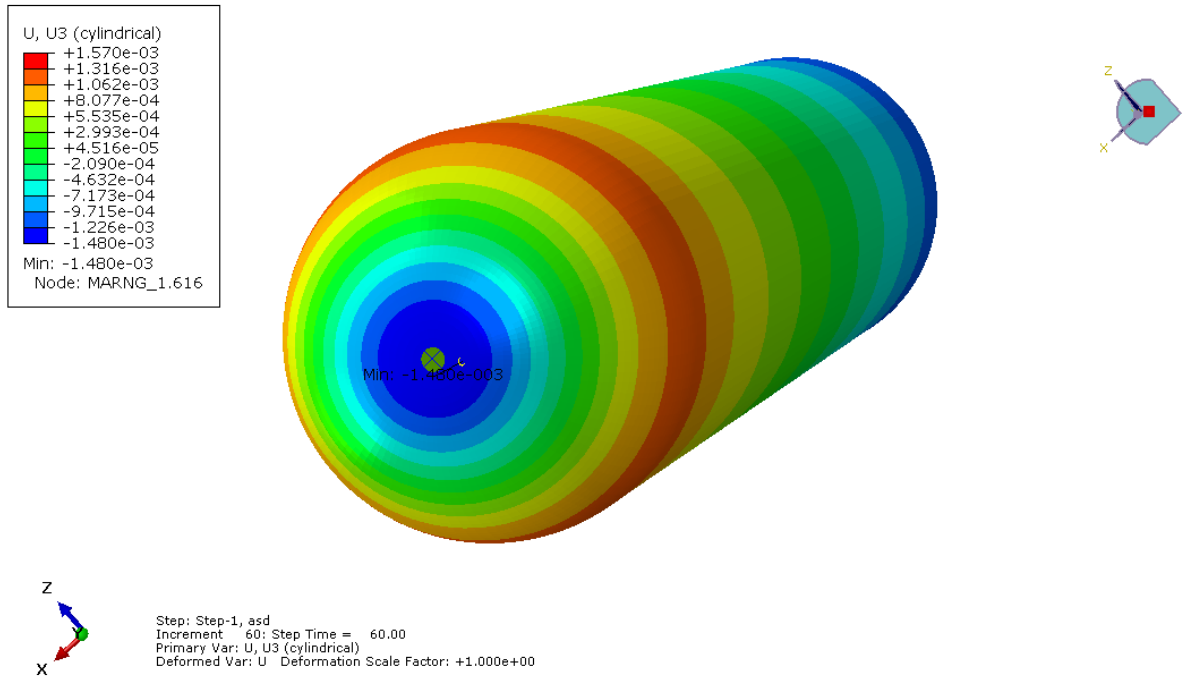


Figure 5-7 The distribution of axial displacement at the failure load (60 MPa) (m)

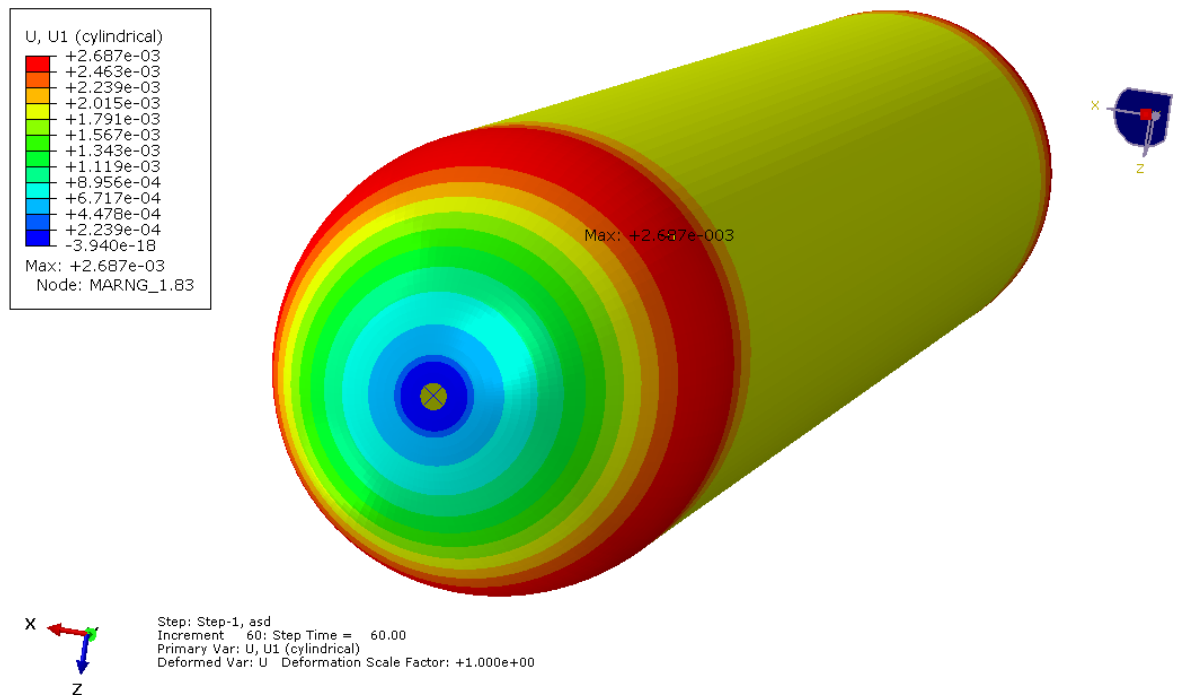


Figure 5-8 The distribution of radial displacement at the failure load (60 MPa) (m)

## 5.2 Parametric Study

The initial model complies with the regulations as its safety factor (2.4) exceeds the required value (2.25). However, a parametric study was conducted to determine which parameters of the design affect the ability of the pressure vessel to withstand the required internal pressure without failure and to quantify the importance of their effect.

Three parameters were chosen to be checked. The first parameter is the percentage of the thickness of the composite covered by helical layers. The initial model had a total of 21mm thickness of helical layers, with its total thickness being 30mm. Thus, 70% of the thickness consisted of helical layers and the rest 30% of hoop layers. In order to have comparable results, the thickness of the liner (6mm) and the total thickness of the composite (30mm) were kept constant. The three helical/hoop thickness ratios that were checked and compared to the initial ratio of 70/30 were 10/90, 30/70 and 50/50. Unfortunately, due to the increasing thickness of helical layers in the dome region, it was unable to check ratios greater than 70/30 as the construction at those were too thick (greater than 70mm).

The next parameter, which was checked, was the thickness of the liner. The models with the four different helical/hoop thickness ratios were recreated with different thickness of liner. Each model was recreated with a thickness of liner of 4mm and with a thickness of 8mm, resulting in 8 new models.

Finally, the last parameter, which was checked, was the shape of the domes. The four models with the liner with 6mm thickness were recreated with elliptical shaped domes. The minor to major axis ratio was chosen to be 0.7, as the analysis of Katsaounis and Tsouvalis (2014) had shown that this is the optimum choice for domes with constant thickness.

### 5.2.1 The impact of the helical/hoop layer thickness ratio on the strength of the pressure vessel

The impact of the ratio of thickness of helical layers to thickness of hoop layers on the strength of the construction was examined. The four different cases, that were examined, had ratios of 70/30, 50/50, 30/70 and 10/90 respectively. This was made by changing the number of helical and hoop layers. The initial model (70/30) had 7 helical layers and 3 hoop layers with a thickness of 3mm each. The 50/50 model was created with 5 helical layers and 5 hoop layers with 3mm thickness each. The other two model were created with respective way.

The quantities that were compared were the load of failure, the maximum value of von Mises or Tsai-Wu index at the load of failure (if the pressure vessel failed due to the fracture of the liner, then the maximum value of Tsai-Wu index was calculated and if the pressure vessel failed due to the fracture of a composite layer, then the maximum von Mises stress was calculated), the maximum axial displacement at this load and the radial displacement at the same load. The reason of failure was also determined (fracture of the liner or fracture of a composite layer) and the locations where the maximum values of von Mises stress and Tsai-Wu index were located.

The analysis showed that all four pressure vessels failed due to fracture of the liner. The impact of the thickness of helical layers is important as the decrease of the percentage of the helical thickness in the total thickness of composite resulted in a decrease of the maximum load that the pressure vessel is able to withstand.

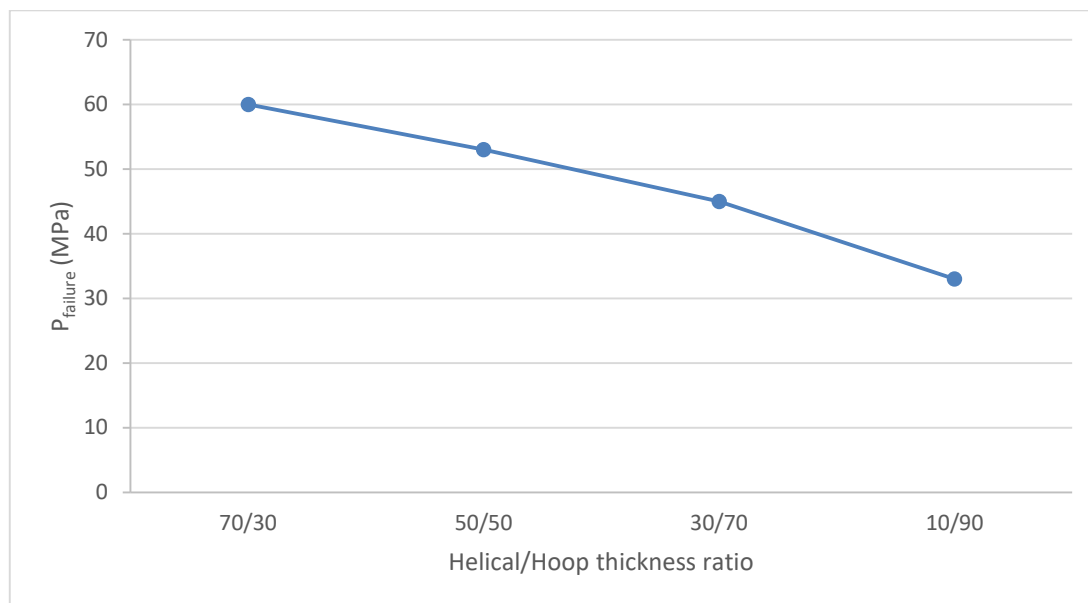


**Figure 5-9** The relation of the load of failure with the helical/hoop thickness ratio

**Table 5-4** The results of the analysis for the helical/hoop thickness ratio

Model #	Helical/hoop	$P_{failure}$ (MPa)	Reason of failure	Tsai- Wu at failure	Position	
					von Mises	Tsai-Wu
1	70/30	60	von Mises	0.8406	boss hole	1st hoop layer (dome-cylinder intersection)
2	50/50	53	von Mises	0.562	boss hole	3rd hoop layer (dome-cylinder intersection)
3	30/70	45	von Mises	0.4398	boss hole	1st hoop layer (dome-cylinder intersection)
4	10/90	33	von Mises	0.377	boss hole	1st hoop layer (dome-cylinder intersection)

As it is shown in Table 5-4, the reason of failure is common for all four models and the reduction of the helical/hoop ratio did not alter the location where the maximum von Mises stress is presented. However, the model with the balanced distribution of the composite thickness (50/50) behaved differently, thus the maximum value of the Tsai-Wu index was observed in the 3<sup>rd</sup> hoop layer of the 5 existing in total. As for the Tsai-Wu index at the failure load, its value decreases as the total thickness of helical layers decreases. This indicates that there is increased residual strength of the composite at the moment of failure, which is reasonable as the applied load is decreased.

The maximum values of the axial and radial displacement at the operating were also calculated. The values are summarized in Table 5-5. It is noted that the values are not directly comparable as they are calculated at different loads. Despite that, it is notable that the value of the axial displacement increases as the total thickness of the helical layers decreases. The same happens for the radial displacement as well, with the exception of the model with 50% helical and 50% hoop layers, which has slightly lower maximum radial displacement.



**Table 5-5 The maximum values of the axial and the radial displacement at the failure load**

Model #	Helical/hoop	P <sub>failure</sub> (MPa)	Displacement (mm)	
			Axial	Radial
1	70/30	60	1.57	2.69
2	50/50	53	1.60	2.65
3	30/70	45	2.17	3.30
4	10/90	33	3.24	3.99

In order to have comparable values, the maximum value of the axial and radial displacement were also calculated at the operating pressure (25MPa). The maximum values and their percentage change relative to the values of the 70/30 combination are presented in Table 5-6. It is obvious that the decrease of the helical/hoop thickness ratio resulted in a significant increase of the axial displacement. On the other hand, the change of the radial displacement is insignificant for the 50/50 combination and a lot lower for the 30/70 and 10/90 combinations.

**Table 5-6 The maximum absolute values of axial and radial displacement at operating pressure and their percentage change**

Helical /hoop	Displacement (mm)		Change (%)	
	Axial	Radial	Axial	Radial
70/30	0.41	0.75	-	-
50/50	0.67	0.77	63.5%	2.7%
30/70	1.05	0.96	158.1%	27.7%
10/90	2.18	1.96	435.9%	161.3%

All in all, it can be concluded that the initial model, whose composite thickness is derived by 70% helical layers and 30% hoop layers has greater strength than the other combinations and the decrease of the quantity of helical layers results in a decrease of the strength of the pressure vessel and its stiffness. Therefore, the 70/30 combination is preferable, as the other combinations demand increased thickness of liner or composite in order to comply with the regulations.

### 5.2.2 The impact of the liner thickness on the strength of the pressure vessel

The next parameter of the design, that its impact on the strength of the vessel was checked, is the thickness of the liner. The four models created in section 5.2.1 were used to create 4 new models with liner thickness 4mm and another 4 models with 8mm thickness of liner. It was obvious that the increase of the thickness of the liner would result in an increased load of failure and respectively the decrease of the liner thickness would result in a decreased load of failure. However, the purpose of this analysis was to quantify this change and to determine the importance of this parameter in the design.

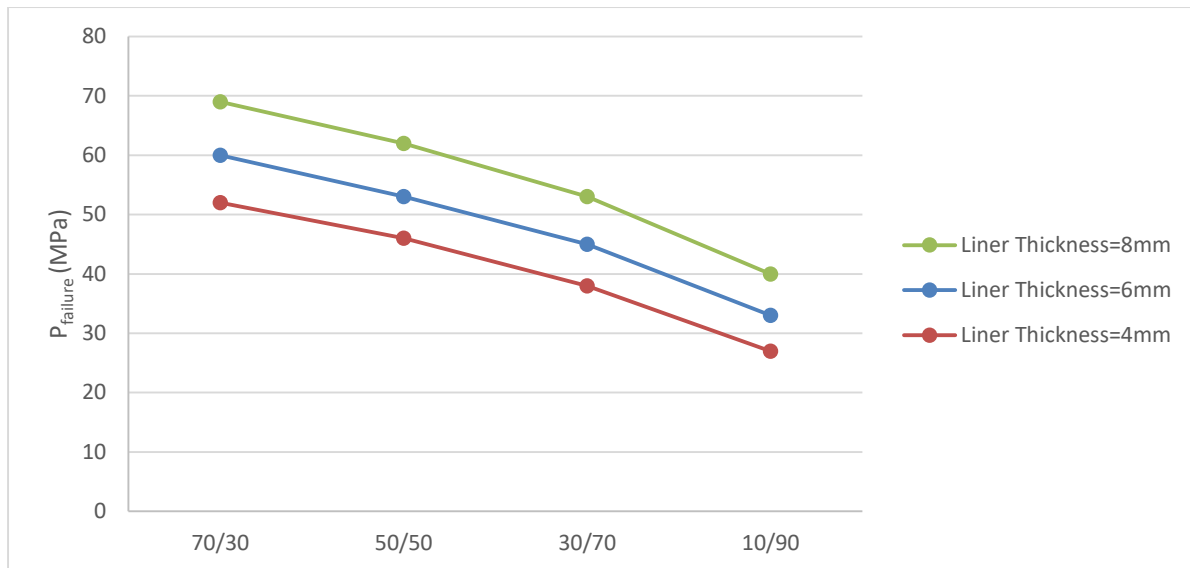


**Figure 5-10 The failure load vs helical/hoop thickness ratio for different liner thicknesses**

As it was expected, the increase of the thickness of the liner results in an increase of the strength of the pressure vessel. In particular, as it is shown in Figure 5-10, the 33% increase of the liner thickness resulted in an increase between 15% and 21.2% of the failure load of the pressure vessel. This change is a 15% increase for the 70/30 combination and a 21.2% for the 10/90 combination. The increase for the other two combinations is in between these two limits. The greater impact on the failure load of the 10/90 combination is justified by the fact that for this combination the thickness at the dome regions is lower, thus the strength of the liner at this region has greater importance. Respectively, the 33% (from 6mm to 4mm) decrease in liner thickness resulted in a decrease of the failure load from 13.3% (for 70/30) up to 18.2% (for 10/90).

It should be noted that the reason of failure remains the fracture of the liner and the failure in every case is located in the region near to the polar boss opening. In addition, the maximum value of the Tsai-Wu index at the failure load is located at the 1<sup>st</sup> hoop layer at the dome-cylinder intersection in every case. Therefore, it can be concluded that the change of the thickness of the liner did not change either the reason of failure or the region of the composite reinforcement which is more prone to failure. The maximum values of the Tsai-Wu index in every case are summarized in Table 5-7.

**Table 5-7 The maximum Tsai-Wu index in every examined case**

Helical /hoop	Maximum Tsai-Wu index		
	$t_{\text{liner}}=4\text{mm}$	$t_{\text{liner}}=6\text{mm}$	$t_{\text{liner}}=8\text{mm}$
70/30	0.7087	0.8406	0.9593
50/50	0.4469	0.4034	0.5702
30/70	0.3852	0.4398	0.4764
10/90	0.3684	0.3770	0.4002

The results show that the increase of the thickness of the liner results in an increase of the maximum value of Tsai-Wu index. This can be explained by the fact that the failure load increases, thus the developed stresses in the composite are greater.

Finally, the maximum axial and radial displacement at the operating pressure were calculated. The results are shown in Table 5-8 and Table 5-9 respectively.

**Table 5-8 The maximum axial displacement at the operating pressure in every examined case**

Helical /hoop	Maximum Axial Displacement (mm)		
	$t_{\text{liner}}=4\text{mm}$	$t_{\text{liner}}=6\text{mm}$	$t_{\text{liner}}=8\text{mm}$
70/30	0.45	0.41	0.37
50/50	0.76	0.67	0.60
30/70	1.28	1.05	0.93
10/90	2.92	2.18	1.63

**Table 5-9 The maximum radial displacement at the operating pressure in every case examined case**

Helical /hoop	Maximum Radial Displacement (mm)		
	$t_{\text{liner}}=4\text{mm}$	$t_{\text{liner}}=6\text{mm}$	$t_{\text{liner}}=8\text{mm}$
70/30	0.92	0.75	0.64
50/50	1.06	0.77	0.63
30/70	1.72	0.96	0.70
10/90	4.01	1.96	0.75

As it was expected, the increase of the liner thickness decreases the axial and radial displacements at the same load. It is notable that the radial displacement of the pressure vessels with liner thickness 8 mm increases slightly with the decrease of the helical/hoop thickness ratio. This indicates that the increase of the thickness of the liner increased the stiffness of the pressure vessel. It should be noted that the displacements are affected by the mechanical behavior of the liner, thus the displacements are greater for pressure vessels whose liner has entered the plasticity zone at the operating pressure. These pressure vessels are the 10/90 with liner thickness 6mm and the 10/90 and 30/70 with liner thickness equal to 4mm. The percentage change of the displacements compared to the displacements of the pressure vessels which have thickness of liner equal to is shown inTable 5-10.

**Table 5-10 Percentage change of the displacements compared to the displacements of the pressure vessel with liner thickness equal to 6mm**

Helical /hoop	$t_{\text{liner}}=4\text{mm}$		$t_{\text{liner}}=8\text{mm}$	
	Axial	Radial	Axial	Radial
70/30	33.7%	104.8%	-25.1%	-61.5%
50/50	21.9%	79.9%	-11.9%	-27.0%
30/70	13.5%	37.5%	-9.5%	-18.3%
10/90	11.1%	22.4%	-8.8%	-14.6%

In conclusion, the change of the thickness of liner resulted in an expected change of the strength and the stiffness of the construction. However, the 70/30 combination remains the combination with greater strength and stiffness.

### 5.2.3 The impact of the dome shape on the strength and stiffness of the pressure vessel

Another parameter, which was checked, was the shape of the dome. The shape that was chosen to be compared to the spherical domes of the initial geometry, was the elliptical shape with axis ratio equal to 0.7. Therefore, the minor axis of the dome has a length of 157.5mm, as the major axis is the radius of the cylinder, whose length is 225mm.

The analysis was based on the four models created in section 5.2.1, which were recreated with elliptical shaped domes. The first step of the analysis was to determine the failure load and to compare it with the failure load of the respective model with spherical model. The failure load of the models with elliptical domes and the models with spherical domes are shown in Figure 5-11.

The reason of failure of all the four models with elliptical domes was the failure of the liner at a region near to the polar boss opening. Therefore, the reason and the location of failure did not change with the change of the shape.

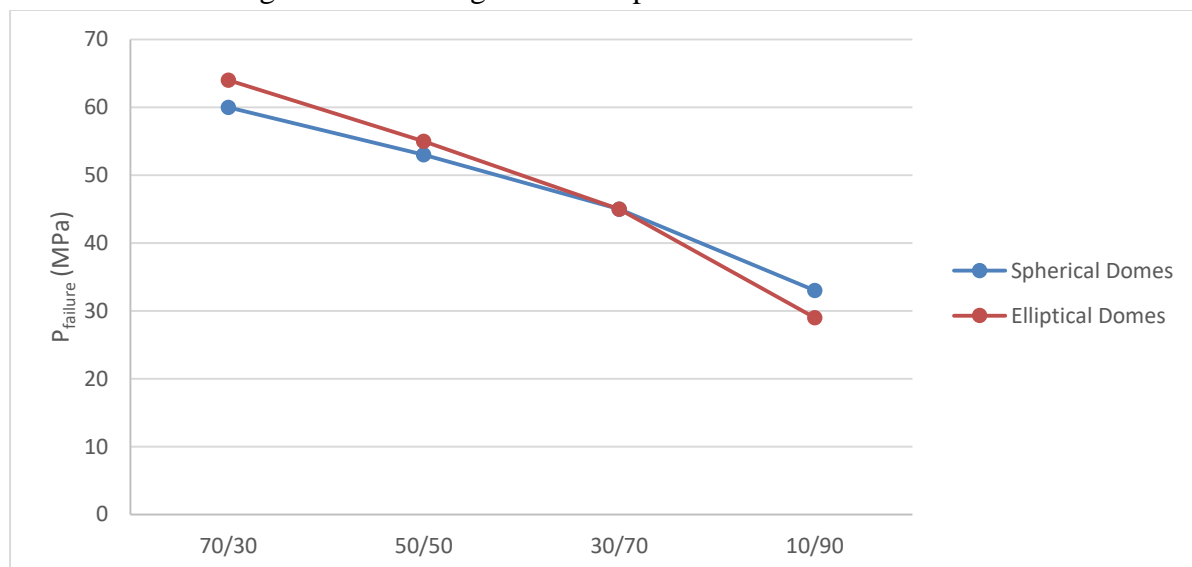


**Figure 5-11 The failure load vs the helical/hoop ratio of pressure vessels with spherical or elliptical domes**

As it shown in Figure 5-11, the change of the shape of the domes resulted in a slight increase of the failure load of the 70/30 and 50/50 combinations. This increase is 6.25% and 3.64% respectively. On the other hand, the change of the shape did not bring any change in the strength of the pressure vessel with the 30/70 combination and even decreased 13.8% the failure load of the 10/90 combination. In general, the behaviour did not change as the decrease of the helical/hoop thickness ratio results in a lower failure load.

As for the Tsai-Wu index at the failure load, the change of the dome shape changed its behaviour. As it was described in section 5.2.1, the maximum value of the index for the pressure vessels with spherical domes was located in the hoop layers at the dome cylinder-intersection. However, for the pressure vessels with elliptical domes, the maximum value of the Tsai-Wu index is located in the first helical layer at the polar boss opening region for the 50/50, 30/70 and 10/90 combinations. As for the 70/30 combination, the maximum value of

the Tsai-Wu index is located at the middle region of all the three hoop layers. The Table 5-11 contains these values and their location.

**Table 5-11 The maximum values and locations of Tsai-Wu index for pressure vessels with spherical and elliptical domes**

Helical /hoop ratio	Maximum Tsai-Wu index		Location	
	Spherical Domes	Elliptical Domes	Spherical Domes	Elliptical Domes
70/30	0.8406	0.5418	1 <sup>st</sup> hoop (dome-cylinder intersection)	All hoop layers (middle)
50/50	0.4034	0.1556	3 <sup>rd</sup> hoop (dome-cylinder intersection)	1 <sup>st</sup> helical (boss hole)
30/70	0.4398	0.2007	1 <sup>st</sup> hoop (dome-cylinder intersection)	1 <sup>st</sup> helical (boss hole)
10/90	0.377	0.2424	1 <sup>st</sup> hoop (dome-cylinder intersection)	1 <sup>st</sup> helical (boss hole)

It can be noticed that the maximum values of the Tsai-Wu index at the failure load was decreased with the change of dome shape. The difference in the load that these values were calculated is relatively small, so they can be comparable. Although the Tsai-Wu index of the combination 30/70 was calculated at the same failure load, the maximum value of the Tsai-Wu index was decreased significantly. This indicates that the change of the dome shape decreased significantly the developed stresses in the composite, thus the residual strength of the composite reinforcement is greater.

As for the displacements, the change of the dome shape altered the distribution of both the axial and radial displacements. The distribution of the axial displacements looks like the respective distribution of pressure vessels with spherical domes with the exception that the boss hole region does not move toward the middle of the cylinder, but it remains almost motionless. In addition, the maximum value of the axial displacement is located at the same region, which is the dome-cylinder intersection. The distribution of the axial displacements of the 70/30 combination is shown in Figure 5-12. On the other hand, the distribution of the radial displacements is completely different. Its maximum values are located at the whole cylindrical portion with a slight peak at a location between the middle of the cylinder and the dome-cylinder intersection. The distribution of the radial displacement of the 70/30 combination is depicted in Figure 5-13.

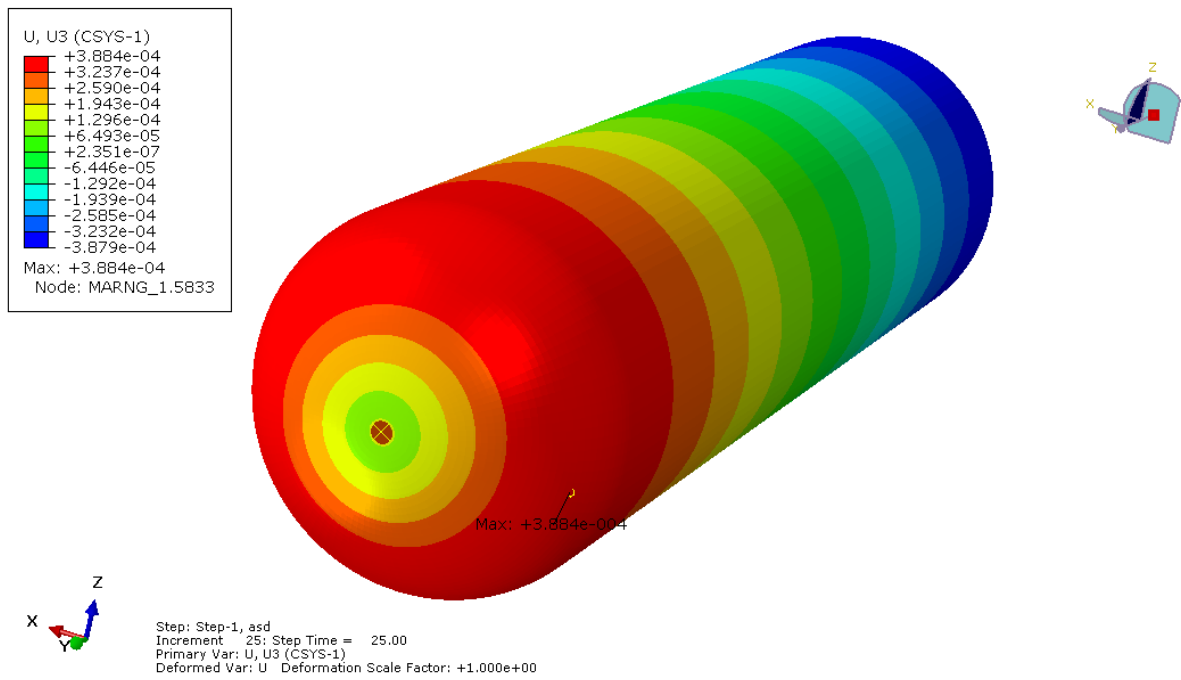


**Figure 5-12** The axial displacement of the 70/30 combination with elliptical domes at the operating pressure (25 MPa) (m)

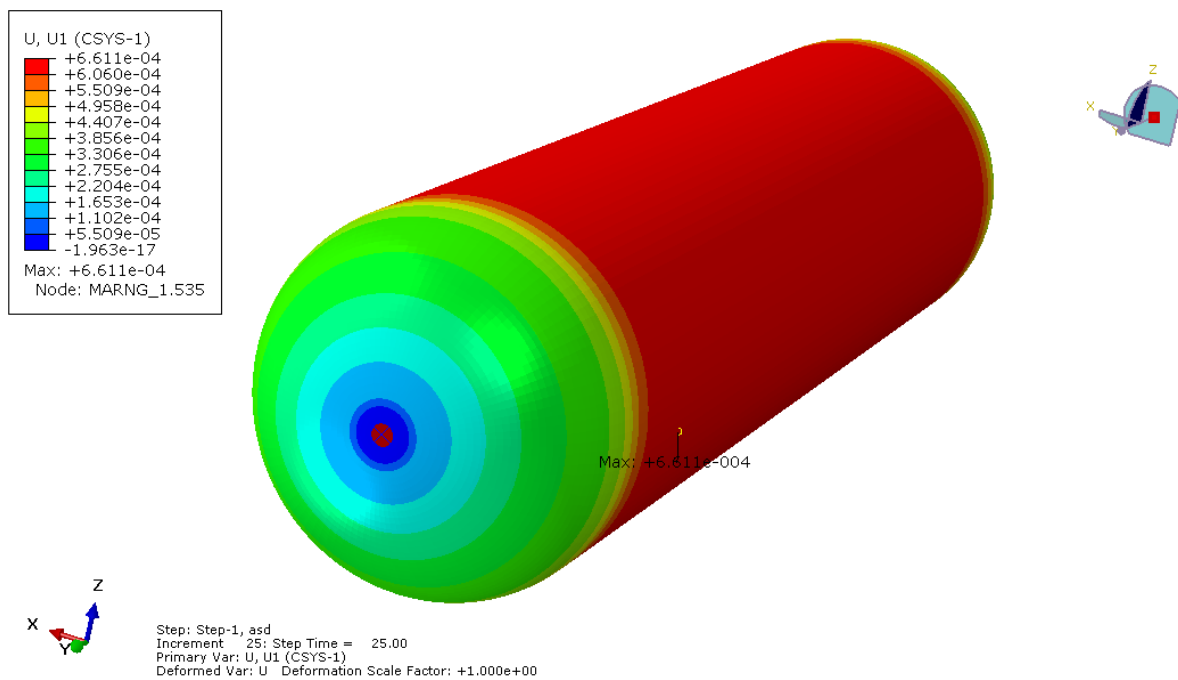


**Figure 5-13** The radial displacement of the 70/30 combination with elliptical domes at the operating pressure (25 MPa) (m)

The maximum values of all the four combinations are summarized in Table 5-12. It is notable that when the helical/hoop thickness ratio decreases the radial displacement decreases and the axial displacement increases for the pressure vessels with elliptical domes. This happens because the maximum value of the radial displacement is located at the cylindrical portion which becomes stiffer with the increase of the hoop layers. On the other hand, the

maximum value of the axial displacement is nearer to the dome which becomes less stiff, because the thickness of the dome (which is made exclusively by helical layers) decreases. Another noticeable fact is that the change of the shape of the dome did not alter significantly either the location or the maximum value of the axial displacement. In addition, although the change of the maximum value of the radial displacement of the 70/30 combination is relatively small, this change is becoming more and more important, as the helical/ hoop thickness ratio decreases, reaching up to a decrease of almost 4 times for the 10/90 combination.

**Table 5-12 The maximum values of axial and radial displacement for pressure vessel with spherical or helical domes at the operating pressure (25 MPa)**

Helical /hoop ratio	Axial Displacement (mm)		Radial Displacement (mm)	
	Spherical Domes	Elliptical Domes	Spherical Domes	Elliptical Domes
70/30	0.41	0.39	0.75	0.66
50/50	0.67	0.69	0.77	0.47
30/70	1.05	1.15	0.96	0.41
10/90	2.18	2.64	1.96	0.58

To summarize, the change of the dome shape resulted in greater strength for the combination in which the helical layers are more or equal to the hoop layer (70/30 and 50/50) and equal strength (30/70) or less strength (10/90) for the combination with more hoop layers. In addition, the pressure vessels with the 70/30 and 50/50 combinations comply with the regulations, as their failure load is greater than the demanded (56.25 MPa). Nonetheless, for all the four combinations, the change of the dome shape did not significantly change the maximum values of the axial displacement, but the respective change of the radial displacement was important.

### 5.3 Definition of the total thickness of the composite reinforcement

In order to define the final design, the total thickness of the composite reinforcement must be decided. Its selection is based on the design principle that the construction must be as light as possible. Therefore, the optimum thickness of composite is the minimum value with which the pressure vessel can withstand the demanded by the regulations pressure (56.25 MPa).

The parametric study that was carried out in 5.2 showed that the greatest strength of the pressure vessel is achieved with a combination of 70% helical layers and 30% hoop layers in any case (spherical or elliptical domes). Therefore, this is the only combination which was used for the following analysis. Although the aforementioned parametric study showed that for the 70/30 combination with thickness of liner equal to 6mm and total thickness of composite equal to 30mm, the elliptical domes are preferable, the spherical domes were not excluded from the analysis for the definition of the total thickness of composite needed, because the decrease of the total thickness of composite could result in different preference.

The procedure that was followed was to create new models in Abaqus, based on those which had been created in 5.2, with decreased thickness of composite and check their failure

load and the reason of failure for both pressure vessels with spherical domes and elliptical domes. The increment of the decrease of the thickness of the composite reinforcement of the pressure vessel was decided to be 4mm and the thickness of the liner was kept constant at 6 mm.

The analysis had another objective. This was to determine for what values of the total thickness of the composite, the composite reinforcement fails before the liner, because all the pressure vessels, which had been created in the previous analysis, had failed due to the fracture of the liner. For that reason, pressure vessels with composite reinforcement as thin as 6mm were created, in spite of the fact that they could not possibly comply with the regulations.

Firstly, 6 new models with spherical domes were created. Their failure load alongside the failure load of the initial pressure vessel with composite thickness equal to 30mm are shown in Figure 5-14. The analysis showed that only the pressure vessels with 26mm and 30mm thickness of composite can withstand the required pressure. Furthermore, both models failed due to the fracture of the liner. In addition, it is noticeable that the slope of the curve changes at a thickness equal to 26mm. This happens because the pressure vessels with thickness of composite under that value fail due to the fracture of the composite and not due to the failure of the liner as happens for pressure vessels with greater thickness. Finally, it can be concluded that pressure vessels with spherical domes need thickness of composite greater than 25mm, in order to comply with the regulations.

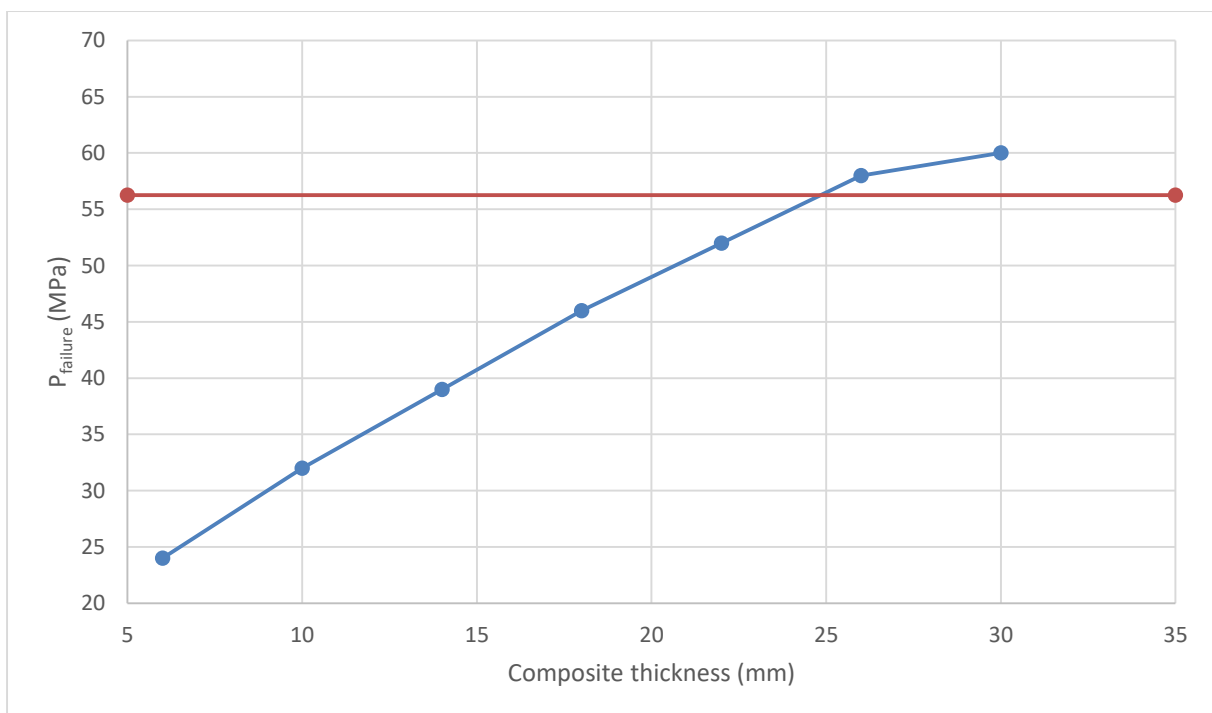


**Figure 5-14 Failure load vs thickness of composite for pressure vessels with spherical domes. The red line denotes pressure required by the regulations (56.25MPa)**

On the other hand, the respective analysis for pressure vessels with elliptical domes produced different results. As it can be seen in Figure 5-15, only the pressure vessels with thickness of composite equal to 26mm or 30mm could withstand the required pressure (red



line) again. However, the required thickness in order to achieve compliance with the regulations is lower. In fact, according to the curve, pressure vessels with thickness equal to or greater than 24mm could possibly have the required strength. Furthermore, it should be noted that the pressure vessels with thickness of composite equal or lower than 14 mm were all the three of them failed due to fracture of composite before the fracture of the liner and this is the reason of the change of slope of the curve at that value of composite thickness.

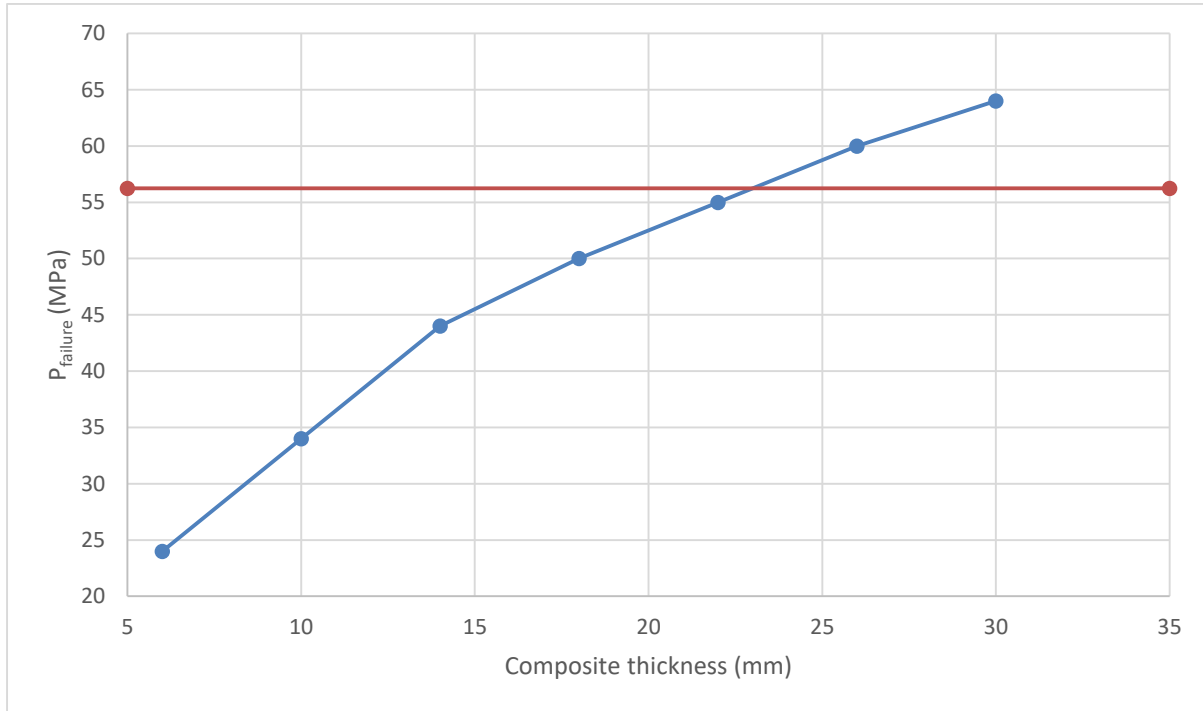


**Figure 5-15 Failure load vs thickness of composite for pressure vessels with elliptical domes. The red line denotes the required by the regulations pressure (56.25MPa)**

## 5.4 The final design

### 5.4.1 Description of the final design

The analysis carried out in 5.3 showed that the minimum value of the total composite thickness with which the pressure vessels complies with the regulation is 24mm. This is achieved for a pressure vessel with elliptical domes. The final design was based on this result.

The pressure vessel consists of an aluminium liner and a carbon fiber reinforcement. The aluminium liner consists of a cylindrical portion, with an internal length of 1500mm and an internal diameter equal to 450mm, and two elliptical domes (one at each end of the cylindrical portion) with a major axis equal to the radius of the cylinder (225mm) and a minor equal to 157.5mm. At the top of each dome, there is an opening with an internal diameter equal to 25.4mm.

The liner is covered with a carbon fiber reinforcement. The thickness of the composite is 24mm at the cylindrical portion, of which the 16.8mm are derived by helical layers and the rest 7.2mm by hoop layers. The domes are covered only with helical layers. The thickness of the composite reinforcement at the dome regions starts from 16.8mm and increases up to about 53mm at a region close to the polar boss opening. The total external length of the

pressure vessel is not included as it is depended on the increase of the composite thickness at the domes, but it is estimated to be about 1925mm.

The stacking sequence, which was used, consists of 7 balanced angle-ply helical layers with a thickness of 2.4mm per layer and winding angle 8deg, followed by 3 hoop layers with a thickness of 2.4mm per layer ( $[(\pm 8^\circ)_7/90^\circ_3]$ ).

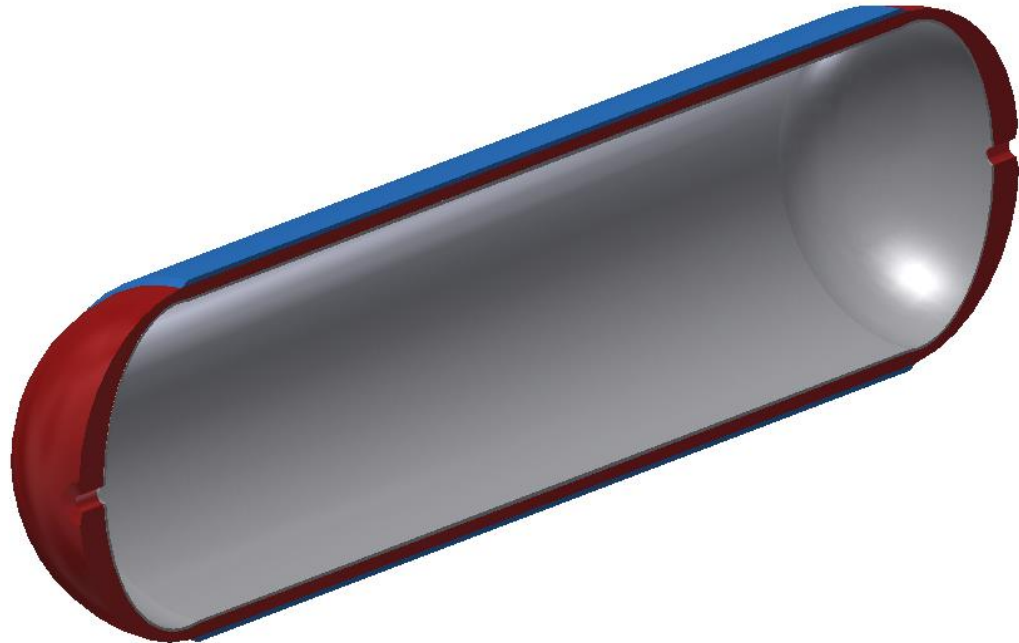


**Figure 5-16** Section view of a 3D modelling of the pressure vessel. The aluminium liner is coloured with grey, whereas the helical layers of the composite are red and the hoop layers are blue. ( $[(\pm 8^\circ)_7/90^\circ_3]$ )

#### 5.4.2 Results of the analysis at failure load

The first step of the analysis is to determine the reason of failure and the failure load. After the examination of the results, it was determined that the liner fractured at an internal pressure equal to 58MPa. The failure occurs at a region near to the polar boss opening. The distribution of the von Mises stress is shown in Figure 5-17. It is noted that the entire liner has stresses greater than the yield stress.

On the other hand, the Tsai-Wu index has not exceed the limit at that load. Its maximum value is observed in the hoop layers and it is 0.6973, thus the composite has not yet failed. The distribution of the Tsai-Wu index in the first hoop layer is shown in Figure 5-18. The values of the Tsai-Wu index are the same for the other two hoop layers. It is noted that the maximum value covers the biggest part of the cylindrical portion.

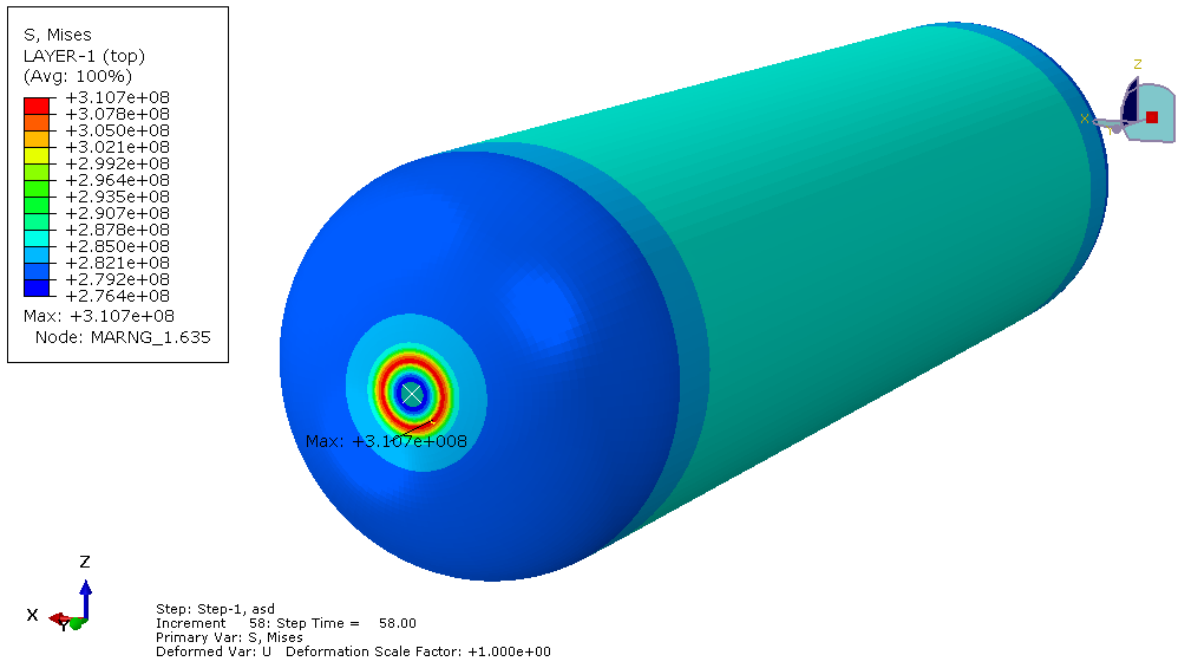


**Figure 5-17** The von Mises stress in the liner at the failure load (58MPa) .The location of the maximum stress is also denoted (Pa)

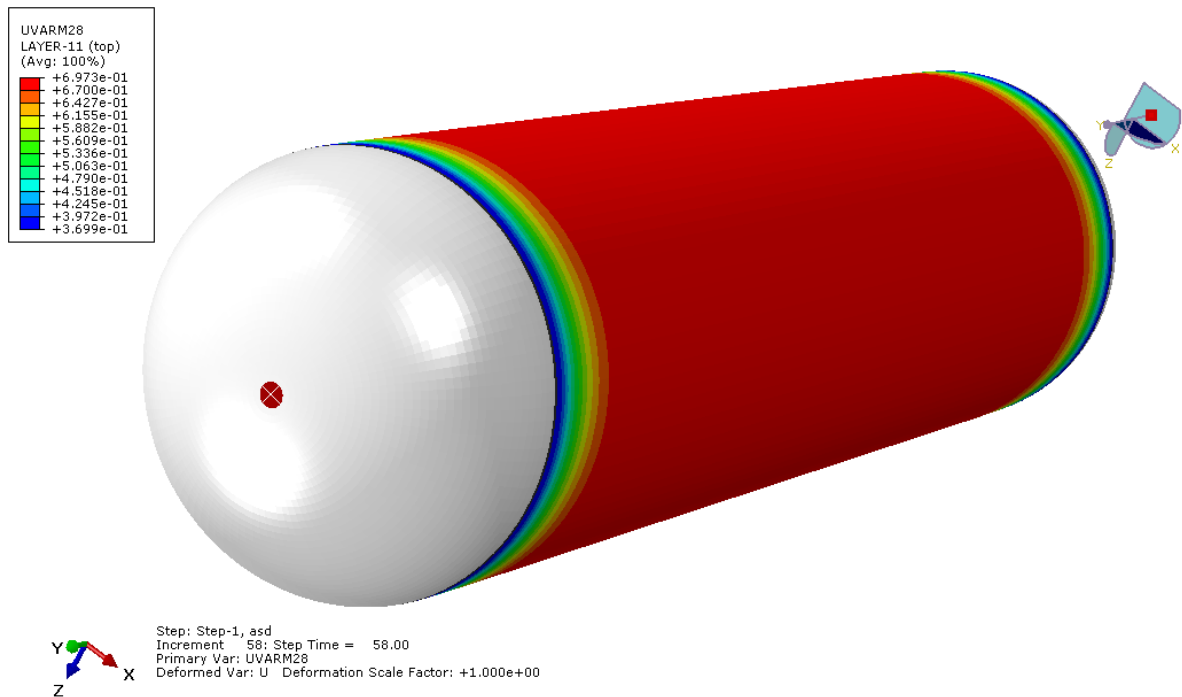


**Figure 5-18** Tsai-Wu index in the first hoop layer at 58MPa (failure load)

Firstly, from the comparison of the deformed with the undeformed shape (shown in Figure 5-19), it can be concluded that the pressure vessel does not deform uniformly. It seems that there is a less stiff region at the domes, whose great values of axial displacement change slightly the shape of the pressure vessel.

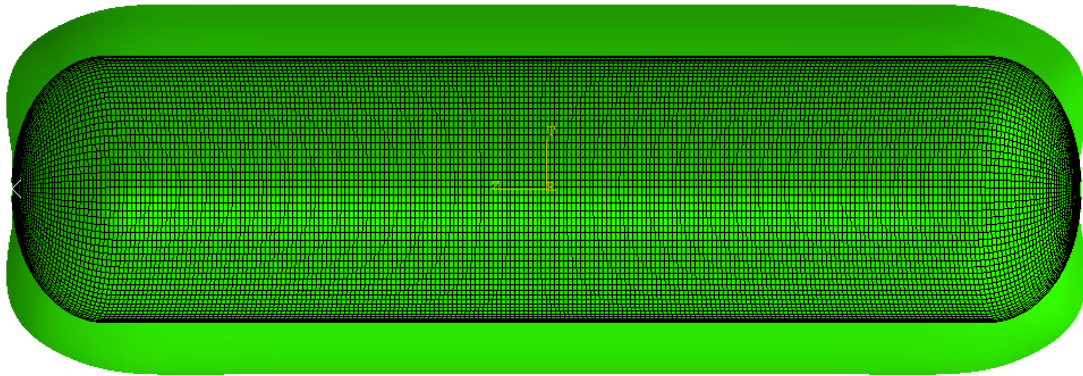


**Figure 5-19 Comparison of deformed (coloured) and undeformed (grid) shape of the pressure vessel at failure load (58MPa). The displacements of the deformed shape have been scaled 40 times in order to be distinct**

The analysis of the deformations of the pressure vessel can give an explanation of the developed stresses and the structural behaviour of the construction. Firstly, the displacements in the axial direction are presented in Figure 5-20. It is noted that the maximum value of axial displacement is at the region of the dome-cylinder intersection. This can be explained by the fact that the pressure applied at the elliptical shape of the dome has a direction closer to the axial direction. In addition, this region is less stiff than both the cylindrical part, as there is no thickness by hoop layers, and the rest of the dome, as the thickness of the dome increases along the meridian profile. It is also noted that the region near the polar boss opening remains almost still in the axial direction, as the axial displacement at that region is almost null. Another comment that should be made is that the axial displacements are symmetrical about the X-Z plane (middle of the cylindrical portion) with different sign due to the opposite direction of the movement, as expected due to the geometrical symmetry of the construction.

Furthermore, the radial displacements at the failure load were calculated and they are shown in Figure 5-21. The maximum value of the radial displacement is located at the biggest part of the cylindrical portion. This could explain also the distribution of the Tsai-Wu index in the hoop layers, as the hoop stresses, which derive by the radial displacements, are the dominant stresses of the Tsai-Wu index in the hoop layers. In addition, the radial displacements are null at the circle of the polar boss opening, as expected, due to the tie constraints (rigid links) that have been applied at this region.

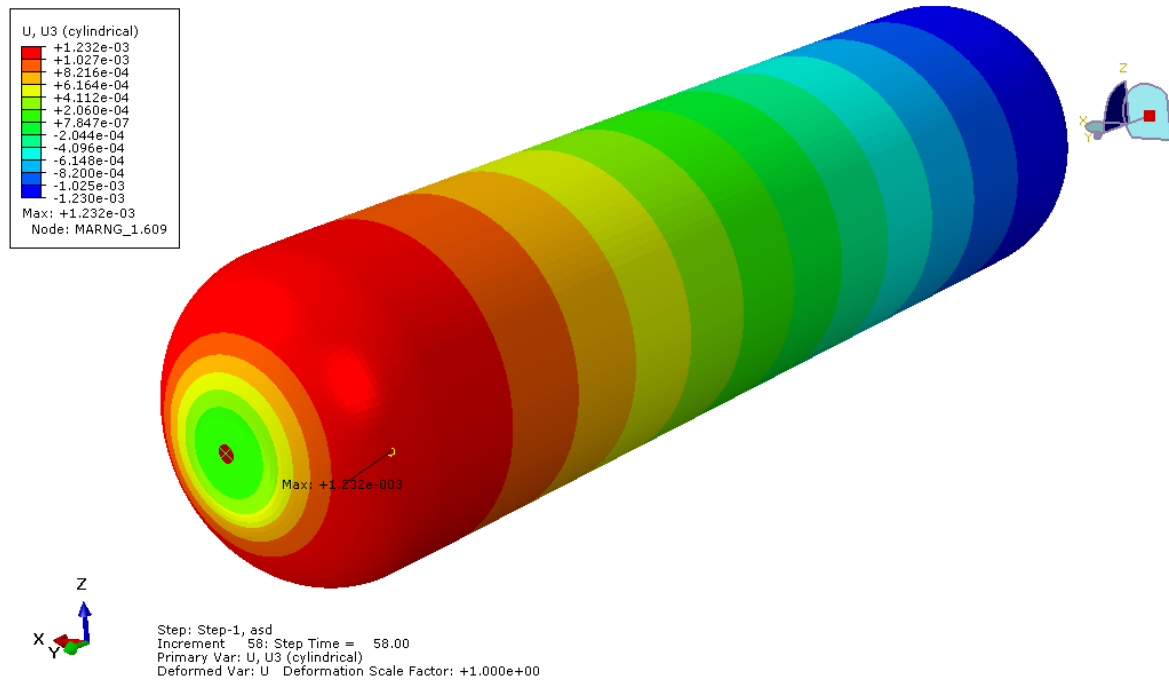


Figure 5-20 Axial displacement at the failure load (58MPa) (m)

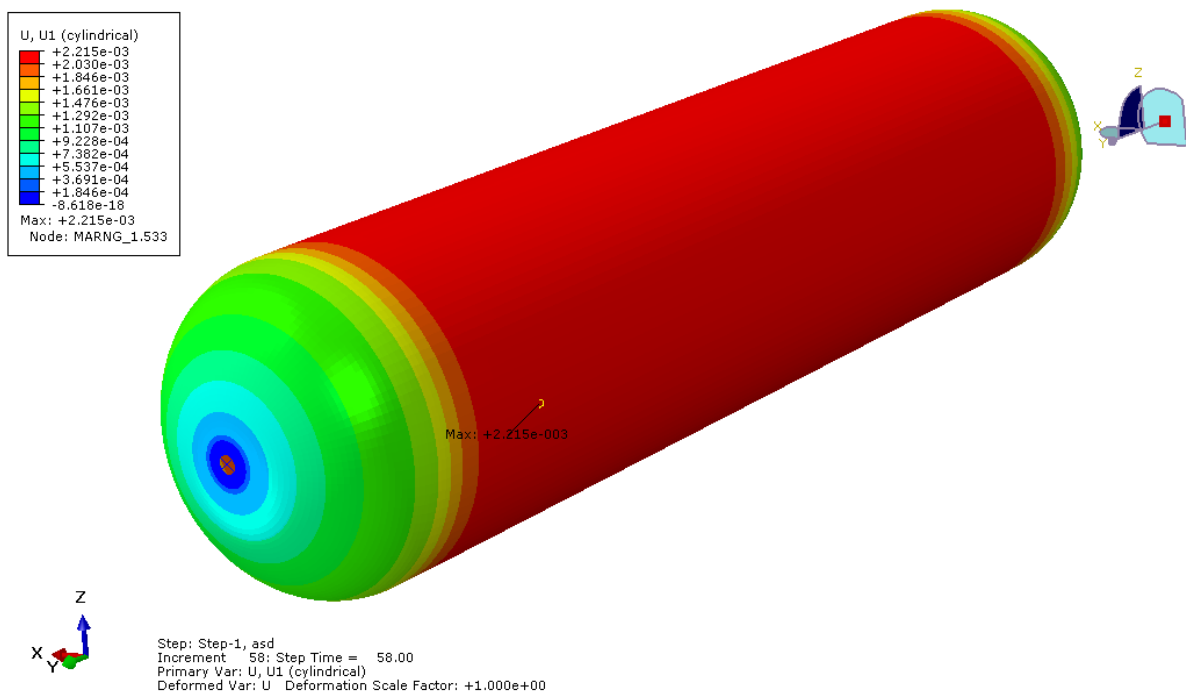


Figure 5-21 Radial displacement at the failure load (58MPa) (m)

### 5.4.3 Results of the analysis at the operating load (25 MPa)

The same analysis that was carried out at the failure load must be done to investigate the structural response of the pressure vessel at the operating pressure.

As shown in Figure 5-22, the von Mises stresses in the liner at the operating pressure are below the yield stress of the aluminium (276 MPa) for the biggest part of the pressure

vessel. However, at a region near to the polar boss opening, the stress slightly exceeds the yield stress. In addition, the maximum value of the stress occurs at the same position with the respective stress at the failure load.

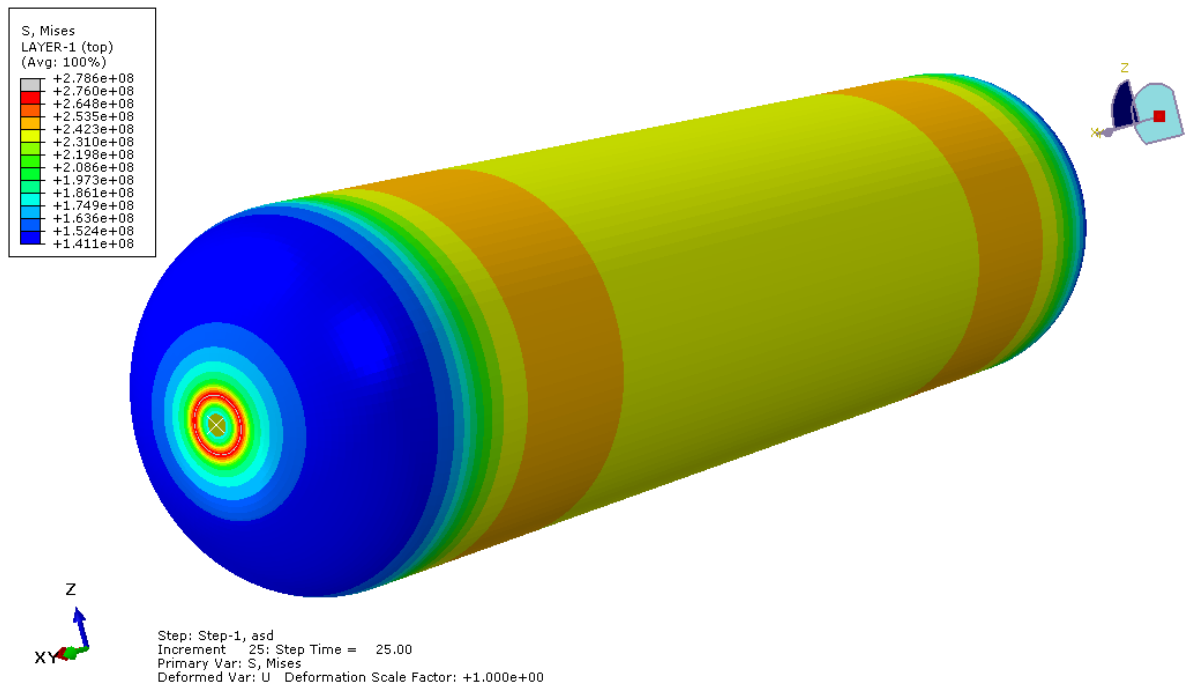


**Figure 5-22 Von Mises stress in liner at the operating pressure (25 MPa). The region where the von Mises stress is greater than the yield stress is depicted with grey colour. (Pa)**

The maximum value of Tsai-Wu index occurs again in the hoop layers and it has a similar distribution with that at the failure load. The maximum value is 0.0871, indicating that the residual stress for the composite is significant. The distribution can be explained again as the radial displacement is maximum at the same region with the Tsai-Wu index.

The deformed shape of the pressure at the operating pressure was also investigated. Figure 5-24 shows the comparison between the deformed and the undeformed shape of the pressure vessel at the operating pressure. It is noted that the cylindrical portion deforms uniformly and there is no local bending. A slight local bending can be seen at the edges of the cylindrical portion, because the radial displacements at the domes are lower as it will be presented later. It can also be noticed that the curvature of the dome changes, due to the increased axial displacements at the dome-cylinder intersection and the lower axial displacements at the polar boss opening region.

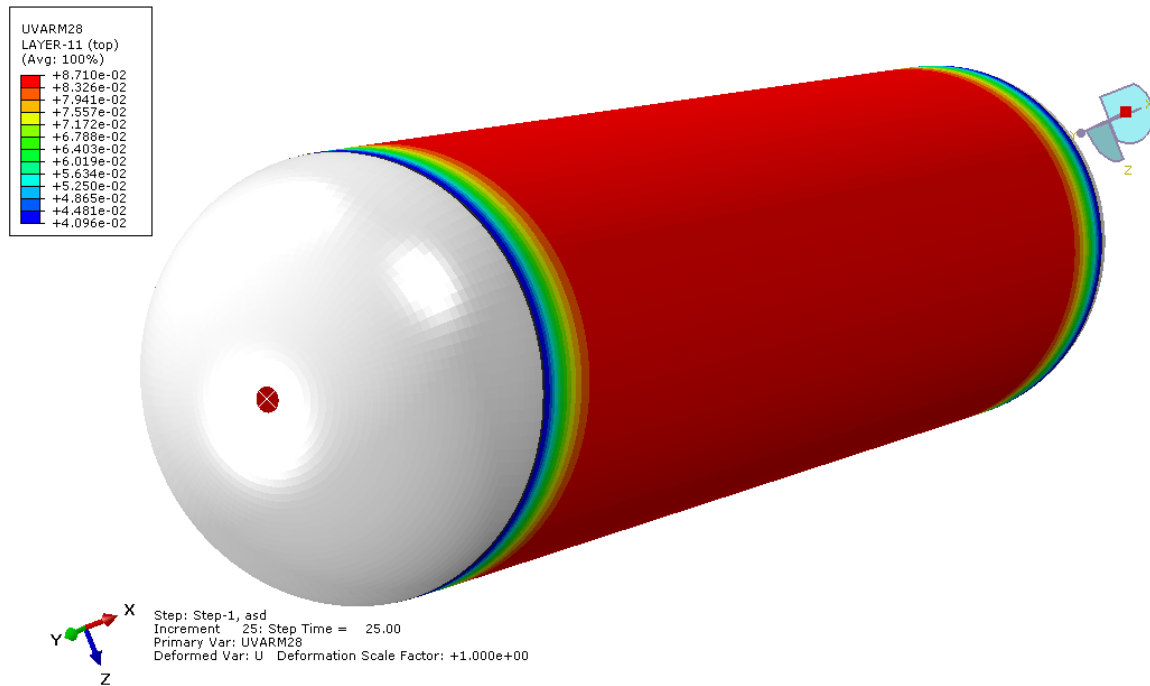


Figure 5-23 Tsai-Wu index in first hoop layer at the operating pressure (25 MPa)

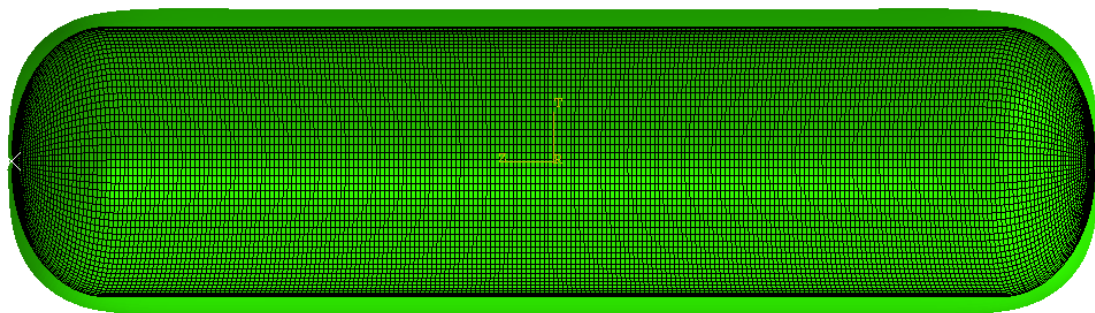


Figure 5-24 Comparison of deformed (coloured) and undeformed (grid) shape of the pressure vessel at the operating pressure. The displacements of the deformed shape have been scaled 40 times in order to be distinct

The axial displacements are shown in Figure 5-25. It is noted that the maximum value of the displacement is located at the same position with the maximum value of the axial displacement at the failure load. The displacements are again symmetrical about the X-Z plane with different sign due to the opposite direction of the movement of symmetrical nodes. A difference that should be noted is that the axial displacements at the polar boss region are not null at this load. As for the radial displacements, the distribution is exactly similar to that at the failure load. Its maximum value occurs again at the cylindrical part. It should be denoted that the displacements in the circumferential direction were also calculated and they were null, thus there is no coupling by the composite in that direction.

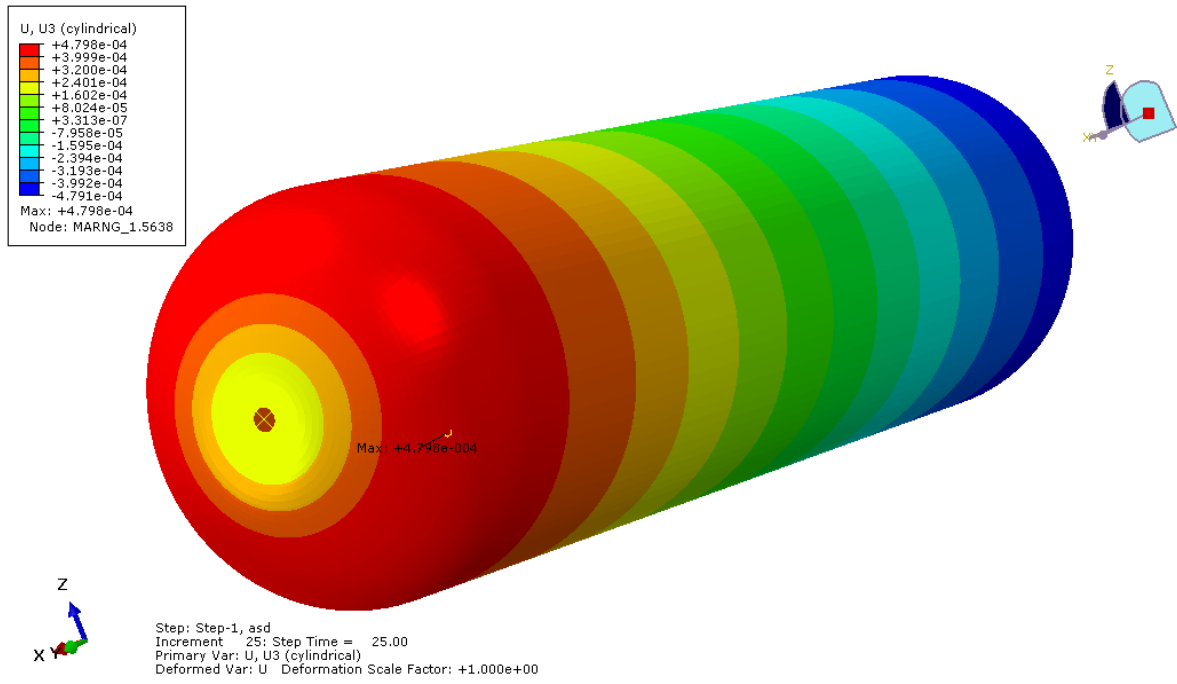


Figure 5-25 Axial displacement at the operating pressure (25 MPa) (m)

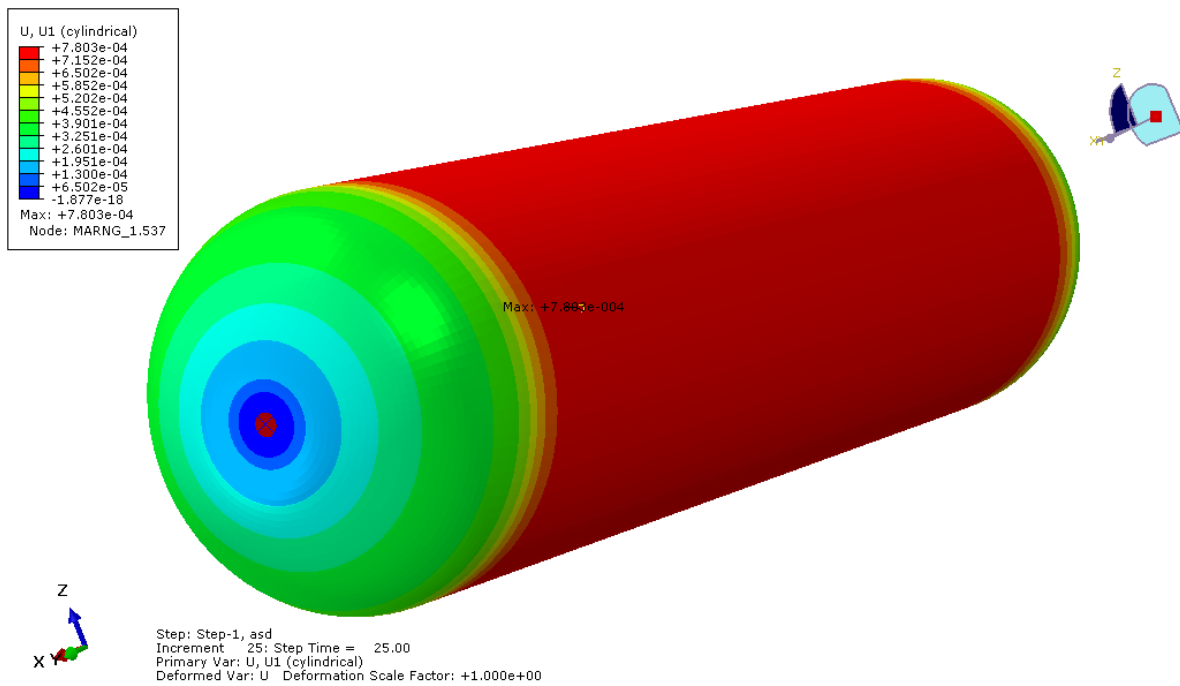


Figure 5-26 Radial displacement at the operating pressure (25MPa) (m)



## Chapter 6 Conclusions and Recommended Future Work

### 6.1 Conclusions

In the present section, certain conclusions of the thesis are summarized and highlighted. The section includes conclusions from both the process of the simulation model development and the simulation results.

- The parameters of non-geodesic winding are strongly correlated to the maximum static friction coefficient of the underlying surface. For the same turnaround radius (usually being the polar boss opening radius), the increase of the value of the coefficient from 0.2 to 0.5 resulted in an increase of the maximum safe initial winding angle in the region of 6deg. This conclusion can be reversed. Therefore, for the same initial winding angle, the increase of the maximum static friction coefficient would result in smaller turnaround radius. However, the change of the coefficient did not affect the general distribution of the winding angle along the dome, which remained almost constant for the biggest part of the dome with a steep increase near the turnaround region.
- The examination of the equation describing the winding angle distribution along the dome showed that the change of the radius of the dome do not affect the initial winding angle. The same examination (same turnaround radii and maximum static friction coefficient) was conducted for different radii of a spherical dome (0.15, 0.2 and 0.25m). The analysis showed that, in any case, the maximum safe initial winding angle was slightly decreased for increasing radius of dome. The change of the maximum safe initial winding angle between 0.15m and 0.25m did not exceed 2deg, so it can be assumed that the change of the dome radius do not affect significantly the winding trajectory.
- Likewise, the comparison of a spherical and an ellipsoidal dome with minor to major axis ratio equal to 0.7 showed that the change of the maximum safe initial winding angle was negligible as it did not exceed 0.5deg, in any case.
- The comparison of the results derived by FEM analysis of a dome with constant thickness and a dome with increasing thickness based on their stiffness showed that the building up thickness changed the structural response of the construction. In fact, the pressure vessel with the dome with increasing thickness had increased radial displacements in the cylindrical portion region and decreased displacements near the polar boss opening. Therefore, the increased thickness of the polar boss region decreased the displacements in the region and resulted in displacements at the regions, where the thickness was equal between the two models.
- A parametric study showed that the combination, in which 70% of the total thickness is helical windings and 30% of the total thickness is hoop windings, is the one that produces pressure vessels with the greatest burst pressure of all the rest of combinations available.

- It was also showed that the decrease of the liner thickness decreases linearly the ultimate strength of the pressure vessel for any combination of helical/hoop thickness ratio.
- The last comparison of the parametric study showed that pressure vessels with ellipsoidal dome with minor to major axis ratio equal to 0.7 have greater ultimate strength compared to pressure vessels with spherical domes for the 70/30 and 50/50 helical/hoop thickness combinations. This conclusion is not valid for the 30/70, where the ultimate strength is the same, and 10/90 combination, where the ultimate strength is lower.

## 6.2 Recommended future work

The final design could be the base for future work. Some proposals are listed below:

- The analysis could be more precise with the implementation of the aluminium liner as an independent part. The present study implemented the liner as the first layer of the construction. It is recommended to 3D design the liner in a CAD software and to import it in the Abaqus suite as an independent part. The composite reinforcement will be created again with the utilization of the Wound Composite Modeler without including the liner as a first layer. Then, a tie constraint could be applied in order to simulate the contact between the liner and the composite reinforcement.
- It would be interesting to investigate the validity of the results obtained during this thesis, by recreating the model with the use of continuum (solid) elements. During this thesis, the assumption that the thickness of the construction is relatively a lot smaller than the diameter of the cylinder, was made in order to approach the simulation with the use of the shell elements. Nonetheless, the shell underestimates the importance of certain quantities (like the transverse to element plane stress), which could alter the results.
- The manufacturing and the experimental testing in the existing experimental set-up of the Shipbuilding Technology Laboratory would also be an accurate method to validate the final design.
- A conclusion that was derived by the analysis is that the domes of the pressure vessels are lacking in stiffness near to the dome-cylinder intersection, especially when they are spherical shaped. The use of helical layers with different winding angles, which will not cover the entire surface of the dome in order to avoid slippage according to the theory discussed in Chapter 3, could reinforce this region and achieve, in that way, the decrease of the total composite thickness needed.
- Another parameter, whose impact on the structural response could be investigated, is the length of the cylindrical portion. In the present study, the length was kept constant in order to be fitted in a standard 20 feet container in the direction of the width. However, if its elongation is feasible, it could be fitted in the same container in the direction of the length. Filling, in this way, the volume

of the container with fewer independent pressure vessels, thus the investment cost could be decreased.

## References

- A.B.S. 2014a. Guide for propulsion and auxiliary systems for gas fuelled ships.
- A.B.S. 2014b. Guide for vessels intended to carry compressed natural gasses in bulk.
- Adamchak, F. & Adede, A. LNG as marine fuel. 17th International Conference & Exhibition on Liquefied Natural Gas (LNG 17), 2013 Houston.
- ASME BPVC Section X 2015. Boiler and Pressure Vessel Code: Section X-Fiber-Reinforced Plastic Pressure Vessels. ASME.
- Audi. 2013. *The Audi A3 Sportback g-tron* [Online]. Available: <https://www.audi-mediacentre.com/en/press-releases/the-audi-a3-sportback-g-tron-1862> [Accessed 18/8/2017].
- B&T Composites. Available: <http://www.btcomposites.gr/>.
- B.V. 2007. Classification of Compressed Natural Gas Carriers.
- B.V. 2011. Safety rules for gas-fuelled engine installations in ships.
- Bakar, R. A., Othman, M. F. & Ismail, A. R. The Compressed Natural Gas (CNG) Cylinder Pressure Storage Technology in Natural Gas Vehicles (NGV) Research Trends.
- Barboza Neto, E. S., Chludzinski, M., Roese, P. B., Fonseca, J. S. O., Amico, S. C. & Ferreira, C. A. 2011. Experimental and numerical analysis of a LLDPE/HDPE liner for a composite pressure vessel. *Polymer Testing*, 30, 693-700.
- Beukers, A., Koussios, S. & Bergsma, O. Composite pressure vessels design: integral determination of winding patterns. 16th International conference on composite materials, Kyoto, Japan, 2007.
- ClassNK 2016. Guidelines for gas fuelled ships (ver.4).
- Damen. 2014. *Damen, MTU and Svitzer will launch the world's first RSD CNG tug in 2016* [Online]. Available: [http://www.damen.com/en/news/2014/06/damen\\_mtu\\_and\\_svitzer\\_will\\_launch\\_the\\_worlds\\_first\\_rsd\\_cng\\_tug\\_in\\_2016](http://www.damen.com/en/news/2014/06/damen_mtu_and_svitzer_will_launch_the_worlds_first_rsd_cng_tug_in_2016) [Accessed 11/6/2017].
- De Carvalho, J., Lossie, M., Vandepitte, D. & Van Brussel, H. 1995. Optimization of filament-wound parts based on non-geodesic winding. *Composites Manufacturing*, 6, 79-84.
- dieselnet.com. *International: IMO Marine Engine Regulations* [Online]. Available: <https://www.dieselnet.com/standards/inter/imo.php>.
- Dillard, T. 2015. *CNG, METHANE, LP? THE METHA-CYCLE?* [Online]. Available: <https://evmc2.wordpress.com/2015/03/29/cng-methane-lp-the-metha-cycle/> [Accessed 18/8/2017].
- DNV-GL 2016. Rules for Classification of Ships.
- Einang, P. M. & Haavik, K. M. 2000. The Norwegian LNG Ferry. *NGV 2000 YOKOHAMA*.
- Evergreen. 2017. *Container Specifications* [Online]. Available: [http://www.evergreen-marine.com/tei1/jsp/TEI1\\_Containers.jsp#Dry\\_1](http://www.evergreen-marine.com/tei1/jsp/TEI1_Containers.jsp#Dry_1) [Accessed 26/6/2017].
- Funck, R. & Fuchs, H. 2001. Development of All-Composite Compressed Natural Gas (CNG) Pressure Vessel for Vehicle Use. *Proc. ICCM-13, Pekin*, 1-8.
- Gray, D. L. & Moser, D. J. 2004. Finite element analysis of a composite overwrapped pressure vessel. *American Institute of Aeronautics and Astronautics*, 6.
- HHP Insight. 2013. *CoCo-Afai CNG Ferry for Rio de Janeiro* [Online]. Available: <http://hhpinsight.com/marine/2013/11/coco-afai-cng-ferry-for-rio-de-janeiro/> [Accessed 11/6/2017].
- HHP Insight. 2014a. *CNG Ferry with ABC Engines & Solar Boost* [Online]. Available: <http://hhpinsight.com/marine/2014/06/cng-ferry-with-solar-boosted-abcs/> [Accessed 13/6/2017].

- HHP Insight. 2014b. *First Ferry for Rio Launched in China* [Online]. Available: <http://hhpinsight.com/marine/2014/08/first-ferry-for-rio-launched-in-china/> [Accessed 11/6/2017].
- HHP Insight. 2015. *CNG Net for Europe's First CNG Ferry* [Online]. Available: <http://hhpinsight.com/marine/2015/02/cng-net-for-europes-first-cng-ferry/> [Accessed 13/6/2017].
- I.M.O. 1973. International Convention for the Prevention of Pollution from Ships, 1973.
- I.M.O. 2014. *New Code of Safety for Ships using Gases or other Low flashpoint Fuels (IGF Code) agreed in draft form by IMO Sub-Committee* [Online]. Available: <http://www.imo.org/en/MediaCentre/PressBriefings/Pages/28-CCC1IGF.aspx#.VrIOofl97IU>.
- Johansen, B. S., Lystrup, A. & Jensen, M. T. 1998. CADPATH: a complete program for the CAD-, CAE- and CAM-winding of advanced fibre composites. *Journal of Materials Processing Technology*, 77, 194-200.
- Kabir, M. Z. 2000. Finite element analysis of composite pressure vessels with a load sharing metallic liner. *Composite Structures*, 49, 247-255.
- Katsaounis, G. & Tsouvalis, N. 2014. Deliverable 3.1 for "Compressed Liquid Tank (5000 psi and 1000 psi) Manufactured by composite materials (carbon fibers and epoxy resins)" Project
- Khan, M. I., Yasmin, T. & Shakoor, A. 2015. Technical overview of compressed natural gas (CNG) as a transportation fuel. *Renewable and Sustainable Energy Reviews*, 51, 785-797.
- Kim, C.-U., Hong, C.-S., Kim, C.-G. & Kim, J.-Y. 2005a. Optimal design of filament wound type 3 tanks under internal pressure using a modified genetic algorithm. *Composite Structures*, 71, 16-25.
- Kim, C.-U., Kang, J.-H., Hong, C.-S. & Kim, C.-G. 2005b. Optimal design of filament wound structures under internal pressure based on the semi-geodesic path algorithm. *Composite Structures*, 67, 443-452.
- Konstantinidis, G. 2016. *Material characterization of filament wound composite materials*. Diploma Thesis, National Technical University of Athens.
- Koussios, S. 2004. *Filament Winding. A Unified Approach*. Doctoral Thesis, TUDelft.
- Koussios, S. Design of cylindrical composite pressure vessels: Integral optimisation. 17th International Conference on Composite Materials, 2009.
- Koussios, S. 2011. Integral Design for Filament Winding—Materials, Winding Patterns, and Roving Dimensions for Optimal Pressure Vessels (Chapter 3). In: PETERS, S. T. (ed.) *Composite Filament Winding*.
- Koussios, S. & Bergsma, O. K. 2006. Friction Experiments for Filament Winding Applications. *Journal of Thermoplastic Composite Materials*, 19, 5-34.
- Koussios, S., Beukers, A. & Stathis, P. 2007. *Manufacturability of composite pressure vessels: Application of non-geodesic winding*.
- Kumar, S., Kwon, H.-T., Choi, K.-H., Lim, W., Cho, J. H., Tak, K. & Moon, I. 2011. LNG: An eco-friendly cryogenic fuel for sustainable development. *Applied Energy*, 88, 4264-4273.
- Liu, D.-x., Liang, L. & Li, M. Nonlinear finite element analysis of mechanical characteristics on CFRP composite pressure vessels. IOP Conference Series: Materials Science and Engineering, 2010. IOP Publishing, 012098.
- Liu, P. F., Chu, J. K., Hou, S. J., Xu, P. & Zheng, J. Y. 2012. Numerical simulation and optimal design for composite high-pressure hydrogen storage vessel: A review. *Renewable and Sustainable Energy Reviews*, 16, 1817-1827.
- Lloyd's Register 2015. Rules and Regulations for the Classification of Natural Gas Fuelled Ships.
- LR.com. 2016. *LR to class unique energy efficient ferry for Waddensee operations* [Online]. Available: <http://www.lr.org/en/news-and-insight/news/lr-to-class-unique-energy-efficient-ferry-for-waddensee-operations.aspx> [Accessed 13/6/2017].
- M.D.A. Marine Design Associates 2000. Dual Fuel (Natural Gas/Diesel) Marine Installations. *Workshop on Alternative Fuels for Ferries & Other Vessels*. Alameda, California.

- MAN 2014. *ME-GI Dual Fuel MAN B&W Engines: A Technical, Operational and Cost-effective Solution for Ships Fuelled by Gas*.
- Marine Log. 2014a. *CNG fueled Reverse Stern Drive tug under development* [Online]. Available: [http://www.marinelog.com/index.php?option=com\\_k2&view=item&id=6912:cng-fueled-reverse-stern-drive-tug-under-development&Itemid=225](http://www.marinelog.com/index.php?option=com_k2&view=item&id=6912:cng-fueled-reverse-stern-drive-tug-under-development&Itemid=225) [Accessed 11/6/2017].
- Marine Log. 2014b. *Rio Olympics ferries to have Caterpillar DGB gen sets* [Online]. Available: [http://www.marinelog.com/index.php?option=com\\_k2&view=item&id=7681:rio-olympics-ferries-to-have-caterpillar-dgb-gen-sets&Itemid=226](http://www.marinelog.com/index.php?option=com_k2&view=item&id=7681:rio-olympics-ferries-to-have-caterpillar-dgb-gen-sets&Itemid=226) [Accessed 11/6/2017].
- Mosaad, M. A. 2013. Compressed natural gas powered inland navigation ships. *Annals of the University Dunarea de Jos of Galati: Fascicle II, Mathematics, Physics, Theoretical Mechanics*, 36.
- NGV Global News. 2015. *First CNG-powered Ferry to Sail in 2016* [Online]. Available: <http://www.ngvglobal.com/blog/first-cng-powered-ferry-to-sail-in-2016-0212> [Accessed 13/6/2017].
- Papadakis, A. & Tsouvalis, N. 2015. "Results of material characterization experimental testing." Technical report No. 2.1 within the framework of National Research Project DEEP CO-HOUS.
- Papadakis, A. Z., Themelakis, J. G. & Tsouvalis, N. G. 2017. The effect of geometric and manufacturing parameters on filament wound composites split disk test results. *International Maritime Association of the Mediterranean Conference, (IMAM 2017)*. Lisbon, Portugal.
- Papagiannakis, R. G. & Hountalas, D. T. 2004. Combustion and exhaust emission characteristics of a dual fuel compression ignition engine operated with pilot Diesel fuel and natural gas. *Energy Conversion and Management*, 45, 2971-2987.
- Park, J.-S., Hong, C.-S., Kim, C.-G. & Kim, C.-U. 2002. Analysis of filament wound composite structures considering the change of winding angles through the thickness direction. *Composite Structures*, 55, 63-71.
- Peters, S. T., Green, J., Koussios, S., Priestley, A. P., Lowrey McLarty, J., Leslie, J. & Reynolds, H. 2011. *Composite Filament Winding*.
- Piellisch, R. 2012. *Ragasco Type IVs for New Mercedes* [Online]. Available: <http://www.fleetsandfuels.com/fuels/cng/2012/09/ragasco-type-ivs-for-new-mercedes/> [Accessed 18/8/2017].
- Pospiech, P. 2014. *Reliability ensures order for Alfa Laval's PureSOX* [Online]. Available: <http://articles.maritimepropulsion.com/article/Reliability-ensures-order-for-Alfa-Lavals-PureSOX-1365.aspx>.
- Sarafoglou, C. & Tsouvalis, N. 2015. Deliverable 5.2 for "Compressed Liquid Tank (5000 psi and 1000 psi) Manufactured by composite materials (carbon fibers and epoxy resins)" Project.
- Semolinos, P., Olsen, G. & Giacosa, A. LNG as Marine Fuel: Challenges To Be Overcome. 17th International Conference & Exhibition on Liquefied Natural Gas (LNG 17), 2013 Houston. sgmf 2014. *Gas as a Marine Fuel - An introductory Guide*.
- Shen, F. C. 1995. A filament-wound structure technology overview. *Materials Chemistry and Physics*, 42, 96-100.
- ship-technology.com. 2017. *Texelstroom Ferry, Netherlands* [Online]. Available: <http://www.ship-technology.com/projects/texelstroom-ferry/>.
- ShipSpotting.com. 2015a. *Accolade II* [Online]. Available: <http://www.shipspotting.com/gallery/photo.php?lid=2221461>.
- ShipSpotting.com. 2015b. *NP Rayong* [Online]. Available: <http://www.shipspotting.com/gallery/photo.php?lid=2385438>.
- Simulia 2014. *Abaqus 6.14 "Analysis User's Guide"*.
- Simulia 2016. *Wound Composite Modeler for Abaqus User's Manual*.

- Stuer-Lauridsen, F., Nielsen, J. B., Odgaard, T., Birkeland, M., Graugaard, C. W., Blikom, L., Muro-Suné, N., Andersen, M. & Øvlisen, F. 2010. *Natural gas for ship propulsion in Denmark-Possibilities for using LNG and CNG on ferry and cargo routes.*
- Vasiliev, V. V., Krikanov, A. A. & Razin, A. F. 2003. New generation of filament-wound composite pressure vessels for commercial applications. *Composite Structures*, 62, 449-459.
- Velosa, J. C., Nunes, J. P., Antunes, P. J., Silva, J. F. & Marques, A. T. 2009. Development of a new generation of filament wound composite pressure cylinders. *Composites Science and Technology*, 69, 1348-1353.
- Wang, R., Jiao, W., Liu, W., Yang, F. & He, X. 2011. Slippage coefficient measurement for non-geodesic filament-winding process. *Composites Part A: Applied Science and Manufacturing*, 42, 303-309.
- Wei, L. & Geng, P. 2016. A review on natural gas/diesel dual fuel combustion, emissions and performance. *Fuel Processing Technology*, 142, 264-278.
- Wikipedia. 2005a. *Filament winding* [Online]. Available: [https://en.wikipedia.org/w/index.php?title=Filament\\_winding&action=history](https://en.wikipedia.org/w/index.php?title=Filament_winding&action=history) [Accessed 19/8/2017].
- Wikipedia. 2005b. *Liquefied natural gas* [Online]. Available: [https://en.wikipedia.org/wiki/Liquefied\\_natural\\_gas](https://en.wikipedia.org/wiki/Liquefied_natural_gas).
- Wikipedia. 2006. *Natural Gas* [Online]. Available: [https://en.wikipedia.org/wiki/Natural\\_gas](https://en.wikipedia.org/wiki/Natural_gas).
- Willardson, R. P., Gray, D. L. & DeLay, T. K. Improvements in FEA of Composite Overwrapped Pressure Vessels. Society for the Advancement of Material and Process Engineering–Fall Technical Conference,(October 2009), 2009.  
[www.cngschool.com](http://www.cngschool.com).
- [www.fibre-reinforced-plastic.com](http://www.fibre-reinforced-plastic.com). 2009. *Composite Fabrication : Filament Winding* [Online]. Available: <http://www.fibre-reinforced-plastic.com/2009/> [Accessed 19/8/2017].
- Xu, P., Zheng, J. Y. & Liu, P. F. 2009. Finite element analysis of burst pressure of composite hydrogen storage vessels. *Materials & Design*, 30, 2295-2301.
- Yang, X.-D. & Hu, K.-X. 2010. Technical practices of compressed natural gas fueled ship *Journal of Ship Production*, 26, 211-218.
- Zu, L. 2012. *Design and Optimization of Filament Wound Composite Pressure Vessels*. Doctoral Thesis, TUDelft.
- Zu, L., Koussios, S. & Beukers, A. 2010. Design of filament-wound domes based on continuum theory and non-geodesic roving trajectories. *Composites Part A: Applied Science and Manufacturing*, 41, 1312-1320.
- Zu, L., Wang, J. & Li, S. 2016. Influence of fiber slippage coefficient distributions on the geometry and performance of composite pressure vessels. *Polymer Composites*, 37, 315-321.

## Appendix A

Code for the calculation of the winding angle along the dome according to equations (3-1) (Lei Zu) and (3-9) (Abaqus)

```

clc
clear all
close all
global R c r0 zmax lamda
R=0.25; %radius of cylinder
cR=1; %minor to major axis ratio
c=cR*R; %minor axis of ellipsoid
r0=0.0125; %radius of polar opening
lamda=0.2; %maximum static friction coefficient
tmdiam=100000; %tmdiamata diamerisis dome
zmax=c*sqrt(1-(r0^2)/(R^2));
z=0:zmax/tmdiam:zmax;
for ii=1:length(z)
    r(ii)=R*sqrt(1-(z(ii)^2)/(c^2));
end

%Runge-Kutta

h=zmax/tmdiam; % step size
a = zeros(1,length(z));
a(1) = 89*pi/180; % initial condition
for i=1:(length(z)-1)% calculation loop
    k_1 = h*fza(z(i),a(i));
    k_2 = h*fza(z(i)+0.5*h,a(i)+0.5*k_1);
    k_3 = h*fza((z(i)+0.5*h),(a(i)+0.5*k_2));
    k_4 = h*fza((z(i)+h),(a(i)+k_3));
    a(i+1) = a(i) + (1/6)*(k_1+2*k_2+2*k_3+k_4);%calculates winding angle
according to Lei Zu equation
end
ab=abacus(a(tmdiam+1));%calculates winding angle according to abacus
equation
plot(z/c,ab*180/pi,':r')
hold on
z=fliplr(z);
plot(z/c,a*180/pi,'-r')
hold on
title('R=0.25m, spherical')
xlabel('dome longitudinal axis (z/c)') % x-axis label
ylabel('winding angle (degrees)') % y-axis label
legend ('Abaqus','Lei Zu')

function aabaq=abacus(a0)
    global R c r0 zmax
    a0r=asin(r0/R);

```



```

r0a=R*sin(a0);
d=a0-a0r;
tmdiam=100000;
zmax=c*sqrt(1-(r0^2)/(R^2));
n=1;
z=0:zmax/tmdiam:zmax;
for ii=1:length(z)
    r(ii)=R*sqrt(1-(z(ii)^2)/(c^2));
    a(ii)=asin(r0/r(ii))+d*((r(ii)-r0)/(R-r0))^n;
end
aabaq=a;

function f=fza(z,a)
global R c zmax lamda r0
r=R*sqrt(1-((z-zmax)^2)/(c^2));
rt=-(R/(c^2))*((z-zmax)/sqrt(1-((z-zmax)^2)/(c^2)));
r2t=-R/((c^2)*((1-((z-zmax)^2)/(c^2)))^(1.5)));
l=lamda*cos((pi/2)*((r-r0)/(R-r0))); %lamda distribution along the dome
f=l*((sin(a)*tan(a)/r)-(r2t*cos(a)/(1+rt^2)))-(rt*tan(a)/r);

```